https://ntrs.nasa.gov/search.jsp?R=19860021045 2020-03-20T13:27:56+00:00Z

NASA Technical Memorandum 87792

NASA-TM-87792 19860021045

A Superconducting Tunnel Junction Receiver for Millimeter-Wave Astronomy

FOR REFERENCE

NOT TO BE TAKEN FROM THIS ROOM

Shing-Kuo Pan and Anthony R. Kerr

JULY 1986

LIBRARY COPY

JUL 1986

LANGLEY RESEARCH CENTER
LIBRARY, NASA
HAMPTON, VIRGINIA

NASA

NF01649

NASA Technical Memorandum 87792

A Superconducting Tunnel Junction Receiver for Millimeter-Wave Astronomy

Shing-Kuo Pan
NASA Goddard Institute for Space Studies
New York, New York
and
Columbia University
New York, New York

Anthony R. Kerr
NASA Goddard Institute for Space Studies
New York, New York

NASA
National Aeronautics
and Space Administration

Scientific and Technical
Information Branch

1986

TABLE OF CONTENTS page

CHAPTER 1. INTRODUCTION 1

CHAPTER 2. THEORY 12

2.1 Introduction 12

2.1.1 Basic Mixer Terminology 14

2.2 Classical Mixer Theory - Generalized Heterodyne Receiver Model 18

2.2.1 Introduction 18

2.2.2 Frequency Notation 19

2.2.3 Conversion Admittance Matrix 20

2.2.4 Mixer Conversion Loss 24

2.2.5 Mixer Port Impedances 25

2.3 Theory of Superconductive Tunneling 27

2.3.1 Introduction 27

2.3.2 Dynamic Tunneling Model 27

2.4 Quantum Mixer Theory 38

2.4.1 Introduction 38

2.4.2 Quantum Expressions for the Conversion Admittance Matrix 38

2.5 SIS Mixer Noise Theory 44

2.5.1 Introduction 44

2.5.2 Shot Noise 44

2.5.3 Thermal Noise 49

2.5.4 Total SIS Mixer Noise 50

2.6 The 3-Frequency Approximation 52

2.6.1 Equal Signal and Image Termination 58

2.6.2 Short-circuited Image Case 63

2.7 Theory of Arrays 68

2.8 Computer Modeling 70

2.8.1 Outline of the Computing Method 71

CHAPTER 3. JUNCTION DESIGN AND FABRICATION 77

3.1 Introduction 77

3.2 Optimum Junction Parameters for Mixer Applications 77

3.2.1 Optimum $\omega R_N C_J$ Product 78

3.2.2 Normal State Resistance 79

3.2.3 Junction Capacitance 80

3.2.4 Junction Area 81

3.2.5 Critical Current Density 82

3.2.6 Series Array 84

3.3 Junction Fabrication 85

3.3.1 Princeton - NBS Junction 85

3.4 Junction Storage 87

CHAPTER 4. MIXER BLOCK DESIGN AND CHARACTERIZATION 88

4.1 Introduction 88

4.2 Mixer Block Design and Construction 89

4.2.1 Type J-J Mixer 89

4.2.2 Type-D Mount 91

4.3 Mixer Mount Characterization - Scale Model Measurements 94

4.3.1 Introduction 94

4.3.2 The 40X Scale Model 94

4.3.3 Measurement Set-up 96

4.3.4 Correction to the Measured Embedding Admittance 96

4.3.5 Available Embedding Admittance: Measured Results 99

4.4 Theoretical Characterization of the Mixer Mount 101

4.4.1 Introduction 101

4.4.2 Microwave Equivalent Circuit 101

4.4.3 Loss in the Mixer Mount 103

4.4.4 Embedding Admittance Calculated from Equivalent Circuit 105

CHAPTER 5. EXPERIMENTAL SET-UP FOR SIS MIXER MEASUREMENT 107

5.1 Introduction 107

5.2 The RF Section 107

5.3 Cryogenic System - the Test Dewar 109

5.4 dc Bias and Measuring System 111

5.5 IF Measuring System 113

5.6 Computer Instrumentation 117

CHAPTER 6. THE MIXING EXPERIMENTS AND RESULTS 118

6.1 Introduction 118

6.2 Experimental Procedure 118

6.3 Experimental Results 123

6.3.1 The Type J-J Mixer 123

6.3.2 The Type-D Mixer 125

6.4 Comparison: Experimental Results Versus Theoretical Predictions 128

6.4.1 Quantitative Verification of Tucker's Theory 128

6.4.2 Analysis of A Type-D Mixer 131

CHAPTER 7. A PRACTICAL SIS RECEIVER AT 115 GHz 135

7.1 Introduction 135

7.2 Receiver Description 136

7.3 Receiver Performance 140

CHAPTER 8. OBSERVATIONS OF DISTANT MOLECULAR CLOUDS TOWARD THE CYGNUS-X REGION WITH A 4-FOOT MILLIMETER WAVE TELESCOPE 144

8.1 Introduction 144

8.2 The Columbia-GISS Sky Survey Telescope 145

8.3 Observations 147

8.4 Discussion 149

CHAPTER 9. FUTURE WORK, SUMMARY AND CONCLUSION 154

9.1 Directions for Future Work on SIS Receivers 154

9.2 Ultimate Limits to SIS Receivers 157

9.3 Summary and Conclusions 159

APPENDIX I THE EXPERIMENTAL DETERMINATION OF THE EQUIVALENT INDUCTANCES L_I, L_{II}, AND L' 161

APPENDIX II DETERMINATION OF THE EQUIVALENT CIRCUIT ELEMENTS OF THE TYPE-D MOUNT 163

FIGURE CAPTIONS 166

FIGURES 178

REFERENCES 226

ACKNOWLEDGEMENTS

I wish to express my sincere appreciation to Dr. Anthony Kerr, my thesis advisor, for his support, guidance, and encouragement throughout this project. I also want to thank Professor Patrick Thaddeus, my advisor at Columbia University, for his constant support and direction. I want to express special gratitude to Dr. Marc Feldman, whom I consider as my advisor, for his invaluable suggestions, and for performing all the theoretical calculations presented in chapter 6. Special thanks must go to Professor John Tucker for teaching me his quantum mixer theory at the beginning of this work.

I want, too, to thank the many people who made important contributions to the construction of the SIS receiver: Peter Timbie, who fabricated the SIS junction; John Grange, who developed the mixer assembly technique; Samuel Palmer, who designed the overall receiver; Dennis Mumma and Moy Wong, who built most of the electronics; and Harry Miller and Michael Eilenfeldt, who made the mixer block and, essentially, all the non-commerical components of the receiver.

I am particularly grateful to Yi-Long Huang for assistance in the observations and in writing chapter 8,

to David Leisawitz for reviewing and commenting on chapter 8, and to Ronald Maddalena for assistance in installing the receiver on the telescope.

I am indebted to Drs. Richard Cohen, Thomas Dame, Carl Gottlieb, Ross Hicks, Dorn Peterson, Peter Siegel, and Yuan Taur for many helpful discussions and suggestions at various stages of this project.

I would like to express my deepest appreciation to my fiancée, Tswen-Jye Chou, who typed this thesis and aided in many ways in the preparation of the manuscript; her love, patience, and encouragement helped me to complete this project.

Finally, I want to dedicate this thesis to my parents with gratitude for their emotional support and encouragement throughout these years.

CHAPTER 1. INTRODUCTION

During the last decade, the development of millimeter wave astronomy has dramatically improved our understanding of the nature of the interstellar medium. This has resulted primarily from observations of the spectral line radiation from rotational transitions of interstellar molecules. More than 50 molecular species have been identified in a few very bright sources whose physical conditions enable excition of the molecules [68]. Giant molecular clouds have been discovered in the Galaxy. Molecular clouds have been found to constitute an appreciable fraction of the interstellar medium by mass and to be the raw material from which stars evolve. Studies of these molecular clouds and their distribution in space have led to an improved understanding of star formation processes [16], stellar mass loss [83] and galactic structure [9]. The relation between molecular clouds and supernova remnants [26], and between molecular clouds and young star clusters [36] are two among many current topics of investigation.

Although a great deal of work has been done, many worthy experiments, such as large scale mapping of extragalactic sources, and searches for new interstellar molecules, become feasible only with instruments of

significantly greater sensitivity than those which presently exist. It is the main purpose of this research project to develop a new kind of receiver, using a superconductor - insulator - superconductor quasiparticle tunnel junction as the mixing element, to overcome the limitations inherent in all previously existing millimeter-wave receivers.

As the radiation from interstellar molecules is extremely weak, sensitive spectral line receivers are needed to detect these very faint signals. Heterodyne receivers are commonly used in radio-telescopes to achieve high spectral resolution, which is necessary in order to determine the velocity of the molecular clouds. The heterodyne receiver consists of a "mixer" followed by an IF amplifier. The receiver noise temperature is:

$$T_R = T_M + LT_{IF} \tag{1.1}$$

where L is the mixer conversion loss, T_M is the mixer noise temperature and T_{IF} is the equivalent noise temperature of the IF amplifier. The two terms on the right side of eq. (1.1) are usually of comparable magnitude, so it is clear that to achieve a major improvement in T_R, both mixer parameters, L and T_M must be improved.

For a heterodyne mixer receiver operating in the Rayleigh-Jeans' limit, i.e. $h\nu < kT$, the sensitivity is given by the radiometric equation [69]:

$$\delta T = \frac{KT_R}{(\tau \, \Delta f)^{1/2}} \tag{1.2}$$

where δT is the smallest detectable signal, τ is the observation time required to detect δT, K is a constant and Δf is the pre-detection bandwidth. From this equation it follows that the observating time required to detect a small signal is proportional to the square of the receiver's noise temperature. In order to exploit fully the potential of the telescope, it is necessary to improve the receiver performance to the point where the overall system noise temperature is comparable to or smaller than the sky noise (typically 135 K at 115.3 GHz).

In the past decade, several different kinds of mixers have been developed, and GaAs Schottky barrier diode mixers have been the most commonly used for millimeter wavelength radio astromony. A cooled Schottky diode receiver, with about 125 K receiver noise temperature, operating at 90 - 120 GHz, has been reported [47].

However, since this technology is very well developed, there is little prospect for any further dramatic improvement in the performance of semiconductor diode mixers. Liquid helium cooled InSb hot electron bolometer mixers [45] have also been successfully operated, but their performance is severely limited by their very narrow instantaneous bandwidth ($\sim$ 1 MHz).

Several different kinds of superconductive tunneling devices have also been extensively studied for use in heterodyne receivers, among them are the point-contact Josephson junction, superconducting micro-bridge, super-Schottky diode and SIN junction. Point-contact and micro-bridge Josephson junction mixers belong to the same category, in which the extremely nonlinear Josephson tunneling currents are used to achieve mixing. Although these devices can achieve conversion gain, their intrinsic high noise properties [67] have eliminated them from the competition. Furthermore, due to their lack of mechanical stablity, experimental results with point-contact junctions are usually very hard to reproduce and the junction's thermal recyclability is also very poor.

Unlike the Josephson effect mixer mentioned above, the super-Schottky (superconductor-semiconductor) diode mixer and the superconductor - insulator - normal metal (SIN) junction mixer, use the nonlinear quasiparticle

current-voltage characteristic to achieve mixing. The super Schottky diode mixer is limited by its series spreading resistance and junction capacitance, to relatively low (i.e. microwave) frequencies [60]. The performance of an SIN array mixer at 73.5 GHz has been reported [53] and the result is very encouraging. However, the I-V characteristic of the SIN junction is not as strongly nonlinear as that of the SIS device, and the resistance of the normal electrode may also tend to degrade the performance. SIN mixers are not, therefore, the best choice for the 100 GHz range. Since SIN mixers are intrinsically free from Josephson effect noise, they are very promising for use at higher frequencies (perhaps 300 - 1000 GHz).

Recently, the superconductor - insulator - superconductor (SIS) quasiparticle tunnel junction has been demonstrated by Richards and Shen [49], Dolan, Phillips and Woody [14], and Rudner and Claeson [51] to be useable as a low noise millimeter wave mixer. It is known that there are two current carrying mechanisms in an SIS tunnel junction: the Josephson (pair) tunneling current and the quasiparticle (single electron) tunneling current. In an SIS mixer, heterodyne mixing is performed using the extremely nonlinear quasiparticle branch of the I-V characteristic which has a sudden onset of conduction at

the full superconducting gap voltage $2\Delta/e$ arising from the effective energy gap in the density states of the superconductors. From an ideal B-C-S calculation it is shown that this I-V characteristic approaches that of an ideal resistive diode near the gap voltage [22,80]. Therefore, according to classical mixer theory, an ideal SIS quasiparticle mixer should have very good mixing performance (e.g. for an image rejecting mixer, $L \rightarrow 0$ dB). However, both theoretical and experimental studies of the high frequency performance of this device have indicated that, when the photon energy, $\hbar\omega/e$, at the input frequency becomes comparable to the voltage scale of the I-V curve nonlinearity, the classical theory is no longer able to describe the performance. Nonclassical phenomena such as conversion gain in a resistive mixer, and quantum-limited sensitivity, have been predicted by the "quantum mixer theory", recently developed by Tucker [73] and later verified by experiments. Recently, two other nonclassical phenomena, negative output impedance and infinite available gain, both predicted by Tucker's theory, have been observed in this device. Several complete SIS receivers, operating from 45 GHz to 250 GHz with performance comparable to Schottky diode receivers, have been reported by different groups [3,4,40,41,46,64,65]. With their potentially low noise properties and very low pump (LO) power requirement, it is likely that the SIS

receiver will be the prime choice in the future for radio astronomy in the millimeter wave frequency range.

This research is directed towards studying the performance of the SIS quasiparticle tunnel junction receiver in the 110-118 GHz region of the radio spectrum, with the ultimate objective of constructing an ultra-sensitive SIS receiver for 115.3 GHz CO line observations. Although Tucker's quantum mixer theory has provided the theoretical framework for analysis and design of the SIS mixer, this theory is rather complicated in its derivation and is very hard to interpret compared with the familiar classical theory. Furthermore, only under certain approximations (e.g. the 3-frequency approximation) is it possible to obtain a tractable set of equations which can be used to characterize mixer performance. Even these simplified equations contain infinite series of Bessel function products and a highly nonlinear junction response function. Hence, most theoretical calculations have hitherto been done by extensive computer simulation, and have been difficult to interpret. Apart from these difficulities, the practical situation is even more complicated. In this work, we have therefore taken a primarily experimental approach. In the following chapters we shall thoroughly discuss the design, fabrication, and optimization of our SIS quasiparticle

mixers. The performance of these mixers is in excellent agreement with the theoretical predictions using Tucker's theory assuming the 3-frequency approximation. This work has led to the construction of an SIS receiver which is now successfully operating on the Columbia-GISS CO Sky Survey telescope on the roof of the Pupin laboratory. It is the most sensitive receiver ever built in this frequency range, with a single sideband receiver noise temperature of 83 K at 115.3 GHz. Observations of the ^{12}CO emission from molecular clouds beyond the solar circle at $\ell = 80^{o}$, made using this SIS receiver, will be described.

The success of this receiver has not only dramatically improved the observation efficiency of the Columbia-GISS telescope, but has also demonstrated that the SIS mixer has the potential to become the preferred front-end in future millimeter wave radio astronomy receivers.

The following outline describes the contents of each chapter of this thesis, and indicates the original contributions:

Chapter 2 contains a detailed description of Tucker's quantum mixer theory (including mixer noise theory), which is the fundation of this research project. We then apply this theory to the SIS mixer in two special cases: 1)

equal signal and image terminations (i.e. the DSB case), and 2) the image frequency short-circuited (SSB case). The conditions under which it is possible to achieve negative output impedance and infinite available gain are investigated. A computer program was developed to predict and analyze the performance of an SIS mixer.

Chapter 3 describes the design and fabrication of the junctions used in this work. The choice of the various fabrication parameters of SIS junctions for optimum mixer performace is discussed.

In chapter 4, we describe the design of the mixers used in this work. Measurement techniques used to characterize the mixer mount are discussed. A microwave equivalent circuit of the mixer mount, including the effects of conductor loss, is derived, and used to study the available embedding impedances at the signal and image frequencies. This information is necessary for an accurate analysis of the performance of the SIS mixer, and for optimization of the stripline circuit in the next design iteration.

Chapter 5 describes the experimental apparatus used for measuring the performance of the SIS mixer, and discusses the calibration of the measuring system.

In chapter 6 we describe the mixing experiments in

which Tucker's 3-frequency quantum mixer theory is quantitatively verified for the first time. In these experiments, the first observation of negative dc differential resistance and infinite available gain in an SIS mixer were made. These are quantum effects which are not possible in classical mixers. The best mixer performance we have achieved at 115.3 GHz are an SSB conversion loss of 6.9 dB and an SSB mixer noise temperature of 20 K, with a lower-sideband rejection > 25 dB.

The optimized SIS mixer described in chapter 6 is used to construct an ultra low-noise 110-118 GHz SIS receiver. Chapter 7 describes the construction and performance of this receiver, which is the most sensitive ever reported for this frequency range.

In collaborating with Y.-L. Huang, we undertook some astronomical observations to demonstrate the power of this new receiver on the Columbia-GISS 4-ft telescope. The typical integration time per scan is only about 1 minute for an rms noise of 0.25 K with a bandwidth of 250 KHz per filterbank channel, demonstrating that the system is in fact 25 times faster than with the previous Schottky diode receiver. Observatioins of the distant molecular clouds towards the Cygnus-X region are presented in chapter 8.

In chapter 9 we discuss future planned work on SIS receivers and their ultimate limits. A summary of the present work is given. This concludes the thesis.

CHAPTER 2. THEORY

2.1 Introduction

Ever since its discovery, the superconducting (Josephson) tunnel junction has appeared likely to be useful as a very low noise amplifier, mixer or direct detector in the millimeter wavelength range. Its strong nonlinearity at low currents leads to extremely low shot noise, and it requires a very small amount of local oscillator power (at most a microwatt) to operate as a mixer. Also, the cryogenic operating environment suggests that a superconducting detector or mixer will have low thermal noise. In addition to the potential of these devices in fields such as millimeter wave astronomy, atmospheric physics and space communication, the development of the theory of the superconducting tunnel junction mixer and detector has its own academic interest, since this involves the study of the interaction process between the tunneling electrons and the input signal field (photon).

The basic principle of frequency conversion using nonlinear resistive elements has been extensively developed and interpreted by many authors [24,54,70,77]

employing a classical approach which assumes an instantaneous device response to the incident electromagnetic field. In classical theory, the small signal performance of a periodically pumped nonlinear device is usually described by a square admittance matrix. The elements of this matrix are simply related to the Fourier coefficients of the conductance and capacitance waveforms produced in the nonlinear device by the local oscillator. The small-signal current and voltage components at different sidebands will therefore be linearly related by this conversion matrix, and the device performance can be calculated in a straightforward way.

When the input photon energy in volts, $\hbar\omega/e$, is sufficiently large compared with the voltage scale of the device's dc I-V nonlinearity, the classical theory is not applicable and the recently developed quantum mixer theory [73] must be used to calculate the performance of a mixer. This theory, which includes the quantized nature of the charge carriers in the nonlinear single-particle tunneling device, was originally constructed by Tucker [71,72,73,74,75] and was elaborated later by Feldman [17], Shen [57] and, Smith and Richards [62]. Tucker used photon-assisted tunneling theory to evaluate the elements of the mixer conversion matrix. Once this step has been done, the mixer analysis proceeds exactly as with the

classical theory. Noise properties of the tunnel junction mixer are also described by the quantum mixer theory. When this theory is applied to the SIS quasiparticle mixer with the input photon energy comparable to the voltage scale of junction's dc I-V nonlinearity, the predicted results differ strikingly from the classical analysis. For instance: reactive mixing terms appear in the mixer admittance matrix, and it becomes possible to achieve gain, even infinite available gain, under certain circumstances. Negative output impedance and quantum limited sensitivity are also possible. All of these (except possibly quantum limited sensitivity) have now been verified by experiments. Since this theory provides the theoretical framework for the design and analysis of our SIS quasiparticle mixer, it is outlined in some detail in this chapter.

2.1.1 Basic Mixer Terminology

In this section, we introduce some basic mixer terminology. The mixer contains one (or more) nonlinear elements such as a semiconductor Schottky barrier diode or a superconducting tunnel junction. The (weak) signal, at frequency ω_s, and a (strong) local oscillator wave, at frequency ω_p, are coupled into these nonlinear devices,

where they generate, among other frequencies, an intermediate frequency (ω_{IF}) which is equal to the difference between signal and local oscillator frequencies. Other unwanted higher harmonics and sidebands are generally filtered out by the circuit. The performance of the simplest type of mixer is characterized by two quantities: the equivalent input noise temperature (T_M) and the mixer conversion loss (L_s) which is defined as:

$$L_s = \frac{\text{available power at the signal frequency}}{\text{power delivered to IF load}} \quad (2.1)$$

Usually, a mixer will produce an IF output at ω_{IF} from either of two input frequencies : the signal, at $\omega_s = \omega_p \pm \omega_{IF}$, or the image, at $\omega_p \mp \omega_{IF}$ (The choice of $\omega_p + \omega_{IF}$ or $\omega_p - \omega_{IF}$ as the "signal" usually depends on the particular experimental circumstances). Clearly there are two separate conversion losses, L_s and L_i, at the signal and image frequencies. Under certain special conditions, equal powers may be applied to the mixer at both the signal and image frequencies, in which case it is useful to define a double-sideband conversion loss, L_C, which is related to the two single-sideband quantities by [56]:

$$\frac{1}{L_C} = \frac{1}{L_s} + \frac{1}{L_i} \tag{2.2}$$

The quantity L_C is appropriate, for example, when the input signal to the receiver is from a blackbody radiator, as is used for calibrating the receiver's noise temperature.

A mixer for which $L_s << L_i$ (image rejecting) is called a single sideband (SSB) mixer, and its noise temperature, as measured using a blackbody radiator, will be denoted as $T_{M,SSB}$. If $L_s \approx L_i$, the mixer is called a double sideband (DSB) mixer, and the noise temperature measured using a blackbody radiator is designated as $T_{M,DSB}$. For some applications, a single sideband noise temperature is quoted for a DSB mixer. It is then given by [32,56]:

$$T_{M,SSB} = T_{M,DSB}\,(1 + L_s/L_i) \tag{2.3}$$

Thus $T_{M,SSB}$ is twice $T_{M,DSB}$ for a mixer which responds equally to both signal and image. It is known from the

classical theory of mixers [31,54] that the conversion loss of an ideal resistive mixer can be as low as 0 dB when there is complete image rejection, and 3 dB for a DSB mixer. Such an ideal mixer would generate no noise of its own, giving $T_M = 0$ K.

For spectroscopic observations, the spectral line appears only in one sideband, and it is more appropriate to use the single sideband values of noise temperatures and conversion loss. Thus in this thesis, except where explicitly noted, all numbers quoted are single sideband quantities.

2.2 Classical Mixer Theory - Generalized Heterodyne Receiver Model

2.2.1 Introduction

The fundamental concepts of classical mixer theory have been studied in depth by Torrey and Whitmer [70], Uhlir [77], Saleh [54], and Held and Kerr [24]. Since this theory is well developed and is the essential framework for the quantum mixer theory, we shall summarize it in this section.

In classical theory, the nonlinear mixer diode is represented by an equivalent circuit shown in Fig. 2-1. A conversion admittance matrix can be formed to relate the small signal-sideband currents and voltages at the diode. The elements of this matrix are simply related to the Fourier components of the conductance and capacitance waveforms produced in the nonlinear diode by the local oscillator drive. The conversion loss and input and output impedances can then be determined from this admittance matrix provided that the embedding impedance of the mixer mount is known at various sideband frequencies. However, in performing the theoretical calculation of the mixer performance, it is necessary to know the correct waveform of the local oscillator voltage $V_{LO}(t)$ at the

diode and the resultant diode current. This problem can be accomplished by an appropriate large signal analysis [23,58]. For the moment we shall just assume that $V_{LO}(t)$ is known and outline the small-signal mixer theory.

2.2.2 Frequency Notation

Saleh's frequency notation [54] will be used here. If a mixer is pumped at a frequency ω_p and has an intermediate frequency ω_0, the frequencies resulting from a distortion-free mixer are those sideband frequencies which can be put in the following form:

$$\omega_n = n\omega_p + \omega_0 \quad , \; n = -\infty,\ldots,-1,0,1,\ldots,\infty \qquad (2.4)$$

Thus ω_1, ω_{-1}, and ω_2 represent the upper sideband, lower sideband, and sum frequencies respectively. Note that $\omega_n<0$ for $n = -\infty,\ldots,-2,-1$. The sideband frequency index n is also used as a subscript with various electrical quantities. For instance, V_1, V_0, and V_{-1} represent the voltages at frequencies ω_1, ω_0 and ω_{-1}; I_1, I_0 and I_{-1} represent the currents at corresponding sidebands.

2.2.3 Conversion Admittance Matrix

Assuming that a dc voltage V_0, a local oscillator voltage $V_{LO}(t)$ and a small signal $v_{sig}(t)$ are impressed across the nonlinear device, then the total voltage waveform is:

$$V(t) = V_0 + V_{LO}(t) + v_{sig}(t) \tag{2.5}$$

Under the small signal approximation, the resultant current in the diode is given by:

$$\langle I(t) \rangle = I_{LO}(t) + i_{sig}(t) \tag{2.6}$$

The small signal voltage and current can be expressed in terms of the individual sideband frequency component:

$$v_{sig}(t) = \mathrm{Re} \sum_{m=-\infty}^{\infty} v_m e^{i\omega_m t} \tag{2.7}$$

$$i_{sig}(t) = \mathrm{Re} \sum_{m=-\infty}^{\infty} i_m e^{i\omega_m t} \tag{2.8}$$

Torrey and Whitmer [70] have shown that for small signals these current and voltage components are linearly related by a matrix equation:

$$i_m = \sum_{m'} Y_{mm'} v_{m'} \tag{2.9}$$

the square matrix Y is called the conversion admittance matrix. For an ideal diode, the elements of this matrix are given by Torrey and Whitmer and are:

$$Y_{mm'} = G_{m-m'} + j\omega_m C_{m-m'} \tag{2.10}$$

where G_k and C_k are the Fourier coefficients of the diode conductance G(t) and capacitance C(t):

$$G(t) = \sum_{k=-\infty}^{\infty} G_k \exp(jk\omega_p t) \quad , \quad G_k = G_{-k}^{*} \tag{2.11}$$

$$C(t) = \sum_{k=-\infty}^{\infty} C_k \exp(jk\omega_p t) \quad , \quad C_k = C_{-k}^{*} \tag{2.12}$$

As shown in Fig. 2-1, the matrix Y is the admittance matrix of the intrinsic diode and can be regarded as a multifrequency multiport network, each port of which represents one sideband frequency. Let I_m and Y_m be the source current and admittance termination at each port. Then an augmented network outlined by the broken line in Fig. 2-1 can be formed to represent the whole mixer which is characterized by the augmented admittance matrix Y' defined by:

$$Y'_{mm'} = Y_{mm'} + Y_m \delta_{mm'} \tag{2.13}$$

and we have

$$\begin{aligned} I_m &= i_m + Y_m v_m \\ &= \sum_{m'} Y'_{mm'} v_{m'} \end{aligned} \tag{2.14}$$

inverting this matrix equation, we have

$$v_m = \sum_{m'} Z'_{mm'} I_{m'} \tag{2.15}$$

where

$$||Z'_{mm'}|| = ||Y'_{mm'}||^{-1}$$

$$= ||Y_{mm'} + Y_m \delta_{mm'}||^{-1} \qquad (2.16)$$

In particular, the IF output voltage can be written as:

$$v_O = \sum_{m'} Z'_{Om'} I_{m'}$$

$$= Z'_{OO} \sum_{m'} \lambda_{Om'} I_{m'} \qquad (2.17)$$

where

$$\lambda_{Om} = Z'_{Om} \; / \; Z'_{OO} \qquad (2.18)$$

and

$$I_{eff} = \sum_{m'} \lambda_{Om'} I_{m'} \qquad (2.19)$$

can be regarded as an equivalent source current at the IF frequency connected in parallel with the load Y_L and the output admittance of the mixer $(1/Z'_{00})$.

2.2.4 Mixer Conversion Loss

The mixer conversion loss, from sideband ω_j to the IF ω_0, is defined as the ratio of the power available from the source Y_j at the input port j to the power delivered to the load Y_L at port 0. The available signal power at the port j is:

$$P_{in} = \frac{|I_{sj}|^2}{8G_j} \tag{2.20}$$

Where I_{sj} is the source current at the input port j. The power delivered to the IF load Y_L is:

$$P_{out} = \frac{1}{2} G_L |v_0|^2 \tag{2.21}$$

$$= \frac{1}{2} G_L |Z'_{0j}|^2 |I_{sj}|^2$$

where G_j and G_L are the real parts of Y_j and Y_L respectively. The mixer conversion loss is then given by:

$$L_C = \frac{P_{in}}{P_{out}}$$

$$= \frac{1}{4G_j G_L |Z'_{0j}|^2} \qquad (2.22)$$

2.2.5 Mixer Port Impedances

The impedance Z_m, which is defined as mixer's m-th port impedance (see Fig. 2-1), can be found by open circuiting the corresponding port termination ($Y_m = 0$) and measuring the impedance at port m of the augmented network. Therefore the port impedance is given by the mm-th element of the Z' matrix defined in (2.16) with $Y_m = 0$. That is:

$$Z_m = Z'_{mm,Y_m=0}$$

$$= ||Y'_{mm'}||^{-1}_{mm,0} \qquad (2.23)$$

Where the subscript "0" indicates that the mm-th element of this matrix is evaluated with $Y_m = 0$. For instance, the upper sideband input impedance of the mixer is:

$$Z_{1,in} = \begin{bmatrix} & \vdots & \vdots & \vdots & \\ \cdots & Y_{11} & Y_{10} & Y_{1-1} & \cdots \\ \cdots & Y_{01} & Y_{00}+Y_L & Y_{0-1} & \cdots \\ \cdots & Y_{-11} & Y_{-10} & Y_{-1-1}+Y_{-1} & \cdots \\ & \vdots & \vdots & \vdots & \end{bmatrix}^{-1} \qquad (2.24)$$

and the IF output impedance is:

$$Z_{IF,out} = \begin{bmatrix} & \vdots & \vdots & \vdots & \\ \cdots & Y_{11}+Y_1 & Y_{10} & Y_{1-1} & \cdots \\ \cdots & Y_{01} & Y_{00} & Y_{0-1} & \cdots \\ \cdots & Y_{-11} & Y_{-10} & Y_{-1-1}+Y_{-1} & \cdots \\ & \vdots & \vdots & \vdots & \end{bmatrix}^{-1} \qquad (2.25)$$

2.3 Theory of Superconductive Tunneling

2.3.1 Introduction

A superconductor - insulator - superconductor (SIS) tunnel junction consists of two bulk superconducting electrodes separated by a thin insulator layer approximately 20 ~ 40 Å thick. Much has been learned about the nature of tunneling in the 20 years since Giaever's experiments on non-Josephson tunneling [20,21] and Josephson's theoretical treatment of superconducting tunnel structures that display phase coherence [29]. The goal of this section is to determine the tunnel junction quasiparticle current response in the presence of the applied field. Since we are only interested in non-Josephson tunneling, the Josephson effect (the supercurrent tunneling) will be neglected in this treatment*.

2.3.2 Dynamic Tunneling Model

* In experiments, this situation can be realized by applying a magnetic field to suppress the observable pair tunneling current, or by biasing the junction close to the gap voltage.

Following the treatment in Tucker [73] and Rogovin and Scalapino [50], the total system Hamiltonian for the tunnel junction in the presence of external fields is given by:

$$H = H_R^0 + H_L^0 + eV(t)N_L + H_T \tag{2.26}$$

Where H_R^0 and H_L^0 are the full many-body Hamiltonians for the right- and left-hand electrodes. Coupling between the external field and the tunnel junction is characterized by the time-dependent potential eV(t) multiplied by the left-side number operator N_L, with $N_L = \sum_k C_k^+ C_k$.

H_T is the transfer Hamiltonian which describes the coupling between the two electrodes and is to be considered as a perturbation. Following Cohen, Falicov, and Phillips [7], H_T can be written as:

$$\begin{aligned} H_T &= \sum_{kq\sigma} T_{kq} C_k^+ C_q + \sum_{kq\sigma} T_{kq}^* C_q^+ C_k \\ &= H_T^+ + H_T^- \end{aligned} \tag{2.27}$$

Where C_k and C_q are one-electron operators representing Bloch states on the left- and right-hand sides of the barrier. H_T^+ corresponds to the first term, in which an electron is transfered from a state q on the right to a state k on the left, while H_T^- performs the reverse function.

The tunnel matrix element $T_{k\uparrow q\uparrow}$ is given by:

$$T_{k\uparrow q\uparrow} = -\frac{\hbar^2}{2m}\int d\vec{s}(\Psi^*_{k\uparrow}\nabla\Psi_{q\uparrow} - \Psi_{q\uparrow}\nabla\Psi^*_{k\uparrow}) \qquad (2.28)$$

Where $\Psi_{k\uparrow}$ ($\Psi_{q\uparrow}$) is the single particle wavefunction for a state in the left-hand (right-hand) metal assuming infinite barrier, $d\vec{s}$ is the area unit vector of the dielectric interface. The integral can be evaluated anywhere within the oxide.

The junction current operator is given by:

$$I = e\frac{dN_R}{dt}$$

$$= \frac{ie}{\hbar}[H_T, N_R]$$

$$= \frac{ie}{\hbar}[H_T^+ - H_T^-]$$

$$= I_+ + I_- \qquad (2.29)$$

where I_+ transfers a particle from right to left and I_- is its Hermitian conjugate.

The tunnel junction is assumed to be in thermal equilibrium. The density matrix of the uncoupled system is determined by the junction Hamiltonian :

$$\rho = \frac{e^{\beta H}}{Z} \quad , \qquad Z = T_r e^{-\beta H} \qquad (2.30)$$

Where $H = H_R^0 + H_L^0 - \mu N$. The time-dependent potential term $eV(t)N_L$ in the system Hamiltonian (2.26) is assumed only to modulate the energy of electrons on the left-hand side and to be turned on adiabatically. The addition of this term to the left side Hamiltonian is offset by the change in left side chemical potential:

$$\mu_L(t) = \mu_R + eV(t) \qquad (2.31)$$

so that, the ensemble remains unaffected. In the Heisenberg picture, the single particle operator $C_k(t)$ on the left can be written as follows:

$$C_k(t) = C_k^0(t) \exp[-\frac{ie}{\hbar}\int^t dt'V(t')] \qquad (2.32)$$

Where $C_k^0(t)$ is the single particle operator in the absense of the applied field $V(t)$.

Separating the dc bias V_0 from $V(t)$, we can express the remaining time-varying contribution as Fourier components:

$$\exp\{-\frac{ie}{\hbar}\int^t dt'[V(t') - V_0]\}$$

$$= \int_{-\infty}^{\infty} d\omega' W(\omega') e^{-i\omega' t} \qquad (2.33)$$

then (2.32) becomes:

$$C_k(t) = C_k^0(t) \exp[-\frac{ieV_0 t}{\hbar}] \int_{-\infty}^{\infty} d\omega' W(\omega') e^{-i\omega t} \qquad (2.34)$$

The single particle operator on the right-side is just:

$$C_q(t) = C_q^0(t) \qquad (2.35)$$

The current operators (2.29) in the presence of the applied field can then be written as:

$$I_-(t) = I_-^0(t) \exp[-\frac{ieV_0 t}{\hbar}] \int_{-\infty}^{\infty} d\omega' W(\omega') e^{-i\omega' t} \qquad (2.36)$$

with

$$I_-^0(t) = -\frac{ie}{\hbar}\sum_{kq} T_{kq}^* c_q^{0+}(t) c_k^0(t) \tag{2.37}$$

and

$$I_+(t) = I_-^+(t) \tag{2.38}$$

From linear response theory [50], the current operator to the first order in the tunneling interaction is:

$$I^{(1)}(t) = I^0(t) + \frac{i}{\hbar}\int_0^t dt'[H_T^0(t'), I^0(t)]\theta(t-t') \tag{2.39}$$

Since for the uncoupled system $\langle I^0(t)\rangle = 0$, the expectation value for the total current can be written as:

$$\langle I(t)\rangle = -\frac{i}{\hbar}\int_{-\infty}^{\infty} dt'\langle[I(t),\ H_T(t')]\rangle_0\theta(t-t') \qquad (2.40)$$

$$= \frac{2}{e}\,\mathrm{Im}\int_{-\infty}^{\infty} dt' i\theta(t-t')\langle[I_+(t),\ I_-(t')]\rangle_0$$

Using (2.36), we get

$$\langle I(t)\rangle = \frac{2}{e}\,\mathrm{Im}\int_{-\infty}^{\infty} d\omega' d\omega'' W(\omega')W^*(\omega'')e^{-i(\omega'-\omega'')t}$$

$$\times \int_{-\infty}^{\infty} dt' i\theta(t-t')\langle[I_+^0(t),\ I_-^0(t)]\rangle_0$$

$$\times \exp[-i(\omega'+eV_0/\hbar)(t-t')] \qquad (2.41)$$

Define the retarded current commutator evaluated in the equilibrium system as:

$$X_{+-}(t-t') = i\theta(t-t')\langle[I_+^0(t),\ I_-^0(t')]\rangle_0 \qquad (2.42)$$

Then its Fourier transform is given by:

$$X_{+-}(\omega) = \frac{1}{2\pi} \int_{-\infty}^{\infty} d(t-t')X_{+-}(t-t')\exp[-i\omega(t-t')] \qquad (2.43)$$

Let us define the complex response function $j(\omega)$ as:

$$j(\omega) = \frac{4\pi}{e} X_{+-}(\omega) \qquad (2.44)$$

Then the average current (2.41) can be written as:

$$\langle I(t)\rangle = \mathrm{Im} \int_{-\infty}^{\infty} d\omega' d\omega'' W(\omega')W^*(\omega'')e^{-i(\omega'-\omega'')t}$$

$$\times\ j(\omega' + eV_0/\hbar) \qquad (2.45)$$

If the junction is only biased by a dc voltage (i.e. $V(t) = V_0$), then the Fourier components of the phase factor

(2.33) are given by:

$$W(\omega') = \delta(\omega') \tag{2.46}$$

then equation (2.45) becomes:

$$\langle I(t)\rangle = I_{dc}(V_0)$$

$$= \mathrm{Im}[j(eV_0/\hbar)] \tag{2.47}$$

Where $I_{dc}(V_0)$ is junction's dc current-voltage characteristic.

The real part of $j(\omega)$ is related to the imaginary part of $j(\omega)$ by the Kramers-Kronig relation [81]*:

---

* This is a direct consequence of the causality principle. In the classical treatment, the current carriers crossing the junction barrier are assumed to respond instantaneously to the applied external field. However, at higher frequencies, i.e. approaching the quantum regime, this response can no longer be assumed instantaneous, therefore one must use a causal response function to relate the tunneling current at time t to the voltage at all times t' < t. It is also well known that the Fourier transform of a causal function is a complex function with real and imaginary parts related by the Kramers-Kronig relation. As pointed out in [17], several important results are found in the quantum regime: both nonlinear resistive and reactive responses exist and are frequency dependent. The frequency dependent response is one of the cause of the observed mixer gain in the quantum regime.

$$\mathrm{Re}[j(\omega)] = P \int_{-\infty}^{\infty} \frac{d\omega'}{\pi} \frac{\mathrm{Im}[j(\omega')]}{\omega'-\omega} \tag{2.48}$$

$$\mathrm{Im}[j(\omega)] = I_{dc}(\hbar\omega/e) \tag{2.49}$$

Equation (2.45) completely describes the coupling between the quasiparticle tunneling current and the applied external field. As shown in (2.49), all the details of the superconducting quasiparticle tunnel junction given in (2.46) are governed by the quasiparticle dc I-V characteristic, where the external driving voltage, V(t), enters solely through the function $W(\omega)$. In the next section, the average current expression (2.45) will be used to derive the explicit quantum expressions for the elements of the conversion admittance matrix for the tunnel junction mixer.

2.4 Quantum mixer Theory

2.4.1 Introduction

The heterodyne receiver model described in section 2.2 can be adopted in the quantum generalization of the tunnel junction mixer theory. That is, in the quantum theory, the nonlinear tunnel junction is still represented as a multifrequency multiport network which is characterized by the admittance matrix Y (2.9). However, the elements of this matrix will now be calculated from the dynamic tunneling model described in section 2.3.2.

2.4.2 Quantum Expression for the Conversion Admittance Matrix

The voltage and current across a tunnel junction in the presence of a dc bias and local oscillator drive can be written as:

$$V(t) = V_0 + V_{LO}(t) \tag{2.50}$$

$$\langle I(t) \rangle = I_{LO}(t) \tag{2.51}$$

Assuming a periodic local oscillator drive, the induced average tunneling current (2.51) is:

$$\langle I(t)\rangle = I_{LO}(t)$$

$$= \mathrm{Im} \sum_{m=-\infty}^{\infty} e^{im\omega_p t}$$

$$\times \sum_{n=-\infty}^{\infty} W_{LO}(n\omega_p) W_{LO}^{*}((n+m)\omega_p) j(n\omega_p + eV_0/\hbar) \quad (2.52)$$

Where the phase factor (2.33):

$$\exp[-ie/\hbar \int^{t} dt' V_{LO}(t')] = \sum_{n=-\infty}^{\infty} W_{LO}(n\omega_p) e^{-in\omega_p t} \quad (2.53)$$

has been used. Including the small signal $v_{sig}(t)$ and $i_{sig}(t)$ in (2.50) and (2.51), we have:

$$V(t) = V_0 + V_{LO}(t) + v_{sig}(t) \quad (2.54)$$

$$\langle I(t)\rangle = I_{LO}(t) + i_{sig}(t) \quad (2.55)$$

Where the small signal $v_{sig}(t)$ and $i_{sig}(t)$ can be expressed as sideband frequency components:

$$v_{sig}(t) = \mathrm{Re} \sum_{m=-\infty}^{\infty} v_m e^{i\omega_m t}$$

$$= \frac{1}{2} \sum_{m=-\infty}^{\infty} (v_m^* e^{-i\omega_m t} + v_m e^{i\omega_m t}) \qquad (2.56)$$

$$i_{sig}(t) = \mathrm{Re} \sum_{m=-\infty}^{\infty} i_m e^{i\omega_m t}$$

$$= \frac{1}{2} \sum_{m=-\infty}^{\infty} (i_m^* e^{-i\omega_m t} + i_m e^{i\omega_m t}) \qquad (2.57)$$

To the lowest order of V_m, the Fourier components of the phase factor (2.53) can be approximated by:

$$W(\omega_p') = \sum_{n=-\infty}^{\infty} W_{LO}(n\omega_p)\{\delta(\omega_p'-n\omega_p)$$

$$+ \sum_{m'=-\infty}^{\infty} \frac{e}{2\hbar\omega_{m'}} [v^*_{m'} \delta(\omega'_p - n\omega_p - \omega_{m'})$$

$$- v_{m'} \delta(\omega'_p - n\omega_p + \omega_{m'})]\} \qquad (2.58)$$

the resultant current across the junction is then given by:

$$\langle I(t)\rangle = \mathrm{Im}\{W_{LO}(n\omega_p) W^*_{LO}(n'\omega_p)$$

$$\times j(n\omega_p + eV_0/\hbar)\exp[-i(n-n')\omega_p t]$$

$$+ \sum_{m'} \frac{eV_{m'}}{2\hbar\omega_{m'}} \sum_{nn'} W_{LO}(n\omega_p) W^*_{LO}(n'\omega_p)$$

$$\times [j(n\omega_p + eV_0/\hbar) - j(n\omega_p - \omega_m + eV_0/\hbar)]$$

$$\times \exp[-i(n\omega_p - n'\omega_p - \omega_{m'})t]$$

$$+ \sum_{m'} \frac{eV^*_{m'}}{2\hbar\omega_{m'}} W_{LO}(n\omega_p) W^*_{LO}(n'\omega_p)$$

$$\times [j^*(n\omega_p + \omega_{m'} + eV_0/\hbar) - j^*(n'\omega_p + eV_0/\hbar)]$$

$$\times \exp[-i(n\omega_p - n'\omega_p + \omega_m)t]$$

$$+ [\text{higher order terms of } v_m \text{ and } v_m^*]\} \tag{2.59}$$

On the other hand, the average tunneling current (2.55) can be written as:

$$\begin{aligned} \langle I(t)\rangle &= I_{LO}(t) + i_{sig}(t) \\ &= I_{LO}(t) + \frac{1}{2}\sum_{m=-\infty}^{\infty}[(\sum_{m'} Y_{mm'}^* v_{m'}^*)e^{-i\omega_m t} \\ &\quad + (\sum_{m'} Y_{mm'} v_{m'})e^{i\omega_m t}] \end{aligned} \tag{2.60}$$

Where the small signal current-voltage relation (2.9) has been used. Substituting (2.52) into (2.60) and comparing with (2.59), the matrix elements $Y_{mm'} = G_{mm'} + jB_{mm'}$ can be identified as:

$$G_{mm'} = \mathrm{Im}(-i)\frac{e}{2\hbar\omega_{m'}} \sum_{nn'=-\infty}^{\infty} W_{LO}(n\omega_p)W_{LO}^*(n'\omega_p)\delta_{m-m',n'-n}$$

$$\times \{[j(n\omega_p+eV_0/\hbar) - j(n\omega_p-\omega_{m'}+eV_0/\hbar)]$$

$$- [j^*(n'\omega_p+\omega_{m'}+eV_0/\hbar) - j^*(n'\omega_p+eV_0/\hbar)]\}$$

and (2.61)

$$B_{mm'} = \mathrm{Re}(-i)\frac{e}{2\hbar\omega_{m'}} \sum_{nn'=-\infty}^{\infty} W_{LO}(n\omega_p)W^*_{LO}(n'\omega_p)\delta_{m-m',n'-n}$$

$$\times \{[j(n\omega_p+eV_0/\hbar) - j(n\omega_p-\omega_{m'}+eV_0/\hbar)]$$

$$- [j^*(n'\omega_p+\omega_{m'}+eV_0/\hbar) - j^*(n'\omega_p+eV_0/\hbar)]\}$$

Where $B_{mm'}$ is the reactive mixing term which only appears in quantum theory and has no classical analogue. Replacing the matrix elements $Y_{mm'}$ (2.10) by (2.61), the performance of the tunnel junction mixer can then be evaluated exactly as described in the generalized heterodyne receiver models (2.13 - 2.25).

2.5 SIS Mixer Noise Theory

2.5.1 Introduction

The sources of noise in a practical SIS mixer are (1) shot noise due to local oscillator current $I_{LO}(t)$ (2.51) tunneling through the junction barrier, (2) thermal noise generated from each sideband termination, and (3) Noise arising from the quantum fluctuations of the input radiation fields. Since the complete quantum mechanical analysis, which quantizes "both" the input radiation fields and the charge carriers, is not yet developed for tunnel junction mixer, and the noise due to the fluctuations of the applied radiation field is small, $\hbar\omega/k$ = 5.5 K at 115 GHz, it is omitted in this analysis.

Shot and thermal noise sources can be included in the mixer equivalent circuit by connecting an equivalent noise current source to each sideband termination as shown in Fig. 2-2. The equivalent IF output noise current due to the noise current at all the sideband frequencies can be determined by equation (2.19).

2.5.2 Shot Noise

In a practical SIS mixer, the mixer noise should be dominated by shot noise which is due to fluctuations in the local oscillator current $I_{LO}(t)$ tunneling through the junction barrier. Rogovin and Scalapino [50] have studied the current fluctuation phenomenon in tunnel junctions and have found that it can be simply related to the junction's dc I-V characteristic. Tucker [73] extented this calculation and constructed a complete shot noise model for the tunnel junction mixer.

In Tucker's model, shot noise is represented by a noise generator $[I(t) - \langle I(t)\rangle]$ placed in parallel with an ideal "noiseless" mixer. $I(t)$ is the junction's current operator over a time interval 'T', and $\langle I(t)\rangle$ is the expectation value of $I(t)$. As shown in Fig. 2-2, this noise generator can be replaced by a set of current generators $I_m(t)$, one at each sideband port. In that case:

$$I_m(t) \approx \int_{\omega_m-\pi B}^{\omega_m+\pi B} d\omega'[I_T(\omega')e^{-i\omega' t} + I_T(-\omega')e^{i\omega' t}]$$

$$\approx 2B[I_T(\omega_m)e^{-i\omega_m t} + I_T(-\omega_m)e^{i\omega_m t}] \qquad (2.62)$$

where $I_T(\omega)$ is the Fourier component of the current operator $I(t)$ defined as:

$$I_T(\omega) = \int_{-T/2}^{T/2} \frac{dt'}{2\pi} I(t') e^{i\omega t'} \tag{2.63}$$

The effective noise current operator at the output frequency ω_0 is given by (2.19):

$$I_T^{eff}(\omega_0) = \sum_{m'} \lambda^*_{om'} I_T(\omega_{m'}) \tag{2.64}$$

At the output frequency ω_0, the mean square noise current within the bandwidth B is:

$$\langle [I_0]^2 \rangle_{LO} = \lim_{T\to\infty} \frac{1}{T} \int_{-T/2}^{T/2} dt \langle [I_0(t)]^2 \rangle \tag{2.65}$$

Where $I_0(t)$ can be calculated by equation (2.62).

Substituting equation (2.64) into (2.65), we have:

$$\langle [I_0]^2 \rangle_{LO} = B \lim_{T\to\infty} \frac{4\pi^2}{T} \langle [I_T^{eff}(\omega_0),\ I_T^{eff}(-\omega_0)]_+ \rangle$$

$$= B \sum_{m,m'} \lambda_{Om} \lambda_{Om'}^{*} H_{mm'} \qquad (2.66)$$

Where $[\quad]_+$ denotes an anticommutator and $H_{mm'}$ is the current correlation matrix which is defined as:

$$H_{mm'} = \lim_{T\to\infty} \frac{4\pi^2}{T} \langle [I_T(-\omega_m),\ I_T(\omega_{m'})]_+ \rangle \qquad (2.67)$$

For a tunnel junction in the presence of a periodic local oscillator drive, the current correlation matrix (2.67) can be expressed as [73]:

$$H_{mm'} = e \sum_{n,n'=-\infty}^{\infty} W_{LO}(n\omega_p) W_{LO}^{*}(n'\omega_p) \delta_{m-m',n'-n}$$

$$\times \{\coth[\beta(eV_0 + n'\hbar\omega_p + \hbar\omega_{m'})/2]$$

$$\times I_{dc}(V_0 + n'\hbar\omega_p/e + \hbar\omega_{m'}/e)$$

$$+ \coth[\beta(eV_0 + n\hbar\omega_p - \hbar\omega_{m'})/2]$$

$$\times I_{dc}(V_0 + n\hbar\omega_p/e - \hbar\omega_{m'}/e)\} \qquad (2.68)$$

where $W_{LO}(n\omega)$ is the Fourier component of the phase factor given by equation (2.53), and $\beta = 1/kT$.

The equivalent USB current source I_s which corresponds to the same mean square noise current $\langle[I_0]^2\rangle$ at the output frequency can be calculated from (2.19):

$$\langle[I_0]^2\rangle_{LO} = \frac{1}{2}|\lambda_{01}|^2\langle[I_1]\rangle_{LO}^2 \qquad (2.69)$$

and the power corresponding to such fluctuations is:

$$P^{shot} = \frac{\langle [I_1]^2 \rangle_{LO}}{8G_1}$$

$$= \frac{1}{4G_1 |\lambda_{01}|^2} \langle [I_0]^2 \rangle_{LO} \qquad (2.70)$$

2.5.3 Thermal Noise

The thermal noise generated from the m-th sideband termination can be represented by an equivalent current source with mean square amplitude [73]:

$$\langle [i_m]^2 \rangle = \frac{4\hbar\omega_m B}{[\exp(\hbar\omega_m/kT_B)-1] \times R} \qquad (2.71)$$

Where R is the resistive termination, T_B is the physical temperature of the termination and B is the effective bandwidth at output frequency. These noise components will be down-converted into the IF output port and are equivalent to a single noise current source at IF with mean square amplitude given by:

$$\langle[i_0{}^2]\rangle_{thermal} = B_{m\neq 0,1}|\lambda_{0m}|^2 \frac{4\hbar\omega_m}{[\exp(\hbar\omega_m/kT_B)-1] \times R} \tag{2.72}$$

As usual, noise generated by signal and load terminations are not included.

Referred to the upper sideband, the signal power corresponding to these fluctuations can be calculated as in equation (2.70):

$$P^{thermal} = \frac{1}{4G_1|\lambda_{01}|^2} \langle[i_0]^2\rangle_{thermal} \tag{2.73}$$

2.5.4 Total SIS Mixer Noise

From the previous sections, the minimum detectable power P_{det}^{min} of the SIS mixer is:

$$P_{det}^{min} = P^{shot} + P^{thermal} \tag{2.74}$$

The sensitivity of the mixer is usually characterized

in terms of the equivalent input noise temperature T_M of the mixer, where T_M is defined as the temperature of the input termination of a noiseless but otherwise identical mixer, which would deliver to the IF load the same noise power as the actual mixer delivers when it is connected to a noiseless input termination. According to this definition, the noise temperature refers to upper sideband of a practical SIS mixer is given by:

$$T_M = \frac{P_{det}^{min}}{kB}$$

$$= \frac{\{\langle[I_0]^2\rangle_{LO} + \langle[i_0]^2\rangle_{thermal}\}}{4kBG_1|\lambda_{01}|^2} \tag{2.75}$$

Here, the Rayleigh-Jeans limit has been used to define the equivalent temperature of the input termination from the minimum detectable power.

2.6 The 3-Frequency Approximation

The simplest applicable heterodyne receiver model is the 3-port Y mixer model in which we only consider the USB frequency (ω_1), LSB frequency (ω_{-1}), and IF frequency (ω_0). The local oscillator waveform across the junction is taken to be sinusoidal:

$$V(t) = V_0 + V_{LO} \cos(\omega_p t) \tag{2.76}$$

and all higher harmonics and their sidebands are assumed to be shorted either by the junction capacitance or by an external tuning circuit. The mixer conversion admittance matrix (2.9) is then reduced to a complex 3 × 3 matrix. Assuming small IF frequency, $\omega_0 << \omega_p$, and $\omega_1 \approx \omega \approx \omega_{-1}$, the admittance matrix elements:

$$Y_{ik} = G_{ik} + jB_{ik} \quad , \quad i,k = -1,0,1 \tag{2.77}$$

have been explicitly evaluated by Tucker [73] as:

$$G_{00} = \sum_{n=-\infty}^{\infty} J_n^2(\alpha)\frac{d}{dV_0}I_{dc}(V_0+n\hbar\omega_p/e)$$

$$G_{10} = G_{-10}$$

$$= \frac{1}{\alpha}\sum_{n=-\infty}^{\infty} nJ_n^2(\alpha)\frac{d}{dV_0}I_{dc}(V_0+n\hbar\omega_p/e)$$

$$G_{01} = G_{0-1}$$

$$= \frac{e}{\hbar\omega_p}\sum_{n=-\infty}^{\infty} J_n(\alpha)[J_{n-1}(\alpha) - J_{n+1}(\alpha)]I_{dc}(V_0+n\hbar\omega_p/e)$$

$$G_{11} = G_{-1-1} \tag{2.78}$$

$$= \frac{e}{2\hbar\omega_p}\sum_{n=-\infty}^{\infty} [J_{n-1}^2(\alpha) - J_{n+1}^2(\alpha)]I_{dc}(V_0+n\hbar\omega_p/e)$$

$$G_{1-1} = G_{-11}$$

$$= \frac{e}{2\hbar\omega_p}\sum_{n=-\infty}^{\infty} J_n(\alpha)[J_{n-2}(\alpha) - J_{n+2}(\alpha)]I_{dc}(V_0+n\hbar\omega_p/e)$$

$$B_{10} = -B_{-10}$$

$$= \frac{1}{2}\sum_{n=-\infty}^{\infty} J_n(\alpha)[J_{n-1}(\alpha)-J_{n+1}(\alpha)]\frac{d}{dV_0}I_{KK}(V_0+n\hbar\omega_p/e)$$

$$B_{11} = -B_{-1-1}$$

$$= \frac{e}{2\hbar\omega_p} \sum_{n=-\infty}^{\infty} [J_{n-1}^2(\alpha)-2J_n^2(\alpha)+J_{n+1}^2(\alpha)] I_{KK}(V_0+n\hbar\omega_p/e)$$

$$B_{1-1} = -B_{-11}$$

$$= \frac{e}{2\hbar\omega_p} \sum_{n=-\infty}^{\infty} [J_{n-2}(\alpha)J_n(\alpha) - 2J_{n-1}(\alpha)J_{n+1}(\alpha)$$

$$+ J_n(\alpha)J_{n+2}(\alpha)] I_{KK}(V_0+n\hbar\omega_p/e)$$

$$B_{00} = B_{01} = B_{0-1} = 0$$

Where $J_n(\alpha)$ is the Bessel function of the first kind of order n, and the argument α is given by:

$$\alpha = \frac{eV_{LO}}{\hbar\omega_p} \tag{2.79}$$

$I_{dc}(V)$ is the junction's dc I-V characteristic in the absence of local oscillator power, and

$$I_{KK}(V) = \frac{1}{\pi} P \int_{-\infty}^{\infty} \frac{dV'}{V-V'} I_{dc}(V') \tag{2.80}$$

is the Kramers-Kronig transform of the $I_{dc}(V)$ and is the real part of the current response function (2.48).

The dc component of the tunneling current (with the LO applied) is given by:

$$I_0 = \sum_{n=-\infty}^{\infty} J_n^2(\alpha) I_{dc}(V_0 + n\hbar\omega_p/e) \tag{2.81}$$

and the component at local oscillator frequency ω is:

$$I_P = \frac{2}{\alpha} \sum_{n=-\infty}^{\infty} n J_n^2(\alpha) I_{dc}(V_0 + n\hbar\omega_p/e) \tag{2.82}$$

$$+ j \sum_{n=-\infty}^{\infty} J_n(\alpha)[J_{n-1}(\alpha) - J_{n+1}(\alpha)] I_{KK}(V_0 + n\hbar\omega_p/e)$$

Assume $\omega_1 = \omega_s$ and $\omega_{-1} = \omega_i$ are the signal and image frequency respectively*, and let $Y_1 = Y_s = G_s + jB_s$, $Y_{-1} = Y_i = G_i - jB_i$ and $Y_0 = Y_L = G_L + jB_L$ be the source, (conjugate) image and load terminations, the augmented impedance matrix Z' (2.16) can be expressed as:

---

* As indicated by Torrey & Whitmer [70] and Saleh [54], no loss of generality results from this assumption.

$$Z' = \begin{bmatrix} (G_{11}+G_s)+j(B_{11}+B_s) & G_{10}+jB_{10} & G_{1-1}+jB_{1-1} \\ G_{01} & (G_{00}+G_L)+jB_L & G_{01} \\ G_{1-1}-jB_{1-1} & G_{10}-jB_{10} & (G_{11}+G_i)-j(B_{11}+B_i) \end{bmatrix}^{-1} \tag{2.83}$$

Once Z' is obtained, the mixer conversion loss, input and output impedance can be calculated from equations (2.22), (2.24) and (2.25) respectively.

In the 3-port model, the explicit form of the current correlation matrix elements $H_{mm'}$, which characterize the noise properties of the mixer, are also given by Tucker [73]:

$$H_{00} = 2e \sum_{n=-\infty}^{\infty} J_n^2(\alpha)\coth[\beta(eV_0+n\hbar\omega_p)/2]I_{dc}(V_0+n\hbar\omega_p/e)$$

$$H_{10} = H_{-10} = H_{01} = H_{0-1}$$

$$= \frac{2e}{\alpha} \sum_{n=-\infty}^{\infty} nJ_n^2(\alpha)\coth[\beta(eV_0+n\hbar\omega_p)/2]I_{dc}(V_0+n\hbar\omega_p/e)$$

$$H_{11} = H_{-1-1} \tag{2.84}$$

$$= e \sum_{n=-\infty}^{\infty} [J_{n+1}^2(\alpha) + J_{n-1}^2(\alpha)]$$

$$\times \coth[\beta(eV_0+n\hbar\omega_p)/2] I_{dc}(V_0+n\hbar\omega_p/e)$$

$$H_{1-1} = H_{-11}$$

$$= 2e \sum_{n=-\infty}^{\infty} J_{n+1}(\alpha) J_{n-1}(\alpha) \coth[\beta(eV_0+n\hbar\omega_p)/2]$$

$$\times I_{dc}(V_0+n\hbar\omega_p/e)$$

Therefore, in the 3-port model, the shot noise contribution to the input mixer noise temperature is given as:

$$T_M^{shot} = \frac{1}{4k|\lambda_{01}|^2} \{(|\lambda_{01}|^2 + |\lambda_{0-1}|^2)H_{11}$$

$$+ 2(\mathrm{Re}[\lambda_{01}] + \mathrm{Re}[\lambda_{0-1}])H_{10} + H_{00} \qquad (2.85)$$

$$+ 2(\mathrm{Re}[\lambda_{01}]\mathrm{Re}[\lambda_{0-1}] + \mathrm{Im}[\lambda_{01}]\mathrm{Im}[\lambda_{0-1}])H_{1-1}\}$$

where

$$\lambda_{0m} = \frac{Z'_{0m}}{Z'_{00}} \qquad , \; m = -1,\ 0,\ 1 \tag{2.86}$$

In the 3-port model, only the image termination generates thermal noise, which is given by:

$$T_M^{thermal} = \frac{|\lambda_{0-1}|^2 \times \hbar\omega_i G_i}{4k|\lambda_{01}|^2 \exp[\hbar\omega_i/(kT_B)-1]} \tag{2.87}$$

and the total input mixer noise temperature is:

$$T_M = T_M^{shot} + T_M^{thermal} \tag{2.88}$$

Theoretical calculations based on the formulae developed in this section will be used later to compare with the experimental results.

There are two examples of special interest which will be discussed below.

2.6.1 Equal Signal and Image Termination

If the image termination is equal to the complex conjugate of the signal source admittance, $Y_i = Y_s^* = G_s - jB_s$, the signal to IF conversion gain can be written as [17]:

$$L_{IF}^{-1} = \frac{4G_sG_LG_{01}^2[(G_s+G_{11}-G_{1-1})^2 + (B_s+B_{11}-B_{1-1})^2]}{(G_{00}+G_L)^2 \times D(G_s,B_s,G_L)} \qquad (2.89)$$

where

$$\begin{aligned} D(G_s,B_s,G_L) = {} & \{G_s - [G_{01}G_{10} / (G_{00} + G_L) - G_{11}]\}^2 \\ & + \{B_s - [G_{01}B_{10} / (G_{00} + G_L) - B_{11}]\}^2 \\ & - \{[G_{1-1} - G_{01}G_{10} / (G_{00} + G_L)]^2 \\ & + [B_{1-1} - G_{01}B_{10} / (G_{00} + G_L)]^2\} \qquad (2.90) \end{aligned}$$

Note that the function $D(G_s,B_s,G_L)$ also depends on the junction dc I-V nonlinearity, dc bias (V_0) and pump voltage (V_{LO}) through the admittance matrix elements Y_{mm}, (2.61).

It can be verified from equation (2.89) [17] that for a given tunnel junction mixer with dc bias V_0 and pump voltage V_{LO}, connected to a load conductance G_L, it is possible to achieve infinite conversion gain if and only if $D(G_s,B_s) = 0$.

We can determine the source admittance region in which a given tunnel junction mixer will exhibit infinite gain:

If $D(G_s,B_s) = 0$, equation (2.10) can be rearranged as follows:

$$(G_s - X_0)^2 + (B_s - Y_0)^2 = r^2 \tag{2.91}$$

with

$$r = \{[G_{1-1} - G_{01}G_{10} / (G_{00} + G_L)]^2 + [B_{1-1} - G_{01}B_{10} / (G_{00} + G_L)]^2\}^{1/2} \tag{2.92}$$

and

$$X_0 = G_{01}G_{10} / (G_{00} + G_L) - G_{11} \tag{2.93}$$

$$Y_0 = G_{01}B_{10} / (G_{00} + G_L) - B_{11} \tag{2.94}$$

This is the equation of a circle in the source admittance plane with radius r and centered at (X_0, Y_0). Here X_0, Y_0 and r only depend on the junction's dc I-V characteristic, dc bias point and pump voltage. Since in the real tuning structure $G_s > 0$, therefore, infinite gain is attainable only on the portion of circle with $G_s > 0$.

The mixer's IF output impedance (2.25) is real and is:

$$Z_{00}' = R_d$$

$$= [(G_s + G_{11})^2 + (B_s + B_{11})^2 - (G_{1-1}^2 + B_{1-1}^2)]$$

$$/ [G_{00} \times D(G_s, B_s, G_L=0)] \qquad (2.95)$$

with

$$D(G_s, B_s, G_L=0)$$

$$= [G_s-(G_{01}G_{10}/G_{10}-G_{11})]^2 + [B_s-(G_{01}B_{10}/G_{00}-B_{11})]^2 \qquad (2.96)$$

$$+ [(G_{1-1}-G_{01}G_{10}/G_{00})^2 + (B_{1-1}-G_{01}B_{10}/G_{00})^2]$$

Where R_d is the differential resistance of the pumped dc I-V curve. Within a certain range of the parameters V_0, V_{LO}, G_s and B_s, the function $D(G_s,B_s,G_L=0) \leqq 0$. That is, the output impedance of an SIS mixer can be infinite or even negative. This has been verified in the experiments (see section 6.3.1).

For a given tunnel junction, a negative output impedance region can be determined in the source admittance plane. As shown above, the equation $D(G_s,B_s,G_L=0) = 0$ is again a circle on the source admittance plane with radius r and centered at (X_0, Y_0) which is given by:

$$r = \{[G_{1-1}-G_{01}G_{10}/G_{00}]^2 + [B_{1-1}-G_{01}B_{10}/G_{00}]^2\}^{1/2} \tag{2.97}$$

and

$$X_0 = G_{01}G_{10} / G_{00} - G_{11} \tag{2.98}$$

$$Y_0 = G_{01}B_{10} / G_{00} - B_{11} \tag{2.99}$$

R_d is infinite on the circle. Within the circle, the output impedance is negative. Usually for a given junction, $X_0 < 0$. However, for a real tuning structure, we are limited to the case requiring $G_s > 0$. Therefore, for a given junction, the condition for achieving negative output impedance is

$$r > |X_0| \tag{2.100}$$

or

$$[(G_{1-1}-G_{01}G_{10}/G_{00})^2 + (B_{1-1}-G_{01}B_{10}/G_{00})^2]^{1/2}$$

$$> G_{11} - G_{01}G_{10}/G_{00} \tag{2.101}$$

2.6.2 Short-circuited Image Case

Mixers operating in single sideband mode are of particular advantage for many astronomical applications since the noise coming from the celestial background and our atmosphere at the image frequency is not received, which makes the effective sensitivity of the system better for a single sideband receiver. Previous computer simulation [63] has shown that large conversion efficiency

and large dynamic range are possible for a single sideband SIS mixer. Techniques developed in previous sections can also be used to study this special case.

Here, we assume that the image frequency wave is short circuited, that is, $Y_i = \infty$. The mixer conversion admittance matrix (2.16) reduces to a 2 × 2 matrix and the conversion loss of the mixer can be expressed in the following simple form:

$$L_C = \frac{[G_s+G_{11}-G_{01}G_{10}/(G_{00}+G_L)]^2+[B_s+B_{11}-G_{01}B_{10}/(G_{00}+G_L)]^2}{4G_sG_LG_{01}^2/(G_{00}+G_L)^2} \tag{2.102}$$

This can be rearranged to give the same form as in (2.91), i.e. constant conversion loss circles in the source admittance plane with radius:

$$\begin{aligned} r = \{&4L^2G_L^2G_{01}^4/(G_{00}+G_L)^4 \\ &+ 4LG_LG_{01}^2[G_{01}G_{10}/(G_{00}+G_L)-G_{11}]/(G_{00}+G_L)^2\}^{1/2} \end{aligned} \tag{2.103}$$

and

$$X_0 = 2LG_L G_{01}^2/(G_{00}+G_L)^2 + G_{01}G_{10}/(G_{00}+G_L) - G_{11} \tag{2.104}$$

$$Y_0 = G_{01}B_{10}/(G_{00}+G_L) - B_{11} \tag{2.105}$$

Hence, in the shorted-image case, the source admittance in which a tunnel junction mixer with given parameters (G_L, V_0 and V_{L0}) will exhibit constant conversion loss is constrained to lie on a circle in the source admittance plane with radius r and centered at (X_0, Y_0). The condition $G_s > 0$ limits the accessible part of the source admittance plane.

In shorted-image case, the output admittance, $Y_{out} = G_{out} + jB_{out}$, is no longer real and is given by:

$$G_{out} = \frac{(G_s+G_{11})[G_{00}(G_s+G_{11})-G_{01}G_{10}]+(B_s+B_{11})[G_{00}(B_s+B_{11})-G_{01}B_{10}]}{(G_s+G_{11})^2+(B_s+B_{11})^2} \tag{2.106}$$

$$B_{out} = \frac{(G_s+G_{11})[G_{00}(B_s+B_{11})-G_{01}B_{10}]-(B_s+B_{11})[G_{00}(B_s+B_{11})-G_{01}B_{01}]}{(G_s+G_{11})^2+(B_s+B_{11})^2} \tag{2.107}$$

For optimum operation, it is assumed that the output impedance is conjugately terminated by the load impedance, $Z_L = Z_{out}$. High or even infinite gain is possible in this case. Within a certain range of the source admittance, the output conductance (2.106) can be zero or even negative. Following the same technique described above, equation (2.106) can be put into the form of equation of a circle with:

$$r = \left[\frac{(G_{00}G_{01})^2 + (B_{10}G_{01})^2}{2G_{00}^{\ 2}}\right]^{1/2} \tag{2.108}$$

and

$$X_0 = \frac{G_{01}G_{10}}{2G_{00}} - G_{11} \tag{2.109}$$

$$Y_0 = \frac{G_{01}B_{10}}{2G_{00}} - B_{11} \tag{2.110}$$

The additional constraint that $G_s > 0$ implies that

$r > X_0$, therefore, the condition to achieve zero or even negative output conductance is:

$$\frac{G_{01}G_{10}}{2G_{00}} - G_{11} < \left[\frac{(G_{01}G_{10})^2 + (G_{01}B_{10})^2}{2G_{00}^{\ 2}}\right]^{1/2} \qquad (2.111)$$

2.7 Theory of Arrays

It has been shown [19] that the mixer performance of an N junction array should be the same as that of a single junction which has the same overall impedance provided that (a) current is in phase all along the array and (b) that all of the junctions of the array are identical. Under these assumptions, Tucker's theory for single junction can be applied to an N junction array by using the following transformation:

	SINGLE JUNCTION	ARRAY	
Current Scale	$I(V)$	$NI(NV)$	(2.112)
Voltage Scale	V	NV	
Induced Photon Step	$\hbar\omega/e$	$N\hbar\omega/e$	
Admittance Matrix Element	$Y_{mm'}(V,\hbar\omega/e)$	$Y_{mm'}(NV,N\hbar\omega/e)$	
Source Admittance	Y_s	Y_s	

Thus the conversion loss for the array will be the same as for the single junction with the same over-all impedance if the external impedance stays the same with the dc and LO voltage scaled by a factor N. On the other hand, the required LO power and the RF saturation power

will be N^2 larger for an N-junction array than for a single junction. The shot noise current $< [I_0]^2 >_{LO}$ for an array has been shown to be identical to that of a single junction of the same over-all impedance [19]. Since the mixer conversion loss and the external impedance are the same in both cases, the equivalent input shot noise should be the same for array and single jucntion.

2.8 Computer Modeling

As shown in previous sections, in the quantum mixer theory, the mixer performance is completely determined by the junction's dc I-V characteristic and the embedding admittances at all relevant frequencies. Based on this, a computer program was developed to determine the mixer performance.

In these calculations, the junction capacitance is treated as an external circuit element and is combined with the embedding admittace. The 3-frequency approximation was used in the simulation. This is equivalent to assuming that all the higher harmonics and sidebands above $\omega_p + \omega_0$ are short-circuited by the junction's capacitance. This is a reasonable representation of our experiments since the junctions' $\omega R_N C$ product is usually larger than 7.

In order to compare the theoretical predictions with experimental results, the experimental dc I-V curve of the junction was used in the simulation. Furthermore, the embedding admittance, seen by the SIS junction at signal, image and LO frequencies, is a function of the backshort position and is determined by direct admittance measurements on a 40X scale model of the mixer block.

Given the input pump power from the experiment and the embedding admittance at the LO frequency from scale model measurements, the pump voltage V_{LO} impressed across the junction can be determined from the following equation:

$$P_{LO} = \frac{1}{8G_{LO}}[(V_{LO}G_{LO}+I_{\omega_p})^2+(V_{LO}B_{LO}+I_{-\omega_p})^2] \qquad (2.113)$$

Where I_{ω_p} ($I_{-\omega_p}$) is the real (imaginary) part of the tunneling current at the local oscillator frequency (2.82). Since the argument of the Bessel function is V_{LO} dependent, equation (2.113) can be solved iteratively.

With all these experimental data input, this program can predict the mixer conversion loss, equivalent input noise temperature, input and output impedance of the mixer. Experimental results are compared with those calculations in chapter 6.

2.8.1 Outline of the Computing Method

The calculation procedures can be roughly divided into three parts: (1) given the junction's dc I-V curve, calculate the Kramers-Kronig transform, (2) given I_{dc}, I_{KK}, dc bias and pump voltage, calculate the mixer conversion admittance matrix elements $Y_{mm'}$, with m,m' =

-1, 0, 1, (3) given the source, image and load admittances together with $Y_{mm'}$, calculate the mixer conversion loss, mixer noise temperature, input and output impedance.

The experimental dc I-V curve was fed in at constant voltage increments with the incremental voltage equal to one tenth of the photon step, i.e. $V = \hbar\omega_p/(10e)$. For voltage between $2\Delta/e - \hbar\omega_p/(2e)$ and $2\Delta/e + \hbar\omega_p/(2e)$, exponential interpolation was used between the input points, whereas a third order polynomial was used outside this voltage range. Given dc I-V curve, the next task is to evaluate it's Kramers-Kronig transfrom:

$$I_{KK}(V) = \frac{1}{\pi} P \int \frac{dV'}{V'-V} I_{dc}(V') \qquad (2.80)$$

This integral is divergent. However, I_{KK} can be shifted by an arbitrary linear term (corresponding to adding a fixed conductance across the junction) without affecting any observed quantities such as the tunneling current [80] and it is also known that above the gap voltage, the dc I-V curve should exponentially approach a straight line with a slope equal to junction's normal conductance G_N. We can therefore subtract the ohmic portion from this integral and modify equation (2.80) as

follows [75]:

$$I_{KK}(V) = \frac{1}{\pi} P \int \frac{dV'}{V'-V}[I_{dc}(V') - G_N V'] \tag{2.114}$$

Since $I_{dc}(V)$ exponentially approaches the normal conductance line, $I = G_N V$, let V_{MAX} be the voltage where:

$$I_{dc}(V_{MAX}) - G_N V_{MAX} = \varepsilon \qquad , \varepsilon \to 0 \tag{2.115}$$

then equation (2.114) can be written as:

$$I_{KK}(V) = \frac{1}{\pi} P \int_{-V_{MAX}}^{V_{MAX}} \frac{dV'}{V'-V}[I_{dc}(V') - G_N V']$$

$$+ \text{ correction term} \tag{2.116}$$

Usually, by choosing $V_{MAX} = 3V_{gap}$, the correction term in (2.116) is small enough to be discarded. Notice that at $V' = V$, the integrand in equation (2.116) diverges. To remove this singularity, (2.116) can be rewritten as

follows:

$$I_{KK}(V) = \frac{1}{\pi}\int_{-V_{MAX}}^{V_{MAX}} \frac{dV'}{V'-V}\{[I_{dc}(V')-G_N V'] - [I_{dc}(V)-G_N V]\}$$

$$+ \frac{1}{\pi}\int_{-V_{MAX}}^{V_{MAX}} \frac{dV'}{V'-V}[I_{dc}(V) - G_N V]$$

$$= I_{KK}^{(1)}(V) + I_{KK}^{(2)}(V) \qquad (2.117)$$

The second integal can be evaluated as follows:

$$I_{KK}^{(2)} = \frac{1}{\pi}[I_{dc}(V) - G_N V]\ln\left|\frac{V_{MAX} - V}{V_{MAX} + V}\right| \qquad (2.118)$$

and the integrand in the first integral is no longer singular at V' = V:

$$\lim_{V'\to V} \frac{1}{V'-V}\{[I_{dc}(V') - G_N V'] - [I_{dc}(V) - G_N V]\}$$

$$= \lim_{V' \to V} \frac{I_{dc}(V') - I_{dc}(V)}{V'-V} - \lim_{V' \to V} \frac{G_N V' - G_N V}{V'-V}$$

$$= \left. \frac{dI_{dc}(V')}{dV'} \right|_{V'=V} - G_N \qquad (2.119)$$

which is the difference between the junction's <u>real</u> differential conductance and the junction's <u>normal</u> conductance and can be calculated from the junction's dc I-V curve. The first integral in (2.119) can therefore be evaluated by numerical integration. The resultant Kramers-Kronig transform I_{KK} used in the simulation is:

$$I_{KK}(V) = \frac{1}{\pi}[I_{dc}(V) - G_N V] \ln \left| \frac{V_{MAX} - V}{V_{MAX} + V} \right| \qquad (2.120)$$

$$+ \frac{1}{\pi} \int_{-V_{MAX}}^{V_{MAX}} \frac{dV'}{V'-V} \{[I_{dc}(V') - G_N V'] - [I_{dc}(V) - G_N V]\}$$

Assuming an ideal SIS I-V characteristic [22,80] and $V_{MAX} = 3V_{gap}$, the calculated Kramers-Kronig transform I_{KK} using (2.120) is found to be within 1% of the analytical

results over most of the region. About 20% error was found at the gap voltage point. However, since in experiments, the bias points of the best performance are always in the middle of one of the photon steps, only the points with $V = 2\Delta/e - \hbar\omega_p/(2e) \pm n\hbar\omega_p/e$, $n = 0, \pm 1, \pm 2, \ldots$, were used in calculations. Therefore this error won't cause any problem in the whole analysis.

Given $I_{KK}(V)$, it is straight forward to calculate the admittance matrix elements G_{ij} and B_{ij} and current correlation matrix elements H_{ij} from (2.78) and (2.84). Note that since higher order Bessel function approach zero for small argument, only the most important 15 terms, i.e. $n = -7, \ldots, 7$, in the infinite series (2.78) and (2.84) are counted in this calcualtion.

Having Y_{ij} and H_{ij} for a particular pump amplitude and bias voltage, the mixer properties can be evaluated for any source and load admittance.

CHAPTER 3. JUNCTION DESIGN AND FABRICATION

3.1 Introduction

For practical mixer application, superconducting tunnel junctions should have the following properties: long term stability, good thermal recyclability, high critical temperature (which will simplify cryogenic cooling), high mechanical strength, good adhesion between metal and substrate, and low leakage current below the gap voltage, I-V curve as close as possible to the ideal case. Lead alloy junctions and niobium junctions, which have been shown to fullfill the above requirements, are used in these SIS mixer experiments. The design and fabrication of the junctions used in this work will be described in this chapter.

3.2 Optimum Junction Parameters for Mixer Applications

There are several parameters of the superconducting tunnel junction which have to be optimized to achieve the best mixer performance. The two most fundamental electrical properties of the junction are the normal state

resistance R_N and the inherent junction capacitance C_J. However, with given junction materials and fabrication process, the only two parameters which can be directly controlled in fabricating the junction are the junction area A, and the maximum dc Josephson current density j_C. The focus of this section is to determine the optimum fabrication parameters of SIS junctions for mixer applications.

3.2.1 Optimum $\omega R_N C_J$ Product

In an SIS mixer, the nonlinear effect of the quasiparticle tunneling current is used in the mixing process. The inherent junction capacitance, being in parallel with the intrinsic junction, tends to short-circuit the desired junction nonlinearity and thus to prevent the full signal power from being coupled into it. It is possible in principle to tune out the junction capacitance at the signal frequency, thereby avoiding this power loss. The junction's $\omega R_N C_J$ product*, which is the

* Actually, the mixer input resistance R_{in}, not R_N, should be used here. But since they are comparable in most cases (at least of the same order), R_N is used instead of R_{in} in most of the literature.

ratio of the junction's normal state resistance to its capacitive reactance, is commonly used to measure the effect of the junction capacitance on the RF power coupling.

Although the optimum value of $\omega R_N C_J$ is still an open question, previous published experiments have shown that small values, i.e. $\omega R_N C_J \approx 1$, tend to give poor mixer conversion [14,15], whereas good mixer performances were obtained with $\omega R_N C_J \sim 10$ [33,61]. It has also been argued that $\omega R_N C_J \geqq 4$ is required for mixer's conversion to reach the values predicted by Tucker's theory assuming the three-frequency approximation [53]. Thus we chose $\omega R_N C_J = 6$ in designing the Princeton - NBS junction used in this experiment. This value should permit operation close to the three-frequency condition, while not being too difficult to tune out.

3.2.2 Normal State Resistance

In order to achieve optimum mixer performance, the junction's resistance should be chosen for reasonable input and output impedance matchings. Previous experiments and theoretical analysis have shown that the input resistance R_{in} and the output resistance R_{out} of an

optimized mixer are comparable to its normal state resistance. Since the output of the mixer is usually coupled to a 50 ohms IF amplifier and the guide impedance of the quarter hight WR-10 waveguide used in our experiment is about 111 ohms, therefore, the desired junction normal state resistance is chosen to fall in the range from 50 to 100 ohms.

3.2.3 Junction Capacitance

With the given $\omega R_N C_J$ product and junction normal state resistance, the desired junction capacitance at the operating frequency can then be determined. This capacitance must be resonanted out at the signal frequency for efficient RF coupling. In principle, this can always be achieved by using an external tuning circuit since this is a constant capacitance and the RF resistance in the superconducting electrodes is very small. By choosing $\omega R_N C_J = 6$, the desired junction capacitance at 115 GHz is:

$$C_J = \frac{6}{2\pi \times 115 \times 10^9 R_N}$$

$$= 83 \text{ fF} \qquad \text{with } R_N = 100 \text{ ohms}$$

$$= 166 \text{ fF} \qquad \text{with } R_N = 50 \text{ ohms} \tag{3.1}$$

3.2.4 Junction Area

For a tunnel junction with barrier thickness d and relative dielectric constant ε, the specific capacitance is simply given by the parallel plate capacitance formula:

$$C_S = \frac{\varepsilon_0 \times \varepsilon}{d} \tag{3.2}$$

However, since the thickness, composition and structure of the oxide barrier are difficult to characterize, experimental data are used to determine the junction area. According to Magerlein [37], the specific capacitance for the Pb-In-Au/oxide/Pb-Bi tunnel junction fabricated by standard IBM process is:

$$1/C_S = 0.35 \pm 0.040 - (0.016 \pm 0.006) \times \ln(j) \tag{3.3}$$

for junctions on the films containing 13.6 at% indium. Here C_S is in $\mu F/cm^2$ and j is in A/cm^2. For critical current densities between 500 and 1500 A/cm^2, C_S is approximately equal to 4.2 $\mu F/cm^2$. The desired junction area is then given by:

$$A = \frac{C_J}{C_S} \tag{3.4}$$

3.2.5 Critical Current Density

Theoretically, for a given normal state tunnel resistance R_N, the maximum dc Josephson current can be obtained from Ambegaokar - Baratoff relation [1]:

$$I_C = \frac{\pi}{2} \frac{\Delta(T)}{e} \frac{1}{R_N} \tanh \frac{\Delta(T)}{2kT} \tag{3.5}$$

Where $\Delta(T)$ is the superconducting energy gap at temperature T. This yields $I_C = 2.15\ mV/R_N$ for lead alloy junction with $\Delta(T)/e = 1.42$ mV and T = 4.2 K. In

practice, the experimental value is $I_C = 1.6\ mV/R_N$ for NBS process. Therefore, the desired junction current density is given by:

$$j_C = \frac{1.6 \times 10^{-3}}{R_N \times A} \tag{3.6}$$

Here area A is in cm^2, R_N is in ohm and j_C is in A/cm^2.

3.2.6 Series Array

As discussed in section 2.7, the performance of an N-junction array is the same as that of a single junction provided that both have the same $\omega R_N C_J$ product. From equations (3.4) and (3.5), it can be shown that $\omega R_N C_J$ is independent of the area of the junction and depends only on the maximum dc Josephson current density. Therefore, except for the junction area, the parameters obtained in previous sections can be adopted in designing an N-junction array. The area of the individual junction must be scaled by a factor of N. Table 3-1 summarizes the design parameters for the arrays used in this experiment.

Table 3-1. Summary of the design parameters of the Princeton - NBS lead alloy junctions.

PARAMETERS	UNIT	A	B	C	D
NO. OF JUNCTION	----	2	2	4	4
$\omega R_N C_J$ PRODUCT (115GHz)	----	6	6	6	6
CURRENT DENSITY	A/cm^2	800	800	800	800
ARRAY RESISTANCE	ohm	50	100	50	100
ARRAY CAPACITANCE	fF	166	83	166	83
AREA OF INDIVIDUAL JUNCTION	μm^2	8	4	16	8

3.3 Junction Fabrication

Junctions fabricated by different laboratories using similar processes were tested in this experiment. The 14-element series-connected arrays of lead alloy tunnel junctions supplied by IBM were fabricated on the 0.010" × 0.005" × 0.010" thick silicon chips by the standard IBM photolithographic process [28]. In this section, we describe the similar process used at the National Bureau of Standards in Boulder where junctions were fabricated to our design by P. Timbie of the Physics Department, Princeton University.

3.3.1 Princeton - NBS Junctions

The Pb-In(12 wt%)-Au(4 wt%)/oxide/Pb-Bi(29 wt%) tunnel junctions were made on 0.010" thick 2" diameter fused quartz wafer (Mark Optics, type GE 124). The superconducting Pb-alloy layers and the insulating SiO films were vacuum-deposited on the quartz wafer and patterned using optical lithography and the photoresist stencial lift-off method. Tunnel barriers are formed on the base electrode films by thermal and sputter oxidation. A wafer contains thirty-six 0.246" × 0.246" chips. Each chip is identical in design and contains 4 different types of arrays (N = 1, 2, 4, 8) on it. Fig. 3-1 shows a 0.010" × 0.005" 2-junction array.

The base electrode is formed by sequentially depositing films of Pb (1000 Å), Au (45 Å), Pb (600 Å) and In (350 Å) on the quartz wafer. It is then covered with a 3000 Å thick SiO insulation layer. Prior to the SiO deposition, a photoresist stencil was prepared over the base electrode. The junction windows are opened in the SiO by the lift-off process to define the junction. The oxide barrier was formed on the base electrode by sputter-etching in an RF-oxygen plasma ($P \sim 16.7\ \mu$). After the tunnel barrier was formed, a 4250 Å thick Pb-Bi(29 wt%) counter electrode and a 1000 Å SiO protection layer were deposited. An additional 1 μm thick SiO protection layer was put down to cover the whole of each device except for the bonding pads. Finally, the entire wafer was covered by 1 μm thick photoresist, for protection, and the fabrication process is completed.

All the single-junctions we obtained were short circuited, probably due to the indium contamination of the Pb-Bi electrode during the fabrication process. None of the 8-junction arrays has been tested due to the wrong spacing between the two bonding pads. Therefore only 2- and 4-junction arrays have been tested. In general, most of the 2- and 4-junction devices show very similar I-V characteristic. However, arrays with an anomalous junction, which has a totally different critical current density from the rest of the junctions in the same array, are found in some

chips. The RF performance of these anomalous arrays is in general inferior to that of the normal ones, there is no attempt in this work to look into this problem.

3.4 Junction Storage

It has been reported that the best storage condition for the lead alloy junctions is to keep them in liquid nitrogen [5]. However, this is impractical for our application. In our laboratory, the junctions are stored in a dry nitrogen atmosphere at a temperature of 0 C. Chips covered by photoresist have remained essentially unchanged for more than two years. Two arrays with photoresist removed did fail, and exhibited an S-I-N type I-V characteristic after 6 months from the initial cool down to liquid helium temperature. But in general, the junctions' thermal recyclability is good. In particular, one 2-junction array has been cycled more than 15 times between room temperature and liquid helium temperature over a period of 14 months with no discernible change in behavior.

CHAPTER 4. MIXER BLOCK DESIGN AND CHARACTERIZATION

4.1 Introduction

As we have seen in chapter 2, the performance of an SIS mixer is completely determined by the junction's dc I-V characteristic, input LO power, bias voltage, and embedding admittance seen by the junction at the local oscillator and all relevant harmonics and sideband frequencies. This embedding admittance is mainly governed by the waveguide and microstrip circuits immediately surrounding the junction, i.e. the "mixer block". Thus, one of the main tasks in developing a high frequency SIS mixer with good performance is to design an external microwave tuning circuit (mixer block) which can provide the junction with the optimum embedding admittance.

In this chapter, we describe the mixers used in this work. Techniques used to characterize the mixer mount will be described, and a microwave equivalent circuit will be derived which includes the effects of conductor loss.

4.2 Mixer Block Design and Construction

Two different blocks were used in this work. The first design, Type J-J, was used in peliminary tests to verify Tucker's theory. The second one, Type-D, which has greater tunability was used in subsequent experiments to achieve better mixer performance.

4.2.1 Type J-J Mixer

This mixer mount, described by Y. Taur and A.R. Kerr [66], was originally designed for point-contact Josephson junction mixers. The mount, shown in Fig. 4-1(a), consists of two major parts, the waveguide transformer and the main body. The transformer reduces the full height WR-10 waveguide (0.100" × 0.050") to quarter height (0.100" × 0.0125") in a series of quarter-wave steps. It is electroformed copper. The main body of the mixer is a brass block split along the wide wall of the waveguide with a 0.019" wide × 0.017" deep slot which contains a suspended quarts substrate. Metal choke patterns are fabricated on the quartz substrate by photolithographic techniques. The metallization is 2.5 μm thick gold over a thin (80 Å) chromium layer for better adhesion.

As shown in Fig. 4-1(b), there are two separate metalized patterns on the substrate, the upper (lower) one consists of 5 (3) quarter wavelength stripline sections of, alternately, high and low characteristic impedance, and an arrowhead-shaped section. These RF choke patterns are designed using large scale models as described later in this chapter: the arrowhead-shaped elements are trimmed on the scale model until a proper reactive impedance for optimum coupling to the junction is measured. This final shape is used in the actual mixer.

Two 0.100" long, 0.001"-diameter gold wires are soldered on the upper end of the substrate before the assembly for later connection to the dc/IF connector. The SIS chip, described in section 3.3, is mounted on the substrate by cold welding with indium. The assembled chip-substrate unit is then transferred into the mixer mount. As shown in Fig. 4-1(c), it lies sideways in the substrate slot of the block and is centered in the slot by a spring-loaded clamping wire. The same spring wire also presses the lower part of the substrate against an indium coated shoulder in the block, to provide dc and IF return paths, and an RF ground. An adjustable contacting type backshort behind the chip is used as the sole tuning element.

4.2.2 Type-D Mount

Figure 4-2 is schematic drawing of the type-D mixer. The gold plated brass mixer block consists of two parallel quarter height WR-10 waveguides. It is fabricated in two halves with the main and side-arm waveguides split along the center of their broad walls. Since at 110 - 118 GHz we are operating somewhat beyond the high end of the normal operating band of WR-10 waveguide (75 - 110 GHz), the actual width of the waveguide was reduced from 100 mils to 96 mils to prevent unwanted excitation of higher waveguide modes. As shown in Fig. 4-2(a), transistions between the main waveguide and the input full height waveguide are accomplished by a broad-band channel waveguide transformer [59]. A 0.020" × 0.010" substrate channel supports a suspended substrate stripline circuit between the two waveguides. The substrate, shown in Fig. 4-2(b), is 0.023" wide × 0.003" thick fused quartz, metalized with stripline circuit patterns which consist of an RF choke structure and a 0.059" long stripline of 50 ohm characteristic impedance. The RF choke is a 7 element quarter-wave design which is used to pass the IF and dc bias to the junction while preventing RF power leakage. The side-arm waveguide is coupled to the SIS chip in the main waveguide through the 50-ohm stripline, thereby

providing a tunable reactance in series with the chip. Two contacting finger type moveable short circuits, shown in Fig. 4-2(a), are used as tuning elements. The side-arm waveguide is blocked by a fixed indium short circuit a quarter wavelength away from the substrate channel; this reflects an open circuit at the stripline-waveguide transistion. The lower half block has 5 mil surface relief over the shaded area, shown in figure 4-2(a), to ensure a good contact along the joint line and reduce loss due to leakage. Gold wires, 0.005" in diameter, are placed in the gasket groves around the SIS chip area to prevent microwave power leakage through the interface. Compared with the conventional mixer design with only one tuning element, this design has much greater tunability at a given frequency, but the tuning is very frequency dependent.

4.2.3 Mixer Assembly

The mixer assembly is quite simple. Referring to Fig. 4-2(a), the two 0.100" long 1 mil diameter gold wires are first soldered to the substrate on the choke pattern end, a 0.030" × 0.009" × 0.001" gold grounding tab is then bonded on the other end of the substrate. Two tiny pieces

of indium are melted onto the middle of the substrate where the SIS chip is to be bonded and then scraped with a blade to expose a fresh, level surface. The SIS chip, 10 × 5 × 10 mil thick, is then cold welded to the indium pads on the substrate using a pressure mounting jig. The complete chip-substrate assembly is transferred into the mixer mount. The substrate is located such that the SIS chip sits in the main waveguide while the lower end of the substrate extends across the side-arm waveguide with the grounding tab resting on the split surface of the block. The two gold connecting wires are then attached into the indium coated center pin of the SMA connector for junction dc bias and IF output. The upper half block is then bolted in place. When the block is assembled, the grounding pad on the substrate is squashed into a 0.020" × 0.005" × 0.004"-deep slot in the upper half of the block. This slot is filled with indium and covered with a 1 mil gold foil to ensure a rigid support for the substrate and a good electric ground contact. Finally, the backshorts are slipped into the waveguides and the mixer is ready for use.

4.3 Mixer Mount Characterization - Scale Model Measurements

4.3.1 Introduction

Due to the complexity of the mixer geometry, theoretical characterization of the mixer would be extremely difficult. Direct impedance measurements are very hard to perform accurately above about 10 GHz. Since the physical dimensions of the mixer mount can be scaled inversely with frequency without appreciably affecting its electric properties (except for the conduction loss), it is much easier to characterize the mixer mount by using a large-scale model at a frequency much lower than the normal operating frequency. The loss in the mount, which is due to the skin effect in the conductors, can either be modeled by choosing the appropriate construction material for the scaled mount or by theoretical estimation. Scale modeling is a valuable technique commonly used in designing millimeter-wave components. See references [25] and [58].

4.3.2 The 40X Scale Model

Two aluminum mixer models were made, one for the type J-J mount, and the other for the type-D mount. In this section, we shall thoroughly discuss the characterization of the type-D mount. Since the same technique is used to characterize the type J-J block, we shall just present, i Fig. 4-17, the measurement results on type J-J model without going into the details.

For the mixer model, a scaling factor of 40 was chosen so that the operating frequency scales from 116 - 112 GHz to 2.9 - 2.8 GHz. Since the junction's capacitance is large enough ($\omega R_N C \sim 7$ to 10) effectively to short circuit all the higher harmonics, only the embedding admittance in the fundamental frequency band needs to be measured. A cross-section of the scale model is shown in Fig. 4-3. The substrate is made of stycast* which has the same dielectric constant ($\varepsilon_r = 3.8$) as fused quartz. Copper adhesive tape** on the substrate surface was cut to form the required circuit pattern. As shown in figure 4-3, a 50 ohm 0.085" diameter coaxial cable is buried within the stycast substrate in contact with the copper tape, with one end connected to the network

---

* Emerson & Cuming Inc. Canton. MA., Stycast Hik.
** 3-M Co. St. Paul, MINN. Electrical tape No. 1245.

analyzer. The other end is at the position of the SIS chip in the real mixer, and hence enables us to measure the embedding admittance normally seen by the junction. Some small corrections must be made, as described later.

4.3.3 Measurement Setup

Figure 4-4 is the block diagram of the measurement setup. The test signal generated by the sweep oscillator (HP-8690B) is coupled to the power spliter (HP-1610A), two identical 10 dB attenuators (HP-8492A) and two high-directivity directional couplers (Narda-5293). One directional coupler is connected to the scale model, the other connected to a short circuited reference coaxial cable identical in length to the cable into the model. A Hewlett Packard network analyzer (HP8411A/8410A) compares the reflected signal from the reference cable with the reflected wave from the mixer model and displays the embedding admittance seen by the end of the coaxial probe (corresponding to the SIS chip in the real mixer) directly on the polar display (HP-8414A). The results can also be recorded on a Smith chart by an X-Y recorder (HP-7034A).

4.3.4 Corrections to the Measured Embedding Admittance

Since the coaxial probe does not resemble the SIS junction (which is a planar device) in the chip region, several small corrections have to be made to transform the measured embedding admittance (on the scale model) into the embedding admittance seen by the junction in the actual mixer. This can be accomplished by characterizing the SIS chip and the test probe as follows.

Figure 4-5 is an enlarged view of the SIS chip in the actual mixer and the corresponding region in the mixer model. Since the physical dimensions of the SIS chip in the actual mixer and the test probe in the scale model are much smaller than the guide wavelength, 121.6 mil at 115 GHz and 4.86" on the 40X scale model, they can be characterized by a number of lumped elements between the reference terminal planes A-A', B-B' shown in Figs. 4-5(a) and (b). The test probe can be represented by the inductance of the center conductor L' and the capacitance C' at the end of the coaxial cable, while the SIS chip can be characterized by the capacitance C_p and the equivalent inductances L_I and L_{II} which represent the magnetic energy stored in regions I and II shown in Fig. 4-5(a). Three large scale models were constructed to measure these quantities, they are: 1) a 300X model of the actual SIS chip (similar to Fig. 4-5(a)), 2) a 7.5X model of the test

probe in the 40X scale model (40 × 7.5 = 300) (similar to Fig. 4-5(b)), and 3) the reference model which is similar to the 300X model of the SIS chip except that, as shown in Fig. 4-5(c), the conductors between the terminal surface AA'-BB' are removed.

The capacitance measurements were performed with a Boonton Capacitance bridge at 1 MHz. C_f is the difference in the measured fringing capacitance betwen the 300X model of the SIS chip and the reference model, while C_p is the difference between the 7.5X model of test probe and the reference model.

Figure 4-6 is a block diagram of the setup used to measure the equivalent inductances L_I, L_{II}. A low frequency (10 - 20 MHz) signal generated by the oscillator is transmitted through the 50 ohm system to the power meter. The unknown inductance (i.e. model of the chip) is then connected in shunt with the 50-ohm line. By measuring the change in the transmitted power the unknown inductance can be determined fairly accurately. A detailed description of this method is given in Appendix I.

The measured values of these lumped equivalent circuit elements are summarized in table 4-1. The corrected embedding admittances can be computed from the

circuit illustrated in Fig. 4-7. The procedure can be regarded as de-embedding the end of the coaxial measuring probe (-L', -C'), then re-embedding it (L_I, C_p, L_{II}) in the actual SIS chip geometry.

Table 4-1 Measured Values of the Lumped Elements

	Test Probe		SIS Chip		
	L'(nH)	C_f(pF)	L_I(nH)	L_{II}(nH)	C_p(pF)
300X Model	7.81	0.462	5.44	0.94	0.576
Actual Mixer	0.026	0.00154	0.018	0.0031	0.00192

4.3.5 Available Embedding Admittance: Measured Results

Embedding admittances (junction capacitance excluded) measured on the mixer model at 2.875 GHz (equivalent to 115 GHz in the actual mixer) are plotted as a function of the two backshort positions in Fig. 4-8. The results are shown on a Smith chart (with both conductance and susceptance normalized to 1/(50 ohm)). It is found that except for a small forbidden region (shown on the Smith chart), all the other embedding admittances can be

achieved by varying the two backshort settings.

To obtain the embedding admittance seen by the intrinsic junction, the junction's capacitive susceptance must be added in parallel with the measured embedding admittance. that is:

$$Y'_{emb} = Y_{emb} + j\omega C \tag{4.1}$$

This has the effect of moving each point in the forbidden region clockwise along a constant conductance line. The resultant forbidden region as seen by the intrinsic junction (which excludes the junction capacitance) is illustrated in Fig. 4-9. Therefore, almost any desired embedding admittance can be presented to the intrinsic junction in this mount.

4.4 Theoretical Characterization of the Mixer Mount

4.4.1 Introduction

Although the junction's embedding admittance can be determined from the scale model measurements described in the previous section. This technique does not simulate the loss in the mixer mount and is very time-consuming. It would be very helpful to construct the equivalent circuit of the mixer mount, including loss, and employ it to predict the junction's embedding admittance as a function of the two backshort positions.

4.4.2 Microwave Equivalent Circuit

An approximate microwave equivalent circuit of the type-D mount for the dominant TE_{10} rectangular waveguide mode is illustrated in Fig. 4-10. The transistion between the junction and the single-mode waveguide is represented by a simple T-network. The elements in this network, which represent the electric and magnetic energy stored in the various parts of the mixer mount, are in general complex. By assuming a loss-less network, these elements can be identified as the gap capacitance C and the lead inductances L_1 & L_2 as shown in Fig. 4-11. The junction's

embedding admittance can be calculated if the precise values of these lumped elements are known. The same 40X scale model described in the previous section, with a small modification of the printed circuit on the substrate, can be used to measure these elements. Details of the measurements are described in Appendix II. The measured values of these parameters are summarized in Table 4-2.

Table 4-2 Measured Values of Equivalent Circuit Parameters

L_1(nH)	L_2(nH)	C(fF)
0.111±0.019	0.039±0.017	6.9±1.01

A simplified equivalent circuit with measured lumped elements is shown in Fig. 4-12. The main backshort is represented by the variable shunt susceptance $B_{B/S}$ while the side arm backshort acts as a variable reactance $X_{B/S}$ in series with the junction in the circuit. The backshort impedance is given by :

$$jX_{B/S} = jZ_g \times \tan(2\pi S/\lambda_g), \qquad (4.2)$$

where S is the distance between the backshort and the

junction, λ_g is the guide-wavelength, Z_G is the waveguide impedance of the TE_{10} mode given by:

$$Z_G = (b/a)240\pi/[1-(f/f_c)^2]^{1/2} \qquad (4\text{-}3)$$

Where a and b are the waveguide dimensions and f_c is its cut-off frequency. The SIS junction is represented by its intrinsic junction shunted by junction's capacitance. In Fig. 4-13, we superimpose the forbidden embedding admittance region, derived from the equivalent circuit, on the experimental results measured on this model. The slight difference between the measured and calculated forbidden region is due to the errors in the measured values of L_1, L_2 and C, resulting from the errors in the mechanical tolerances in the model and the errors within the network analyzer. It is clear from this comparison that the equivalent circuit is adequate to represent the real mixer mount.

4.4.3 Loss in the Mixer Mount

The major loss components in the mixer mount are the sliding backshorts, the waveguide, and the 50 ohm suspended stripline which couples main and side-arm waveguides. A movable contacting backshort usually

presents a small resistance between the contacting fingers and the waveguide walls. For instance, a backshort resistance as high as 7.6 ohm (an extreme case) has been reported in a 115 GHz Schottky diode mixer using backshorts similar to those we used in the type-D mount [23]. In order to reduce this loss, special care has been taken during the mixer assembly: mixer mount and backshorts are cleaned thoroughly; the backshort's fingers are adjusted to ensure a good contact with the waveguide walls. The backshort resistance is estimated to be 0.1 ohm in the type-D mount.

The waveguide attenuation due to the normal skin depth effect can be characterized theoretically [10]. At room temperature, the theoretical loss of the gold plated quarter-height WR-10 waveguide is 0.245 dB/inch at 114 GHz. At liquid helium temperature, this attenuation is estimated to be 0.076dB/inch*. However, due to roughness

---

* Since the anomalous skin effect occurs roughly near 130K for gold at 114 GHz [38], the extreme anomalous surface resistance $R^m_{ex} = (\pi^2 f^2 \mu^2/\beta k)^{1/3}$ is employed in this estimate. Here $\beta = 7.2$ is a constant, f is the operating frequency, μ is the permeability and k is the ratio of the dc conductivity to mean free path σ/λ which is approximately equal to 8.4×10^{14} (ohm $m^2)^{-1}$ for gold.

of the surface of the waveguide, the actual loss may be higher than this values.

The major loss components in the 50 ohm stripline include the conductor loss and dielectric loss [30]. The attenuation due to the dielectric loss is about 0.05 dB/inch at 100 GHz for the fused quartz substrate with dielectric constant $\varepsilon_r = 3.8$ and loss tangent $\tan \delta = 0.0001$ [30]. Regarding the conductor loss, computation using the analysis described by Schneider [55] yields a conductor loss of 1.96 dB/inch for room temperature stripline at 114 GHz and 0.65 dB/inch when cooled down to 4 K. Since these are very rough estimates and other losses such as the loss due to roughness of the surface of the substrate channel are not included, the actual loss is certainly much higher than the calculated values. Therefore an estimated total loss of 1.2 dB/inch is adopted for the stripline at 4 K.

4.4.4 Embedding Admittance Calculated from Equivalent Circuit

Given the equivalent circuit of the mixer mount and the loss in the circuit, the embedding admittance seen by the junction at signal, image and pump frequencies can be calculated as a function of the two backshort settings.

This was accomplished by using a network analysis program [34] which computes the following quantities: a) input impedance (admittance), b) input reflection coefficient $|\rho|$ and Arg (ρ), c) input return loss, d) transmission loss. The results are printed out and displayed on the Smith chart directly.

Some of the possible tuning conditions for the short-circuited image case, as simulated by the program, are presented in Fig. 4-14 to 4-16 : the embedding admittance seen by the junction at signal, image and LO frequencies are plotted on the Smith chart with main backshort position as parameter. Also shown is the transmission loss of the circuit at each possible embedding admittance. A transmission loss of 1-3 dB is usually found in the vicinity of the best operating point. As discussed in chapter 6, the optimum theoretical mixer performance is degraded by this loss.

From the simulation, it is found that tuning is very sensitive to the backshort settings; an accuracy better than 0.5 mil in backshort position is required to achieve optimum results.

CHAPTER 5. EXPERIMENTAL SET-UP FOR SIS MIXER MEASUREMENT

5.1 Introduction

In order to evaluate the performance of the SIS mixer, a carefully calibrated microwave cryogenic mixer testing set-up was used in the experiment. Fig. 5-1 is a block diagram of the experimental set-up, which can be divided into five major parts: 1) the RF section 2) mixer test dewar 3) dc measuring system 4) IF measuring system and 5) the computer-controlled instrumentation. In this chapter, we shall describe the experimental apparatus and discuss the calibration of the measuring system.

5.2 The RF Section

The millimeter-wave sources are two Varian VRT-2123A klystrons. One is used as the local oscillator, the other is used as a monochromatic signal source. The local oscillator frequency is set at 113.9 GHz while the signal klystron can be operated either at 115.3 GHz (upper sideband) or 112.5 GHz (lower sideband) so that the mixer performance at different sidebands can be measured separately. Two home-built 3 MHz-bandwidth phase-locked

loop systems, with an effective pull-in range of 200 MHz peak-to-peak [42], are used to stablize the klystrons. A thermocouple type power sensor (Anritsu model MP 82 B1 with ML 83A readout) and a frequency meter (Hitachi model 2277) can be switched into the system to measure the output power of the klystrons and their frequencies. The modulator (Hughes model 45217 H-3000) following the signal klystron functions as a switch to control the signal power during the measurements. The signal and LO power were combined in a high directivity 20 dB directional coupler (Baytron 3N-40/20) which is connected to the signal input waveguide of the helium cooled test dewar. The loss along the signal and LO paths is carefully measured with less than 0.1 dB error (up to the RF input port of the test dewar). Since the Anritsu power sensor has a maximum VSWR OF 1.6 from 90 to 140 GHz and an accuracy of ± 3% at 115.3 GHz, obtained by calibrating against a calorimeter (TRG model 981/982), the overall uncertainity in the measured loss of this section is about 0.25 dB.

5.3 Cryogenic System - the Test Dewar

Mixing experiments were performed in a modified Infrared Model HD-3 dewar, which has a 5" diameter liquid helium cold head surrounded by a 77 K radiation shield. The dewar, which holds 0.8 liter of liquid nitrogen and 1.1 liters of liquid helium, can operate for more than 24 hours when operated at 4.2 K and for about 8 hours when pumped to 2 K. The cold stage (in vacuum), including the mixer itself, a bias-tee and a home-made cold pad ($\sim$ 18 dB), is usually maintained at 2 K by pumping on the liquid helium. The backshort settings can be adjusted from outside the dewar by a micrometer driven vacuum feedthrough unit which is coupled to the backshorts by two 0.125" fiber glass rods. The mixer and dewar temperatures are monitored by two silicon diode temperature sensors (Lakeshore model DT-500 DRC). The intended function of the cold attenuator is four-fold: it reduces the room temperature blackbody radiation; it acts as a cold RF termination for the mixer with a very well defined temperature; and it provides the necessary mechanical support and heat sink for the mixer block.

It is found that the attenuation of this cold attenuator, which is made by inserting a piece of wedge shaped kapton vane, metalized with nichrome, into the

copper waveguide block, varies slightly as a function of time, therefore it is necessary to measure its attenuation periodically. During the periods when these experiments were carried out, its attenuation, measured at liquid helium temperature, was found to be 17.8 ± 0.2 dB. The cold attenuator is connected to the room temperature microwave system via a 2.5" long stainless steel WR-10 waveguide plated on the inside with approximately 25 μ-inch of copper, which is sealed by a room temperature WR-10 waveguide vacuum window. The window consists of a polyetheylene plug, epoxied into a short reduced-size waveguide section. The return loss of the window is greater than 20 dB over a 6 GHz bandwidth. The insertion loss of the entire input waveguide section, measured with the dewar cooled to liquid helium temperature, is 0.35 dB ± 0.05 dB. The overall attenuation of the dewar input waveguide and cold attenuator is 18.15 ± 0.25 dB.

5.4 dc Bias and Measuring System

The SIS junction is dc biased through a liquid helium cooled bias-T which is also used to separate the IF (1.4 GHz) signal from the dc bias. The advantage of the cooled bias-T is that it can properly heat sink all the leads to ensure that the junction reaches the temperature of the mixer block. The IF signal is isolated from the dc circuit by a 20 pF chip capacitor (ATC-175 series). A coil inductor, close to its parallel self-resonance at 1.4 GHz, is used as an RF choke. The return loss of the bias-T is greater than 25 dB between 1 and 2 GHz. The mixer bias voltage is developed across a 50 ohm bias resistor (thin film rod type) in the bias-T by a current source external to the dewar. The dc I-V characteristic of the junction is measured by a conventional 4-lead methods: 2 wires monitoring the junction voltage and the other two measuring the voltage developed accross the 5 ohm current sensing resistor. Two instrumentation amplifiers (INA-101CM) are used for current and voltage amplification. In order to protect the junction against static and transients, all bias and monitoring wires entering the dewar were filtered by 4-element low pass filters (SPRAGUE series 1JX2851). The insertion loss of the filter is 80 dB at 90 KHz with a low frequency roll

off of 25 dB/octave. The bias voltage can be maintained at a preset value by a leveling loop. This is extremely handy when tuning up the mixer.

5.5 IF Measuring System

The IF (1.4 GHz) output of the mixer, passing through the bias-T, was coupled to a room temperature IF radiometer/reflectometer system via two series-connected 50 ohm stainless steel coaxial cables, which were jointed at the 77 K radiation shield to reduce the heat load to the cold stage. The IF test set, similar to that described by Weinreb and Kerr [78], was used to measure the IF output power of the mixer, its IF reflection coefficient and the attenuation of the dewar's IF section. The 1.4 GHz radiometer is calibrated against liquid nitrogen and room temperature matched loads so that the detected power can be read directly in absolute temperature (± 0.5 K). The mixer's IF mismatch is measured by injecting a 1.4 GHz noise signal through the directional coupler towards the output port of the mixer and measuring the power reflected. By comparing the reflected power (corrected for the round-trip loss in the the dewar's IF section) with the injected signal, the magnitude of the reflection coefficient at mixer's output port can be determined.

In order to determine the performance parameters of the SIS mixer (L, T_M and IF-VSWR), it is necessary to know the attenuation of dewar's IF section and its effective

radiation temperature. This can be accomplished by two separate measurements as described below.

Figure 5-2 illustrates the various noise contributions to the measured output noise temperature from the dewar's IF section, which is terminated by a cold 50 ohm load at its mixer port. Assuming that the attenuation of the IF section is α_{IF} and its effective radiation temperature can be characterized by $T_{\alpha 1}$ (towards the mixer port) and $T_{\alpha 2}$ (towards the room temperature end), the output noise temperature is given by:

$$T_1 = T_r \, \alpha_{IF}^2 \, |\Gamma|^2 + T_{\alpha 1} |\Gamma|^2 \, \alpha_{IF} + T_{\alpha 2} + (1 - |\Gamma|^2) \, \alpha_{IF} \, T_B \qquad (5.1)$$

Where T_r is the room temperature, T_B is the bath temperature and Γ is the reflection coefficient between load and the IF cable. The output temperature, with a noise signal $T_{N/S}$ injected into the IF cable, is:

$$T_2 = (T_r + T_{N/S}) \, \alpha_{IF}^2 |\Gamma|^2 + T_{\alpha 1} |\Gamma|^2 \, \alpha_{IF} + T_{\alpha 2} + (1 - |\Gamma|^2) \, \alpha_{IF} \, T_B \qquad (5.2)$$

Replacing the cold load by short circuit and repeating the above measurements, we have (without the noise injection):

$$T_3 = T_r \ \alpha_{IF}^2 + T_{\alpha 1} \ \alpha_{IF} + T_{\alpha 2} \tag{5.3}$$

and with the noise injection:

$$T_4 = (T_r + T_{N/S}) \ \alpha_{IF}^2 + T_{\alpha 1} \ \alpha_{IF} + T_{\alpha 2} \tag{5.4}$$

From equations (5.3) and (5.4), the attenuation α_{IF} is given by:

$$\alpha_{IF} = \sqrt{(T_4 - T_3) \ / \ T_{N/S}} \tag{5.5}$$

solving (5.1), (5.2) and (5.5) for $|r|^2$, we have:

$$|r|^2 = (T_2 - T_1) \ / \ (T_4 - T_3) \tag{5.6}$$

knowing α_{IF} and $|r|^2$, the effective radiation

temperatures, $T_{\alpha 1}$, and $T_{\alpha 2}$ can be calculated from the following equations:

$$T_{\alpha 2} = [T_2 - T_4 |\Gamma|^2 - T_B \, \alpha_{IF} \, (1 - |\Gamma|^2)] \; / \; (1 - |\Gamma|^2) \qquad (5.7)$$

and

$$T_{\alpha 1} = (T_3 - T_r \, \alpha_{IF}^2 - T_{\alpha 2}) \; / \; \alpha_{IF} \qquad (5.8)$$

With the mixer in place, similar measurements can be performed by biasing the junction at high impedance region and 50 ohm point respectively, also including the shot noise generated by the junction as an additional noise source (discussed in chapter 7). The measured results are $\alpha_{IF} = 0.8 \pm 0.05$ dB, $T_{\alpha 1} = 17 \pm 5$ K and $T_{\alpha 2} = 20 \pm 5$ K.

5.6 Computer Instrumentation

An Apple II plus (48 K) computer was integrated into the system to enable experimental data acquisition and analysis to be performed automatically. Whenever a good operating point was located (the tuning technique will be described in the next chapter), the mixer performance was measured as a function of junction's bias voltage, which can be controlled by the computer through a digitally programmable 12-bit D/A converter (Tecmar, Apple DA101). A home-built 2-channel Apple relay driver was used to control the RF signal source (via the modulator) and the IF noise during the measurements. The output of the radiometer is recorded by the computer via a 14-bit A/D converter (Tecmar, Apple AD211) and stored on diskette for use in the mixer performance analysis. Final results can be obtained from the printer.

CHAPTER 6. THE MIXING EXPERIMENTS AND RESULTS

6.1 Introduction

Functionally, a mixer is characterized by its signal and image conversion loss, equivalent input mixer noise temperature, and output impedance at the intermediate frequency. We have seen in chapter 2 that Tucker's quantum mixer theory can predict the performance of an SIS mixer. In this chapter we discuss how the performance of our SIS mixer, described in chpaters 3 and 4, is measured, and present the experimental results. We also compare the measured results with the predicted performance for our particular junction, using the 3-frequency quantum mixer theory. As shown in this chapter, the agreement between the experimental and theoretical results is very good.

6.2 Experimental Procedure

The SIS mixer block was mounted on a copper heatsink plate which is attached to dewar's cold head. The dewar case was first evacuated to a pressure of about 10 micron Hg and then precooled by liquid nitrogen to reduce the consumption of helium during the final cool-down. The

dewar was then cooled down to 4.2 K by transfering liquid helium. Usually the experiments are conducted at 2 K which is achieved by reducing the helium vapor pressure with a mechanical pump (Welch DUO-SEAL Model 1376). During the experiment, an external Helmholtz coil is used to generate a static magnetic field ($\sim$ 50 gauss) to suppress the Josephson critical current to its first minimum. Optimizing the mixer performance at a given sideband, upper or lower, is quite straightforward. As pointed out by Rudner et al. [53], the mixer noise temperature at most of the operating points is very low, so it is only necessary to minimize the mixer conversion loss and avoid operating in unstable regions when tuning the mixer. Therefore, the dc bias voltage, input pump power and the backshort settings are all optimized to give the maximum readout of the IF radiometer when a signal is applied to the input. Since our IF frequency (1.4 GHz) is rather high and the mixer tuning is very frequency dependent, it is necessary to measure the mixer performance at both sidebands under the same operating conditions. The measurement method is as follows.

The IF mismatch is measured, as described in section 5.5, by injecting approximately 1000 K of noise* towards the mixer IF port and measuring the power reflected. Correction is made for the loss of dewar's IF section. By measuring the IF temperature increment when a known RF signal power is applied to the mixer, the conversion loss can be calculated. The available conversion loss is obtained after correcting for the IF mismatch. The mixer noise can be calculated from the above measurements. Detailed calculations are given below.

Fig. 6-1 shows the various contributions to the noise power measured by the 1.4 GHz IF radiometer at dewar's output port with A) no RF or IF noise power applied to the mixer B) a known RF power, T_{sig} or T_{image}, applied to dewar's RF input port and C) an IF noise power $T_{N/S}$ applied to dewar's IF port. Referring to this figure, the measured noise temperature, T_{IF_A}, T_{IF_B} and T_{IF_C}, in each case is then given by:

$$T_{IF_A} = \{[\alpha_{RF}T_r + (1 - \alpha_{RF})T_B](1/L_s + 1/L_i) + T_M/L_s\}$$

* All the noise powers mentioned in here are expressed in terms of the equivalent noise temperatures, $T = P/k\Delta\nu$.

$$\times [(1 - |\Gamma|^2)\alpha_{IF}]$$

$$+ \alpha_{IF}|\Gamma|^2[T_{\alpha 1} + \alpha_{IF}T_r] + T_{\alpha 2} \qquad (6.1)$$

$$T_{IF_B} = T_{IF_A} + T_{sig}\ \alpha_{RF}(1 / L_s)\alpha_{IF}(1 - |\Gamma|^2)$$

or (6.2)

$$T_{IF_B} = T_{IF_A} + T_{image}\ \alpha_{RF}(1 / L_i)\alpha_{IF}(1 - |\Gamma|^2)$$

and

$$T_{IF_C} = T_{IF_A} + T_{N/S}\ \alpha_{IF}{}^2|\Gamma|^2 \qquad (6.3)$$

where

α_{RF} = the attenuation of dewar's RF section

T_r = room temperature

T_B = bath temperature

Γ = reflection coefficient at mixer IF port

L_s = conversion loss at signal frequency

L_i = conversion loss at image frequency

T_M = equivalent single sideband noise temperature of the mixer referred to the input port.

α_{IF}, $T_{\alpha 1}$, and $T_{\alpha 2}$ are defined in section 5.5 as the dewar's IF attenuation and it's effective radiation temperatures, respectively.

Solving (6.1) and (6.3) for $|r|^2$, we have:

$$|r|^2 = [1 / \alpha_{IF}^2][(T_{IF_C} - T_{IF_A}) / T_{N/S}] \qquad (6.4)$$

From equations (6.1) and (6.2) the conversion loss at signal (image) frequency L_s (L_i) is given by:

$$L_{s(i)} = [\alpha_{RF}\alpha_{IF} / (T_{IF_B} - T_{IF_A})] \times (1 - |r|^2)\, T_{sig(image)} \qquad (6.5)$$

Knowing L_s, L_i and $|r|^2$, the single sideband mixer noise temperature T_M can be calculated from (6.1) as:

$$T_M = [T_{IF_A} - T_{\alpha 2} - \alpha_{IF}|r|^2(T_{\alpha 1} + \alpha_{IF}T_r)]L_s / [\alpha_{IF}(1 - |r|^2)] - [\alpha_{RF}T_r + (1 - \alpha_{RF})T_B][1 + (L_s / L_i)] \qquad (6.6)$$

6.3 Experimental Results

The mixing performances of various SIS arrays, fabricated by IBM and NBS-Boulder, have been tested at 115 GHz, and are summarized in table 6-1. These results are discussed in detail below.

6.3.1 The Type J-J Mixer

Figures 6-2 and 6-3 show the typical experimental results for the type J-J mixer with the IBM 14-junction array. The dc I-V curve with or without LO power (P_{LO}) and the measured output noise temperatures T_{IF_A}, T_{IF_B} and T_{IF_C}, which are described in the previous section, are plotted on the same dc bias voltage scale. Being operated at 2 K, the unpumped dc I-V curve shows a very sharp rise at the energy-gap voltage, $V_g = 14(2\Delta/e) \approx 41.5$ mV, and a barely noticeable subgap structure at about 23 mV. Measured at the center of the first photon step, $V = V_g - 14(\hbar\omega/2e) = 38$ mV, the leakage current is around 5 μA. The normal state resistance of array is rather high, R_N = 600 ohm measured at V = 55 mV. Since the array capacitance is 22.5 ± 2.0 fF, this yields an $\omega R_N C$ product of 10 for the entire array at 115 GHz.

With LO power applied, the pumped dc I-V curve exhibits the photon-assisted tunneling structure with a voltage step of 14 $\hbar\omega/e$. Similar voltage-modulated structures are also observed in the three measured output noise temperature curves and therefore in the mixer performance parameters (L_C, T_M and IF-VSWR). The best conversion is obtained when junction is biased at the first peak below the gap voltage. This agrees with the general trends observed by Rudner et al. [53] that for large R_N the conversion is more efficient at the first peak while for low R_N the high number peak (low bias voltage) is more efficient.

As shown in Fig. 6-4, under certain tuning conditions negative differential resistance is observed at the first photon peak. This implies that, for low IF, infinite conversion gain is available into an appropriate IF load. This has been verified by the dc incremental method [70]. The mixer's IF reflection coefficient, calculated from the T_{IF_C}-V curve, is also found slightly greater than unity at V = 38 mV. Therefore, the mixer's IF output resistance is negative and the infinite gain is also available at 1.4 GHz. Since the array normal state resistance is extremely high, the mixer is very badly matched into the 50 ohm load. Therefore the maximum realized conversion in these experiments, from mixer input to the 50 ohm load, is about

11.5 dB. This is achieved by biasing the junction at the center of the first photon step. By installing a high ratio IF transformer or by terminating mixer with an appropriate high resistance load, substantial conversion gain could be realized in this mixer. At the same bias point, the equivalent single-sideband mixer noise temperature is 70 ± 40 K. High noise due to the Josephson effect, which is sensitive to the applied magnetic field, was observed for bias voltages below 28 mV. At higher voltages, the mixer performance is independent of the applied magnetic field. The saturation power measured at the 1-dB gain compression point is about 30 nW.

6.3.2 The Type-D Mixer

Several NBS N-junction series arrays, (N = 2, 4), were tested in the type-D mount. Some typical results are presented in Figures 6-5 and 6-6. The general features of the unpumped dc I-V characteristics of these arrays, such as the steep current raise at the gap voltage, $V_g = N(2\Delta/e)$, low leakage current and sharp corner below the gap voltage, are very similar to that of the IBM array. The normal state resistances of these arrays are between 50 and 100 ohm. Using an estimated array capacitance of 0.1 pF gives $\omega R_N C = 4$ to 7. The pumped dc I-V curves show

very clear photon steps with voltage periodicity of $N\hbar\omega/e$. By adjusting the backshort settings and the input LO power, it is possible to obtain a negative differential resistance region on the pumped dc I-V curve at the first photon step. Measured under the same tuning conditions, an IF-VSWR about 1.8 is obtained. The significant difference between dc and 1.4 GHz IF output impedance is due to the sharp RF tuning of the mixer.

Since this mixer mount has very broad tuning range, the mixer can be tuned for operation with almost any desired sideband ratio. The performance of the two-junction arrays is generally superior to that of the 4-junction ones. The best result obtained, with the mixer tuned for single-sideband operation (lower-sideband rejection > 25 dB) and biased at the first photon step, is a conversion loss of 6.9 ± 0.5 dB at 115.3 GHz and the mixer noise temperature of 20 K*. The mixer's instantaneous bandwidth is 350 MHz, and the 1-dB gain compression point occurred at ∿ 4 nW.

This SIS mixer, whose performance is superior to any yet reported at 115 GHz, has been used to construct an

---

* As shown in the next chapter, the mixer noise temperature deduced from receiver's performance is 15 ± 14 K.

ultra-sensitive 110 - 115 GHz receiver. The construction and performance of this receiver will be described in chapter 7.

6.4 Comparison: Experimental Results Versus Theoretical Predictions

Dr. M. J. Feldman has calculated the performance of our mixers by applying the three-frequency quantum mixer theory to the measured unpumped dc I-V curve of the array under the following assumptions: a) All of the junctions in the array are identical. Then the array can be treated as an "equivalent single junction". b) The junction capacitance is large enough to short circuit all of the higher harmonics. c) The dc current through the array is entirely due to the single particle tunneling. His results are used to compare with our experimental data.

6.4.1 Quantitative Verification of Tucker's Theory [18]

We have carried out a series of measurements on the type J-J mixer (with the IBM 14-junction array) at 115 GHz. The results are found to be in good agreement with the theoretical predictions. In these experiments, the mixer performance was measured, with the same applied LO power ($\sim$ 180 nW), at each of nine equally-spaced backshort settings (every 5 mils). Figure 6-7 illustrates one of these results obtained with the backshort set to 0.248". In order to compare with the theoretical predictions, four

data points, as shown in Fig. 6-7, were chosen from each of the nine backshort settings at the first and the second photon steps. They are the conversion losses and the pumped dc currents at the bias voltage of 38 mV (= $V_g - N\hbar\omega/2e$) and 31 mV (= $V_g - 3N\hbar\omega/2e$). These 36 experimental data points, displayed in Fig. 6-8 as a function of backshort settings, are used to compare with the theoretical calculations.

Since the measured result of our mixer noise temperature, $T_M = 70 \pm 40$ K, is not precise enough for quantitative comparison, no attempt was made to compare the mixer noise temperature.

In order to simulate the experimental situation, Feldman used the following experimental information in his calculation: a) the experimentally measured incident LO power, $P_{LO} = 180 \pm 40$ nW, b) the IF load resistance is 50 ohm, c) the array capacitance, $C = 22.5 \pm 2$ fF, and d) the complex embedding admittance at each backshort setting, for signal, pumped and image frequencies, measured on the scale model and shown in Fig. 4-17.

One of the calculated results, with $P_{LO} = 173$ nW and $C = 22.5$ fF (both within the experimental errors), are shown in Fig. 6-8. The computed conversion losses and the pumped dc currents at 38 mV and 31 mV are displayed as a

function of backshort setting for comparison. The agreement between the theoretical results and the experimental data points is extremely good. This quantitatively verifies Tucker's three-frequency quantum mixer theory, at least for an SIS mixer with $\omega R_N C$ product about 10. This is the most convincing quantitative verification of Tucker's theory which has yet been published.

It is found that good agreement between theory and experiment exists if the theoretical calculations assume P_{LO} between 163 nW and 180 nW, and C between 22 fF and 23 fF. The measured values of P_{LO} and C are 180 ± 40 nW and 22.5 ± 2.0 fF respectively. It is clear that, by fitting the predictions of quantum mixer theory to the experimental mixer measurements, the capacitance of an SIS junction can be determined more precisely than by other techniques [2,37,82].

We also compared our measurements with theoretical calculations which assumed equal terminations for signal and image frequencies. The observed huge discrepancies between the theoretical and the experimental results indicate that the embedding admittance at each RF frequency has a very significant effect on the mixer performance. Therefore, one should determine these quantities as accurately as possible.

In order to determine the effects of the nonlinear quantum reactance, the same data set was compared with calculations neglecting the nonlinear quantum reactance terms in eq. (2.58). The computed results still agree very well with the experimental ones. Thus, we conclude that the nonlinear quantum reactance has no detectable effect on our results.

6.4.2 Analysis of the Type-D Mixer

The theoretical performance of the type-D mixer, whose unpumped dc I-V curve shown in Fig. 6-5, was calculated by Feldman. For equal signal and image terminations, he predicted a best conversion loss of 1.5 dB. But in our experiments, due to the sharp tuning of the mixer mount, only one sideband could be well terminated while the other was approximately short-circuited (see Figs. 4-14 to 4-16). Thus, we should compare our results with the predictions assuming shorted image case. Fig. 6-9 shows contours of the predicted conversion loss, assuming the image is short-circuited, as a function of the normalized signal source conductance and susceptance plotted on the Smith chart. These contours were calculated by assuming an IF load resistance of 50 ohm and that the junction is biased at the first photon

step below the gap-voltage. Furthermore, at each of the signal source admittances, the junction bias voltage and the normalized pumped voltage α [$= eV_{LO}/(2\hbar\omega)$] are optimized for the best conversion. The optimum α is found between 1.2 and 1.6. As shown in Fig. 6-9, the best conversion loss, 4.3 dB, occurs at the optimum source admittance $Y_s^{opt} \approx [(0.0165 \pm 0.0002)-j(0.0045 \pm 0.0002)]$ mho. Recalling that, in section 4.4.4, our simulations of the type-D mount embedding admittance have shown that in the vicinity of this optimum source admittance point, the circuit transmission loss will add 1-3 dB to the conversion loss. Hence in the short-circuited image case, the predicted overall conversion loss is 5-8 dB, which is in good agreement with our measured results.

In the vicinity of the best operating point, the predicted mixer output noise temperature is 3.9 ± 0.4 K which corresponds to an equivalent input noise temperature of 19 ± 4 K if the experimental conversion loss, 6.9 ± 0.5 dB, is used in calculation. This agrees very well with the measured mixer noise temperature, $T_M = 20 \pm 15$ K.

As described in section 6.3.2, under certain tuning conditions, we observed a negative differential resistance region on the pumped dc I-V curve at the first photon step in this mixer. This phenomenon is also predicted by the theory. To show this, the predicted values of the local

oscillator termination, which yields negative differential resistance on the pumped dc I-V curve, are mapped on the shaded area of the same Smith chart (Fig. 6-8). Since this shaded area falls within the available embedding admittance region shown in Fig. 4-9, we would expect regions of the negative dc differential resistance to appear on the pumped I-V curve.

Table 6-1 Typical properties of lead alloy SIS array mixers operated at 2 K with f_{sig} = 115.3 GHz, f_{LO} = 113.9 GHz and f_{IF} = 1.4 GHz

TYPE OF ARRAY	AREA OF EACH JUNCTION (μm^2)	j_c (A/cm^2)	R_N (ohm)	$\omega R_N C$	L_C (dB)	I_{RJ} [1] (dB)	T_M (K)	IF-VSWR	P_{LO} (nW)	SATURATION [2] POWER (nW)	BAND- [3] WIDTH (MHz)
IBM 14-JUNCTION	8	700	600	10	11.5±0.5	-0.5	70±40	60	160	30	-
NBS 2-JUNCTION	8.4	600 [4]	63	8.5	8.0±0.5	>12	20±15	1.05	215	7	300
NBS 2-JUNCTION	4.5	760 [4]	94	6.7	6.9±0.5	>25	20±15 15±14 [5]	1.6	250	4	350
NBS 4-JUNCTION	17.2	410 [4]	90	12	9.0±0.5	-	23±15	1.5	3400	-	-

[1] Image regection ratio, measured under the same tuning conditions
[2] Measured at 1 dB gain compression point
[3] 1 dB bandwidth. This was limited by the mixer and not the IF system
[4] Assuming $R_N I_C$ = 1.6 mV, typical for NBS junctions
[5] Deduced from the receiver performance (see next chapter)

CHAPTER 7. A PRACTICAL SIS RECEIVER AT 115 GHz

7.1 Introduction

The previous chapters have explained the design, fabrication, measurement, and optimization of our SIS mixers, and have analyzed their performance. As shown in chapter 6, the agreement between the measured mixer performance and the theoretical predictions is excellent. It appears that the properties of our SIS mixers are well understood. The final part of this thesis is devoted to the development of a low-noise SIS receiver for radioastronomical applications at 115 GHz. In this chpater, we describe the construction of a 110 - 118 GHz ultra low-noise receiver using one of the type-D SIS array mixers which were optimized and described in chapter 6. We also discuss the performance of this receiver, which turns out to be the most sensitive one ever reported for this frequency range.

7.2 Receiver Description

Fig. 7-1 is a simplified block diagram of the SIS receiver front-end. The local oscillator power is provided by a frequency-doubled 57 GHz klystron which is stablized by the same phase-locked loop described in chapter 5. The varactor diode doubler consists of a GaAs Schottky diode, mounted in a parallel WR-10/WR-15 waveguide structure as described by Siegel [58], and can provide roughly 10 mW power at 114 GHz. The design of the receiver dewar is very similar to the test dewar described in chapter 5, the main difference being the use of a liquid helium cooled cross-guide coupler for LO injection and the use of a liquid helium cooled field-effect transistor amplifier [79] as the first IF stage. Fig. 7-2 is a picture of the complete SIS receiver. The dewar is an Infrared Laboratories' model HD-3(8) dewar which holds 2.8 liters of liquid helium and 2.5 liters of liquid nitrogen and can provide approximately 11 hours continuous operation when the liquid helium is pumped down to 2.5 K. The incoming RF signal is collected by a room temperature scalar feed horn which is connected through a 3" long copper-plated stainless steel WR-10 waveguide and a 20 dB cross-guide LO injection coupler to the type-D SIS mixer. The total insertion loss from the aperture of the scalar

feed to the mixer is 0.6 dB and contributes about 12 K to the receiver noise temperature. The local oscillator power is introduced into the dewar via a 10" long stainless steel WR-10 waveguide to reduce the heat load to the liquid helium. Although the overall loss along the LO path is very high, around 30 dB, this scheme still provides enough LO power to operate the SIS mixer. Both of the signal and the LO input waveguides are sealed by the room temperature waveguide vacuum windows described in section 5.3.

The 1.2 - 1.6 GHz IF output from the SIS mixer is coupled through a bias-tee (described in section 5.4) and a 1.4 GHz isolator (Passive Microwave Technology, model 1102) to the L-band GaAs FET amplifier which is then connected to dewar's room temperature IF output port via a 0.085" stainless steel coaxial cable. As shown in Fig. 7-2, all these major components are cooled to 2.5 K. The FET amplifier has about 30 dB gain and an input return loss > 15 dB from 1.2 to 1.7 GHz. The power dissipated from the amplifier is about 75 mW which is approximately half of the total heat load to the liquid helium. Thus any further reduction of amplifier's power dissipation would considerably increase the helium hold time of the dewar.

The insertion loss between the mixer and FET amplifier is 0.3 dB over the 1.2 to 1.6 GHz frequency range which is mainly contributed by the isolator. The noise temperature of the IF amplifier can be measured by using the shot noise generated in the unpumped, dc biased SIS array, as an IF noise source*. Taking into account the mismatch between the mixer's IF output and the IF section, the noise temperature of the IF section is found to be 10.5 ± 1.0 K, referred to the mixer's output port. As described in section 5.5, all the bias and the monitoring wires entering the dewar were carefully isolated and filtered to avoid the RF pick-up and protect the junction against static discharges and transients.

The mixer backshort adjustment assembly, temperature monitoring system and the junction bias and monitoring circuit are the same as those used in the test dewar. Details are given in chapter 5.

The receiver was usually tuned for > 20 dB image rejection, thus operating as a true single sideband receiver. This was measured using a sideband generator

---

* As shown in [19], if an N-junction array is biased with a dc current I_{dc} at a differential resistance R_d, the shot noise power per unit bandwidth is $eI_{dc}R_d/2N$.

which generates equal amounts of power at both the upper and the lower sidebands. The sideband generator consists of a 2.4 to 3.7 GHz varactor tuned transistor oscillator (Avantek, model VTO-8240) and a conventional GaAs Schottky diode mixer [12], which is used as a harmonic generator. The Schottky diode mixer was pumped at 2.812 GHz to generate 40th and 41st harmonics at 112.48 GHz and 115.29 GHz respectively. The output at both sidebands was measured, the harmonic generator tuned so they were found to be within 1-dB difference.

As shown in the previous chapter, the mixer performance depends on four strongly interacting parameters, namely: the dc bias voltage, the incident LO power, and the two backshort settings. Two independent leveling loops, as shown in Fig. 7-1, were used to simplify the mixer tuning process. The first leveling loop maintains the constant dc bias voltage which is usually set at the center of the first photon step below the gap voltage, the other one maintains the constant dc current through the junction (thus the constant pump voltage V_{LO} across the junction through eq. (2.78)) by adjusting the incident LO power via a modulator (Hughes, model 45217H-3000). The receiver performance can be optimized much more easily if these parameters are independently controlled.

7.3 Receiver Performance

The receiver's response to room temperature and liquid nitrogen loads is shown in Fig. 7-3: the receiver's 1.4 GHz output power, in a 50 MHz bandwidth, and junction's dc current with and without the incident LO power ($\sim$ 250 nW) are plotted on the same dc bias voltage scale. At the dc bias voltage of 5.45 mV, the measured single sideband receiver noise temperature, with an image rejection ratio > 25 dB, is 89 ± 3 K* at 115.3 GHz, referred to the aperture of the scalar feed horn. Since the junction was biased at the first photon step, no magnetic field was applied in these measurements. Fig. 7-4 shows the various noise contributions to the overall receiver noise temperature at 115 GHz. Assuming a mixer conversion loss of 6.9 dB, as measured in the test dewar, the mixer noise temperature deduced from Fig. 7-4 is 15 ± 14 K, which is in good agreement with the measured result presented in table 6-1.

The saturation power of the receiver is limited by

* T_R has been improved to 83 K by installing a new SIS 2-junction array and retuning the FET amplifier. The retuned amplifier dissipates less heat and has a lower noise temperature at the expense of a narrower bandwidth.

the SIS mixer whose 1-dB gain compression point occurs at 4 nW input. As shown in Fig. 7-5, the receiver's noise temperature changes less than 10 K within a 270 MHz instantaneous bandwidth.

If we operate the receiver at 4.2 K, the single sideband receiver noise temperature increases to 200 K*. This is mainly due to the higher mixer conversion loss, roughly 4 to 5 dB more, at 4.2 K. Properties of this SIS receiver are summarized in table 7-1.

Fig. 7-6 shows the single sideband receiver noise temperature as a function of signal frequency for an image rejection ratio larger than 20 dB, when it is retuned at each frequency. The SSB receiver noise temperature is about 80 K below 115 GHz and rises at higher frequencies. This increase in the noise is a result of the cross-guide LO injection coupler, which has an evanescent mode at 118 GHz. Better results can be achieved by relaxing the image rejection, for instance, with 12 dB image rejection ratio, a single sideband receiver noise temperature of 68 K was obtained at 112.3 GHz. This receiver has been proved to

---

* At 4.2 K, T_R was improved to 143 K by installing a new SIS array and retuning the FET amplifier.

be very reliable and simple to use. It is presently in use on the Columbia-GISS 4-ft telescope.

Table 7-1 Properties of the SIS receiver at 2.5 K and 4.2 K, with f_{sig} = 115.3 GHz, f_{LO} = 113.9 GHz, and f_{IF} = 1.4 GHz

BATH TEMPERATURE	2.5 K	4.2 K
SSB T_R	89 K [83 K]1)	200 K [143 K]1)
L_C	6.9 dB	---
T_M	15 K	---
BANDWIDTH	270 MHz	---
IMAGE REJECTION RATIO	> 25 dB	> 25 dB
TOTAL HEAT LOAD TO LIQUID HELIUM	156 mW	---
LIQUID HELIUM HOLD TIME	11 hr	---

1) Using the new SIS array and the retuned FET amplifier

CHAPTER 8. OBSERVATIONS OF DISTANT MOLECULAR CLOUDS TOWARD THE CYGNUS-X REGION WITH A 4-FOOT MILLIMETER WAVE TELESCOPE

8.1 Introduction

The SIS receiver described in chapter 7 is now successfully in use on the Columbia-GISS 4-ft telescope. This receiver, which has a single sideband noise temperature of 83 K at 115 GHz, is currently the best in operation at this frequency and is some 25 times more sensitive than its room temperature predecessor. More than 20,000 CO spectra have been obtained in the 1983-84 observation season with the new SIS receiver. The typical integration time per scan is only about 1 minute for an rms noise of 0.25 K with a bandwidth of 250 KHz per filterbank channel. A first order fit is generally sufficient for the baselines.

In order to demonstrate the power of this new receiver, we, in collaboration with Y.-L. Huang, undertook a CO survey toward the Cygnus-X region. Results are presented in this chapter.

8.2 The Columbia-GISS Sky Survey Telescope

The Columbia-GISS 4-ft Sky Survey Telescope is located on the roof of the Pupin Physics Laboratories at Columbia University in New York city. The telescope consists of four major parts: the antenna, the SIS receiver, the spectrometer, and the control system. These will be summarized in this section.

The antenna is a Cassegrain reflector with a half-power beamwidth (FWHM) of 8.7 arc min and a beam efficiency of 0.75 at 115 GHz. It consists of a 4-foot diameter main reflector with f/D = 0.375 and a 7 inch secondary. The effective f/D ratio of the Cassegrain system is 3.79. The feed is a 5-inch long scalar feed horn with an aperture of 1.5 inches. For additional details of the antenna, see R. Cohen [8].

The front-end of the telescope is the liquid-helium cooled SIS receiver (usually operated at 2.5 K by reducing the liquid helium vapor pressure) described in chapter 7. The incoming radiation is collected by the scalar feed horn, downconverted to a 1.4 GHz intermediate frequency (IF) signal by the SIS mixer, and then amplified by the liquid helium cooled FET amplifier. The output from the

SIS receiver is further amplified by a low noise transistor amplifier with 30 dB gain and then down converted again to the second IF of 150 MHz. This second IF is amplified (by approximately 30 dB) and sent to the spectrometer. At 115 GHz, the complete system has a single sideband noise temperature, measured in front of the scalar feed, of 83 K with a 25 dB image rejection ratio.

The spectrometer is a 256-channel filterbank similar to the standard NRAO design [39]. The spectral resolution is 250 KHz, which corresponds to a velocity resolution of 0.65 km s^{-1} at 115 GHz, and a total bandwidth of 166 km s^{-1}.

The output of each channel filter is detected by a square-law detector and then sent to an analog integrator which integrates the data for 48 msec. The outputs of the integrators are then passed to a 12-bit analog-to-digital converter for readout to the computer.

An on-line minicomputer (Data General Nova 1200) is used for telescope guidance, data acquisition and preliminary data processing. Details of the telescope mount and drive system, the back end and the computer system are given in G. Chin [6] and T. Dame [13].

8.3 Observations

All the spectra were obtained by position switching (i.e. by alternately observing the source position and two nearby CO emission-free comparison positions) at roughly 15-second intervals, until the rms channel-to-channel noise was about 0.25 K. Typically, the integration time per scan was 1 minute. The receiver is calibrated against a room-temperature black-body by the chopper-wheel technique, which automatically compensates for changes in the atmospheric attenuation and expresses line intensities in terms of the antenna temperature. Correction for the beam efficiency yields the radiation temperature, T_R, which is related to the radiation intensity, I_ν, by the Rayleigh-Jeans formula: $I_\nu = 2kT_R/\lambda^2$, where k is the Boltzmann constant and λ is the wavelength. The filter bank was centered at -60 km s^{-1} with respect to the Local Standard of Rest (from which the local galactic motion has been removed), and covered a velocity range from -143 km s^{-1} to 23 km s^{-1}.

Our observations of the J = 1→0 rotational transition of CO at 115 GHz toward the Cygnus-X region were made in March 1984. We mapped a square region, roughly 4° on a side, centered at galactic coordinates $\ell = 78.5^o$, $b = 1^o$ (Fig. 8-1). The map consists of 522 spectra and the total

integration time was about 13 hours.

In this region, CO emission lines have been detected over a wide range of velocities, from -80 to 20 km s^{-1}. Only the emission from molecular clouds which lie well beyond the nearby Cygnus Rift, will be discussed here. These clouds have radial velocities more negative than -20 km s^{-1}.

Seven well separated clouds have been identified whose velocities are between -80 and -20 km s^{-1}. In Fig. 8-2, we show a typical spectrum from each cloud. The spectra are remarkably flat so that it was sufficient to remove only a first order baseline from the raw data. Fig. 8-3 shows the spatial maps of the largest cloud. The CO emission is integrated over velocities from -55 to -35 km s^{-1}.

8.4 Discussion

A previous search for CO emission in this direction was performed by H.-I. Cong [11] using a 40-channel filterbank with 1 MHz resolution (corresponding to 2.6 km s^{-1} at 115 GHz). Cong [11] detected no emission with an antenna temperature higher than 1 K between -50 and -25 km s^{-1}. This was probably because spectral dilution smeared the emission.

Approximate distances to the seven clouds discovered in the direction of the Cygnus-X region can be obtained by assuming that the orbits of molecular clouds about the galactic center ar circle. This technique is standard when stellar companions, whose distance could be more accurately determined, cannot be found for interstellar clouds.

For galactocentric radii larger than that of the sun (R_o), a reasonable approximation is that the galaxy's circular rotation velocity is a constant 250 km s^{-1}. Accordingly, the radial velocity of a cloud which lies in the direction of galactic longitude ℓ at galactocentric distance R is:

$$V_r = 250 \sin\ell \, [(R_o/R) - 1] \qquad (8.1)$$

where R_o is the radius of the solar circle. By adopting the canonical value R_o = 10 kpc and observing the cloud's radial velocities, we can solve for their galactocentric distances and then determine their distances from the sun. The kinematic distances of the seven clouds are estimated to be between 6.5 and 12.7 kpc, corresponding to galactocentric radii of 11 to 14.7 kpc.

Cloud masses are estimated from the velocity-integrated CO intensity W(CO) (= $\int T_R dV$). We assume a mean molecular weight per H_2 molecule of 2.72 and an emperical conversion factor 2×10^{20} cm^{-2} K^{-1} km^{-1} s [35] between the molecular hydrogen column density and W(CO). The seven distant clouds are found to have masses between 1 and 6×10^5 $M_\odot$, typical of values found for giant molecular clouds in the inner Galaxy by Dame [13]. Table 8-1 summarizes the physical characteristics of the seven distant clouds.

Evidence for massive star formation, namely the radio HII region DR7 [48], is found only in the largest cloud (No. 5). Heavy foreground obscuration may have hampered the optical detection of young stellar objects near the clouds. Although embedded massive stars might be detected

by their radio recombination-line emission, no systematic search for such emission has been made in the Cygnus-X region.

Giant molecular clouds are concentrated in the galaxy's spiral arms. Because so many large clouds lie within the small longitude range of our map, it is likely that our line of sight is tangent to a spiral arm. As shown in Fig. 8-4, this arm is possibly the extension of the well-known Orion Arm which may merge with the Perseus Arm and the Outer Arm in this direction.

This survey clearly demonstrates the power of our SIS receiver. Compared with the original room temperature Schottky diode receiver, the overall system noise temperature (i.e., the noise contributed from both the receiver and the earth's atmosphere) has been improved by a factor of 5. Therefore, 25 times less integration time is required to produced a spectrum with the same signal to noise ratio. Furthermore, the quality of the spectra is excellent; only linear baseline removal is needed. Since atmospheric variability contributes significantly to baseline instability, the good baselines are at least partly attributable to the short integration time per scan required to obtain adequate signal to noise ratio. This performance clearly makes our receiver one of the most powerful tools currently available for use in

millimeter-wave astronomy and the ease with which optimization can be accomplished makes it very practical receiver. Many time consuming experiments, such as large-scale galactic surveys, will be made feasible or at least will benefit by this receiver's development.

TABLE 8-1. PHYSICAL CHARACTERISTICS OF THE DISTANT MOLECULAR CLOUDS TOWARD THE CYGNUS-X REGION

CLOUD	CENTER OF CLOUD		PEAK VELOCITY ($km\ s^{-1}$)	DISTANCE FROM SUN (kpc) (1)	GALACTOCENTRIC DISTANCE (kpc) (1)	EFFECTIVE RADIUS (pc) (2)	MASS ($10^5 M_\odot$) (3)
	l (°)	b (°)					
1	79.8	0.8	-21	6.5	10.9	66	2.2
2	77.0	0.0	-21	7.2	10.9	53	1.2
3	80.3	1.5	-32	7.6	11.5	64	1.8
4	77.0	0.0	-32	8.4	11.5	87	2.9
5	79.0	1.0	-42	8.9	12.1	116	5.8
6	78.5	1.3	-62	11.1	13.4	83	2.1
7	77.9	0.8	-75	12.7	14.4	85	3.9

Notes: (1) Adopting a "flat" rotation curve with $V = 250\ km\ s^{-1}$ and $R_o = 10$ kpc

(2) $(Area/\pi)^{1/2}$

(3) Adopting $N(H_2)/W(CO) = 2 \times 10^{20}\ cm^{-2}\ K^{-1}\ km^{-1}\ s$

CHAPTER 9. FUTURE WORK, SUMMARY AND CONCLUSION

9.1 Directions for Future Work on SIS Receivers

Although our SIS receiver is almost twice as sensitive as any previously reported, this result is still very far from the ultimate quantum-limited sensitivity predicted for an SIS receiver. The reasons for this are explained in chapters 4 and 6. Several experiments are being planned to overcome the present practical limitations and enable the SIS receiver to approach its theoretical performance. The main directions for future work are:

1) All Superconducting Mixer Circuit.

As indicated in Chapter 4, the backshort contact resistance and the ohmic circuit loss in the mixer mount, which is made of OFHC copper with a chromium-gold suspended stripline circuit, add 1 to 3 dB to the mixer conversion loss. It is hoped that we can reduce this loss by using superconducting circuits. Experiments using a niobium mixer block and niobium suspended stripline circuits are now under way.

2) Inductively Shunted Junction.

With the help of a 500X scale model, we have designed a new SIS chip on which the junction is shunted by an inductive loop designed to tune out the large junction capacitance at the signal frequency. Our computer simulation indicates that this new design will provide better tunability: mixer conversion gain is expected along with a wider bandwidth ($\sim$ 2 GHz).

3) Niobium Tunnel Junction.

Although lead alloy tunnel junctions have proved suitable for our present work, there are several reasons for considering refractory (e.g. niobium, tatalum) tunnel junctions. These junctions have higher electrical and mechanical strength, better thermal recyclability, and better long term stability. They also have higher critical temperature which should allow operation at temperatures achievable by present closed-cycle refrigerators, typically 4 - 6 K.

Several niobium edge-junctions, fabricated by IBM Thomas J. Watson Research Center, have been tested. A double sideband conversion gain of 0.3 dB and a double sideband receiver noise temperature of 50 K have been observed in prilimary measurements. Although the junction

normal state resistance is low ($\sim$ 50 ohm in this case), this result is already comparable with that of the lead junctions. Increasing the junction normal resistance to $\sim$ 100 ohm is expected to give better results.

9.2 Ultimate Limits to SIS Receivers

The success of this work indicates that in the near future millimeter-wave receivers using SIS mixers may approach the ultimate sensitivity limit imposed by quantum theory. The two outstanding questions still to be answered are: what high frequency limitations are there on SIS mixers, and what is the correct quantum noise limit for the SIS mixer?

1) The High Frequency Limitations of SIS Mixers.

Philips et al. [46] have reported SIS mixing results at 230 GHz. Recently, Sutton has observed SIS quasiparticle mixing, along with Josephson effect mixing for frequencies up to 388 GHz [65]. Based on the assumption that the high frequency limitation of an SIS quasiparticle mixer is governed by the sudden onset of Josephson effect noise below the drop-back voltage [15,52,53,57], Tucker and Feldman have estimated the upper frequency limit for pure quasiparticle mixing, in lead alloy junctions, to be 250 GHz and 350 GHz for $\omega R_N C = 2$ and 10 respectively [76].

2) The Fundamental Limit to the Mixer Noise Temperature.

Theoretically, an SIS mixer should have a minimum mixer noise temperature of the order of $\hbar\omega/k$ (= 5.5 K at 115 GHz), the quantum noise [19,76]. The measuring technique described in this work was not precise enough (with uncertainty of ± 15 K ≈ ± 3 $\hbar\omega/k$) to detect this noise. A new technique has been developed to measure T_M with an accruacy better than ± 2 K, and it is hoped that we should be able to gain a better understanding of the practical noise limits of SIS mixers in the near future.

9.3 Summary and Conclusions

The research reported in this thesis is in three main parts:

1) An experimental SIS mixer was constructed and used to verify quantitatively the predictions of Tucker's 3-frequency quantum mixer theory [18]. We also made the first observation of negative dc differential resistance and infinite available gain in an SIS mixer [33], non-classical effects which are not seen in conventional diode mixers.

2) Tucker's theory was then used to design an ultra-low noise SIS mixer for a 115.3 GHz spectral line receiver [43,44]. The noise temperature of this receiver, 83 K, is the lowest ever reported in this frequency range. The true single sideband nature of the SIS mixer removes the uncertainties usually associated with the unequal signal and image responses of conventional heterodyne receivers, and also reduces the overall system noise temperature by eliminating the sky noise at the image frequency. The receiver has proved to be very reliable and simple to use on the telescope.

3) The SIS receiver was used on the Columbia/GISS Sky Survey Telescope to detect seven distant molecular clouds towards the Cygnus-X region.

In conclusion, we have achieved the original goals of this research project, namely, to study the performance of the SIS mixer at 115 GHz and to develop an ultra sensitive SIS receiver for use on the Columbia-GISS 4-ft telescope. Our results have demonstrated that the SIS mixer is likely to be the best candidate for sensitive millimeter-wave detection in the future. The success of this project may influence the choice of receivers for use in the Very Long Baseline Array (VLBA) and Millimeter Array, both planned by the National Radio Astronomy Observatory, the Submillimeter Array now under consideration by the Harvard/Smithsonian Center for Astrophysics, and other future millimeter wave radio astronomy facilities.

APPENDIX I THE EXPERIMENTAL DETERMINATION OF THE EQUIVALENT INDUCTANCES L_I, L_{II}, AND L'

The equivalent circuit of the inductance measurement setup (Fig. 4-6) is reproduced in Fig. AI-1.

The unknown inductance can be determined as follows. The power coupled to the 50 ohm load with finite shunt inductance L is:

$$P_L = [V_0^2/(4 \times 50)] \times [4x^2/(1 + 4x^2)] \qquad \text{(AI-1)}$$

where $x = \omega L/50$ is the normalized reactance and ω is the signal frequency. Without the shunt inductance, the transmitted power is:

$$P_{L=\infty} = V_0^2/(4 \times 50) \qquad \text{(AI-2)}$$

Therefore, the ratio of these two powers is:

$$r = P_L/P_{L=\infty} = 4x^2/(1 + 4x^2)$$

$$= 4(\omega L)^2/[50^2 + 4(\omega L)^2] \qquad \text{(AI-3)}$$

and the unknown inductance can be determined from the power ratio r by the following equation:

$$L = (25/2\pi f)[1/(1/r - 1)^{1/2}] \qquad \text{(AI-4)}$$

A 300X scale model (see Fig. AI-2) was constructed for inductance measurement. As shown in Fig. AI-3, all the inductance measurements were made relative to the inductance of the full width (W) stripline. The results are summarized in Table 4-1.

APPENDIX II DETERMINATION OF THE EQUIVALENT CIRCUIT ELEMENTS OF THE TYPE-D MOUNT

In this section, we will describe the experimental procedure used to determine the equivalent circuit elements of the two port network which represents the transistion between the junction and the single-mode waveguide. As illustrated in Fig. 4-11, this two port network can be represented by a T-network which is shown in Fig. AII-1.

We have used the same 40X scale model (described in section 4.3) to measure the elements of this T-network. The printed circuit pattern, as shown in Fig. AII-2, is modified so that it produces a short circuit at plane A-A'. The original filter pattern already produces a short circuit at plane B-B' at the signal frequency. Therefore in the equivalent circuit shown in Fig. AII-3, the series reactance $X_{B/S} = 0$ and the embedding impedance Z_{emb} is given by:

$$Z_{emb} = jX_{L_1} + \{1/[1/jX_c + 1/(jX_{L_2} + Z_{W/G})]\}$$

$$= [-X_{L_1}X_c - X_{L_1}X_{L_2} - X_{L_2}X_c + Z_{W/G}(jX_{L_1} + jX_c)]$$

$$/ \ (jX_c + jX_{L_2} + Z_{W/G}) \qquad \text{(AII-1)}$$

It requires three independent measurements to determine the three unknowns:

1) Measure the impedance looking into port 2 while shorting port 1. Port 1 can be shorted by moving the main backshort to an appropriate position. The measured embedding impedance is:

$$Z_{mea} = jm_1 = jX_{L_1} + jX_{L_2}X_c \,/\, (X_{L_2} + X_c) \qquad \text{(AII-2)}$$

2) Replace the broadband load in the input waveguide by a sliding short circuit and adjust for an open circuit at port 1. The impedance measured at port 2 is:

$$Z_{mea} = jm_2 = j(X_{L_1} + X_c) \qquad \text{(AII-3)}$$

3) Adjust the impedance $Z_{W/G}$ at port 1 until the impedance measured at port 2 is open circuited. This value of $Z_{W/G}$ is given by:

$$Z_{W/G} = jm_3 = -j(X_{L_2} + X_c) \qquad \text{(AII-4)}$$

From equation AII-2, 3, 4, we can solve for X_{L_1}, X_{L_2} and X_c in terms of m_1, m_2 and m_3:

$$X_c = -[m_3 \times (m_1 - m_2)]^{1/2}$$

$$X_{L_1} = m_2 + [m_3 \times (m_1 - m_2)]^{1/2} \qquad \text{(AII-5)}$$

and

$$X_{L_2} = -m_3 + [m_3 \times (m_1 - m_2)]^{1/2}$$

Measurements were performed in 25 MHz intervals from 2.7 to 2.975 GHz corresponding to 108 to 119 GHz, the actual operating frequency range. Due to the residual errors within the network analyzer and the mechanical tolerances of the model, the accuracy of these measurements is limited to approximately ± 0.02 nH in L and ± 1 fF in C. The measured values of L_1, L_2 and C are summarized in Table 4-2.

FIGURE CAPTIONS

Fig. 2-1 Equivalent circuit of a mixer with large signal circuits to the right and small signal circuits to the left of the intrinsic junction which is characterized for small signals by the conversion matrix Y. The augmented network (broken line) includes all the sideband embedding admittances Y_m and is characterized for small signals by the augmented admittance matrix Y'. The equivalent signal current generator I_s is usually connected at port 1 of the augmented network during normal mixer operation, the other port being open circuited.

Fig. 2-2 The mixer small signal equivalent circuit with shot noise current source and thermal noise current source at each sideband port.

Fig. 3-1 Picture of a Princeton-NBS Pb(InAu)/oxide/Pb(Bi) 2-junction array. Each junction is 1.8 μm × 2.5 μm, defined by the SiO window.

Fig. 4-1 a) Type J-J mixer mount. It consists of an electroformed stepped waveguide transformer and a gold plated brass mixer body. A contacting backshort is used as tuning element. b) Side and top view of the SIS

chip-Substrate assembly. The lead alloy 14-junction array was fabricated by IBM. c) Main body of the mixer mount. The substrate lies sideways in the slot and is held in position by the spring wire which also maintains the dc and RF/IF ground between the substrate and block.

Fig. 4-2 a) Schematic diagram of the type-D mixer mount. The channel waveguide transformer is fabricated integral with the two halves of the block. The whole bolck is gold plated.

Fig. 4-2 b) Top and side views of the SIS chip and quartz substrate. The SIS chip was mounted on the substrate by cold welding with indium.

Fig. 4-3 Top view of the lower half of the 40X scale model of the type-D mixer block. Another coax cable, which is identical to the measurement cable, but short circuited at one end, is used as the phase reference for the network analyzer in the measurement.

Fig. 4-4 A block diagram of the measurement setup used for the impedance measurement on the mixer model.

Fig. 4-5 An enlarged view of the region in the vicinity of a) the SIS junction (quartz chip not shown) in the

actual mixer, b) the corresponding region in the model (the upper block of Stycast not shown), and c) the reference planes A-A' and B-B'. The actual mixer and the model only differ within the reference planes A-A' and B-B'. Also illustrated are the equivalent circuit elements for the junction and the test probe inside the reference planes.

Fig. 4-6 a) The measurement setup used to determine an unknown inductance. b) The equivalent circuit of the test setup.

Fig. 4-7 The equivalent circuit used in deriving Y_{emb} seen by the SIS junction from Y_{mea} which is measured on the mixer model.

Fig. 4-8 A Smith chart plot of the embedding admittance (C_J excluded) measured on the mixer model at 2.875 GHz (115 GHz in the actual mixer). Both conductance and susceptance are normalized to 1/(50 ohm). Each circle is obtained by fixing the side arm backshort at one position then moving the main backshort by half a guide-wavelength. The entire set of circles is obtained by repeating the whole process with different side arm backshort settings until it covers half a guide-wavelength. These circles cover all the admittance plane except for the forbidden

region indicated on the chart. The dotted line represents the corrected boundary of the forbidden region which includes the capacitive and inductive corrections shown in Fig. 4-5.

Fig. 4-9 Available embedding admittance seen by the intrinstic junction at 115 GHz. A junction capacitance C_J = 99 fF ($\omega R_N C_J$ = 6.7) is added in parallel to the external circuit.

Fig. 4-10 An approximate microwave equivalent circuit of the type-D mixer mount. The circuit between the junction and the single-mode waveguide is characterized by the two port T-network.

Fig. 4-11 A schematic drawing, showing the equivalent circuit elements surrounding the SIS array. They are idenfied as the elements of the T-network shown in Fig. 4-10.

Fig. 4-12 A simplified microwave equivalent circuit of type-D mount.

Fig. 4-13 Comparison of theoretically and experimentally determined forbidden region at 115 GHz. As described in the text, the measured values of L_1, L_2 and C, which are

small and have only ~ 20% accuracy, are used in the theoretical calculation. These errors caused the slight discrepancy shown in this plot.

Fig. 4-14 One of the possible tuning conditions for the short-circuited image case, calculated from the equivalent circuit using the network analysis program described in section 4.4.4. Here the embedding admittance (C_J included) seen by the intrinsic junction at 115.3 (+), 113.9 (■) and 112.5 GHz (●) is plotted on the Smith chart as a function of the two backshort settings. This plot was obtained by setting the main backshort at 0.058" and then changing the side arm backshort setting, 0.0005" per step, from 0.041" to 0.044". Also shown is the transmission loss (in dB) at each embedding admittance at the signal frequency.

Fig. 4-15 One of the possible tuning conditions for the short-circuited image case, calculated from the equivalent circuit using the network analysis program described in section 4.4.4. Here the embedding admittance (C_J included) seen by the intrinsic junction at 115.3 (+), 113.9 (■) and 112.5 GHz (●) is plotted on the Smith chart as a function of the two backshort settings. This plot was obtained by setting the main backshort at 0.056" and then changing the side arm backshort setting, 0.0005" per

step, from 0.042" to 0.045". Also shown is the transmission loss (in dB) at each embedding admittance at the signal frequency.

Fig. 4-16 One of the possible tuning conditions for the short-circuited image case, calculated from the equivalent circuit using the network analysis program described in section 4.4.4. Here the embedding admittance (C_J included) seen by the intrinsic junction at 115.3 (+), 113.9 (■) and 112.5 GHz (●) is plotted on the Smith chart as a function of the two backshort settings. This plot was obtained by setting the main backshort at 0.0641" and then changing the side arm backshort setting, 0.0005" per step, from 0.034" to 0.037". Also shown is the transmission loss (in dB) at each embedding admittance at the signal frequency.

Fig. 4-17 Loci of the embedding admittance seen by the junction at the signal (S), local oscillator (LO), and image (i) frequencies, measured on the 40X scale model of the type J-J mixer block. The array's capacitance C_J = 22.5 fF has been added.

Fig. 5-1 Microwave-cryogenic mixer testing set-up.

Fig. 5-2 The various noise temperature components of

dewar's IF section terminated with a 50 ohm cold load. The whole section is represented by a attenuator with loss α_{IF}.

Fig. 6-1 The various contributions to the measured noise power at the dewar's IF output port with A) no RF or IF noise power applied to the mixer, B) a known RF power, at signal or image frequency, applied to dewar's RF input port, C) a known IF noise power, $T_{N/S}$, injected into dewar's IF port. The performance of the mixer can be determined from these measurements. α_{RF} and α_{IF} are the measured attenuations of dewar's RF and IF sections, described in chapter 5.

Fig. 6-2 Typical experimental results of an IBM 14-junction array mixer. a) The unpumped dc I-V curve and b) the dc I-V curve with a LO power of 160 nW at 113.9 GHz applied to the mixer. c) - e) Shows the output of the 1.4 GHz IF radiometer with c) a known IF noise power applied to the mixer's IF port, d) a 115.3 GHz monochromatic signal source (upper sideband) applied to mixer's RF port and e) no RF or IF power applied; all with P_{LO} = 160 nW.

Fig. 6-3 Same as Fig. 6-2, except d) a 112.5 GHz monochromatic source was applied to mixer to measure the lower sideband performance.

Fig. 6-4 Similar experimental results for the same 14-junction array mixer shown in Fig. 6-2 but under different tuning conditions. The pumped dc I-V curve b) shows a region of negative differential resistance at the first photon step. The IF reflection coefficient, represented by curve c), is slightly larger than unity at 38 mV. This implys a negative resistance at the 1.4 GHz IF. The structure seen in the curves below about 28 mV is very sensitive to the applied magnetic field and is caused by Josephson effect. The LO power is 375 nW.

Fig. 6-5 Typical experimental results of an NBS 2-junction array mixer. a) The unpumped dc I-V curve and b) the dc I-V curve with a LO power of 250 nW at 113.9GHz applied to the mixer. c) - e) Shows the output of the 1.4 GHz IF radiometer with c) a known IF noise power applied to the mixer's IF port, d) a 115.3 GHz monochromatic signal source (upper sideband) applied to mixer's RF port and e) no RF or IF power applied; all with P_{LO} = 250 nW.

Fig. 6-6 Same as Fig. 6-5, except d) a 112.5 GHz monochromatic source was applied to mixer to measure the lower sideband performance.

Fig. 6-7 a) The unpumped dc I-V curve for a 14-junction

SIS array. b) The dc I-V curve with P_{LO} = 180 nW applied to the mixer. c) The conversion gain with P_{LO} = 180 nW and backshort position = 0.248". The four large dots, at 38 mV and 31 mV, represent the experimental data points chosen from this backshort setting and used in Fig. 6-8 to compare with the theoretical calculation.

Fig. 6-8 The four data points chosen from each of the backshort setting, as illustrated in Fig. 6-7, are plotted in here: a) the pumped dc current and b) the conversion gain, both measured at 38 mV with P_{LO} = 180 ± 40 nW for nine backshort settings, c) and d) are the same as a) and b) respectively, but measured at 31 mV. The solid curves are the theoretical values calculated for C = 22.5 fF and P_{LO} = 173 nW.

Fig. 6-9 Contours of the predicted conversion loss, calculated for optimum bias voltage (at the first photon step) and optimum α, assuming the image short-circuited, on the Smith chart of embedding admittance, normalized to 1/(50 ohm). Negative differential resistance is expected to appear on the pumped dc I-V curve in the first photon step if the LO embedding admittance lies in the shaded region (again, α is optimized at each point).

Fig. 7-1 Block diagram of the SIS receiver front-end,

showing the LO source, receiver dewar, the LO leveling loop and the bias voltage leveling loop.

Fig. 7-2 Picture of the completed 115 GHz SIS receiver. The principle elements on the 2.5 K cold stage are: 20-dB cross-guide coupler, SIS mixer, bias-tee, 1.4 GHz isolator and the L-Band FET amplifier. The 115.3 GHz RF input is a room temperature scalar feed horn.

Fig. 7-3 a) dc I-V curve of the unpumped 2-junction SIS array at T = 2.5 K b) dc I-V curve with LO power of 250 nW at 113.9 GHz applied to the mixer. c) and d) are the receiver's 1.4 GHz IF output with room temperature load and liquid nitrogen load placed in front of the horn. The receiver is tuned for > 25 dB image rejection ratio.

Fig. 7-4 Breakdown of the SIS receiver noise temperature (SSB) at various points along the signal path (f_{sig} = 115.3 GHz). T_M was deduced from the other measured and calculated quantities.

Fig. 7-5 Reveiver's instantaneous bandwidth; data obtained with f_{LO}, P_{LO}, V_{dc} and backshort settings unchanged.

Fig. 7-6 The receiver's noise temperature versus signal

frequency, for both upper-sideband (□) and lower sideband (●) operation. By installing a new SIS array and retuning the FET amplifier, T_R = 83 K, indicated by (▲) in this plot, was obtained at 115.3 GHz. The receiver is tuned for > 20 dB image rejection. Better results can be achieved by relaxing the image rejection ratio, e.g. with 12 dB image rejection ratio, T_R = 68 K was obtained at 112.3 GHz as noted on the figure. The uncertainty in T_R is ± 3 K.

Fig. 8-1 Sampling map of the CO observation towards the Cygnus-X region; each observed point is marked by '+'.

Fig. 8-2 Spectrum of the peak of each cloud listed in Table 8-1. All spectra have a linear baseline removed.

Fig. 8-3 Spatial map of the CO emission integrated over velocity from -55 to -35 km s^{-1}. The contour interval is 1.5 K km s^{-1}. This is the largest cloud (No. 5) detected in this survey.

Fig. 8-4 The locations in the galactic plane of the large clouds compiled in Table 8-1. The circle sizes are proportional to the cube-roots of the cloud masses and a mass scale is shown.

Fig. AI-1 The equivalent circuit for inductance measurement. The unknown inductance is shunted across the 50 ohm circuit and can be determined by measuring the power delivered to the load.

Fig. AI-2 A 300X scale model used for inductance measurement.

Fig. AI-3 a) The inductance (L_0) of the full width (W) stripline is used as the reference in the inductance measurements. b) and c) The magnetic energy stored in area I and II can be characterized by the equivalent inductances L_I and L_{II} respectively. d) The inductance of the center conductor of the test probe.

Fig. AII-1 The elements of the equivalent T-network between the junction and the single-moded waveguide.

Fig. AII-2 A schematic drawing showing the modified printed circuit pattern used to determine the values of L_1, L_2 and C. These circuit patterns produce a short circuit at planes A-A' and B-B'.

Fig. AII-3 The equivalent circuit of the mixer mount with the modified stripline circuit pattern.

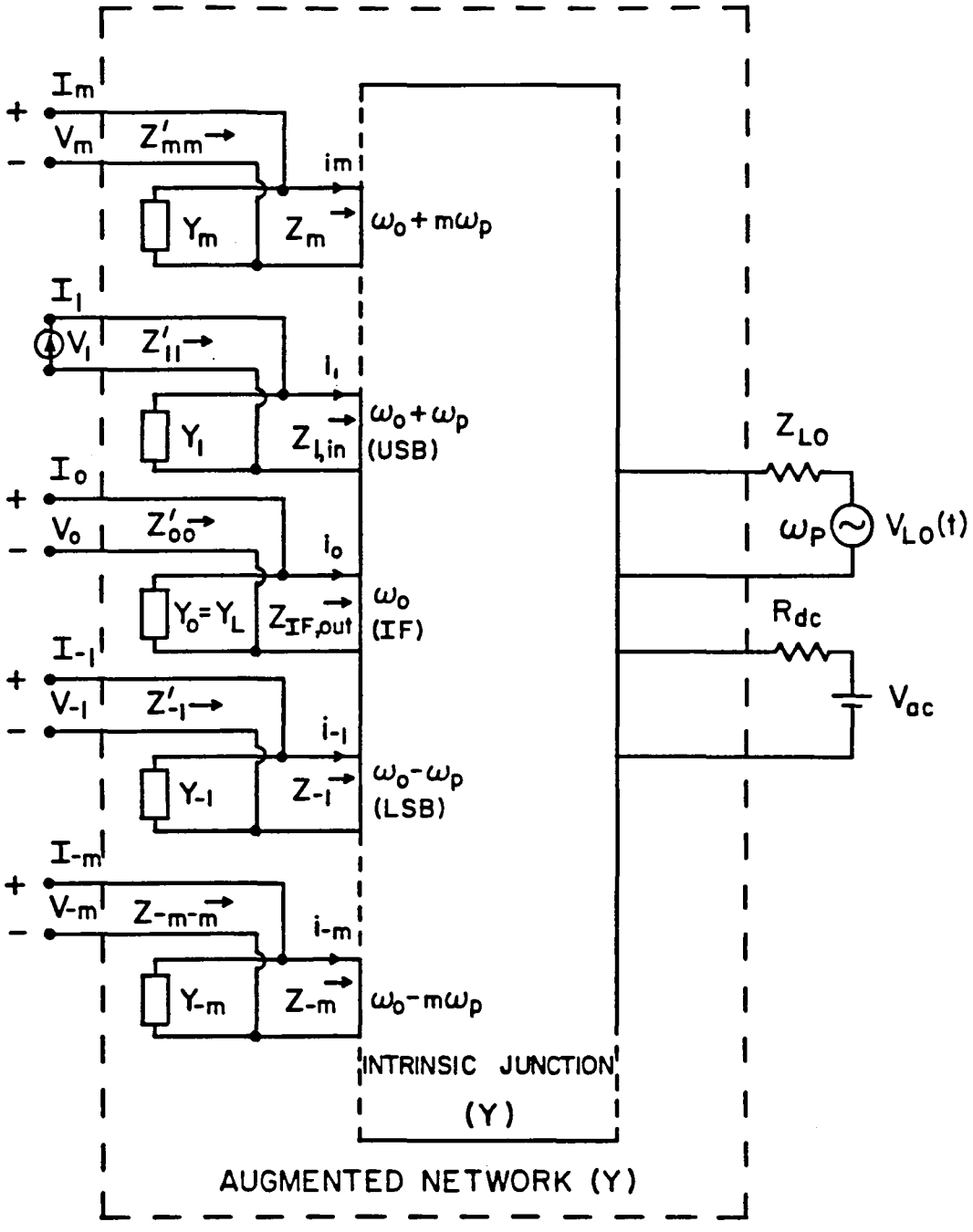
I_m
V_m
Z'_{mm}
i_m
Y_m
Z_m
$\omega_o + m\omega_p$
I_1
V_1
Z'_{11}
i_1
Y_1
$Z_{1,in}$
$\omega_o + \omega_p$
(USB)
I_o
V_o
Z'_{oo}
i_o
$Y_o = Y_L$
$Z_{IF,out}$
ω_o
(IF)
I_{-1}
V_{-1}
Z'_{-1}
i_{-1}
Y_{-1}
Z_{-1}
$\omega_o - \omega_p$
(LSB)
I_{-m}
V_{-m}
Z_{-m-m}
i_{-m}
Y_{-m}
Z_{-m}
$\omega_o - m\omega_p$
INTRINSIC JUNCTION
(Y)
AUGMENTED NETWORK (Y)
Z_{LO}
ω_P
$V_{LO}(t)$
R_{dc}
V_{dc}

Fig. 2-1

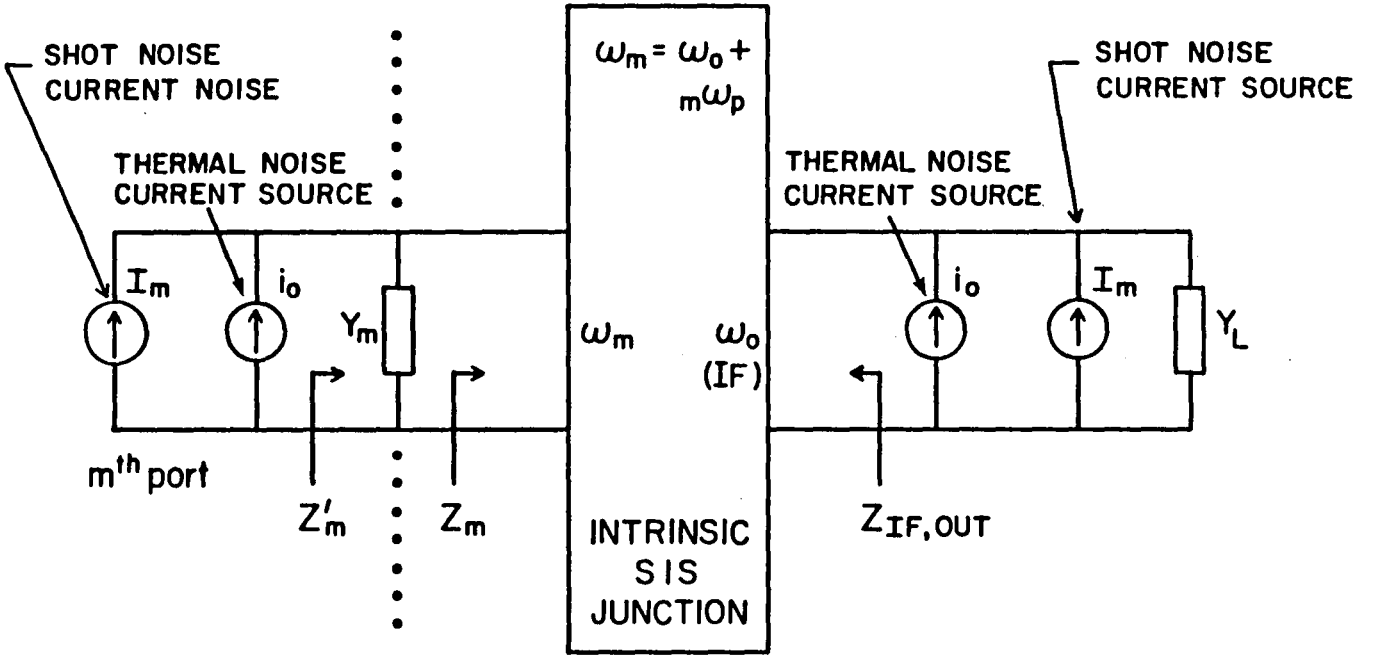
SHOT NOISE
CURRENT NOISE
THERMAL NOISE
CURRENT SOURCE
I_m
i_o
Y_m
m^{th} port
Z'_m
Z_m
$\omega_m = \omega_o + m\omega_p$
ω_m
ω_o
(IF)
INTRINSIC
SIS
JUNCTION
SHOT NOISE
CURRENT SOURCE
THERMAL NOISE
CURRENT SOURCE
i_o
I_m
Y_L
$Z_{IF,OUT}$

Fig. 2-2

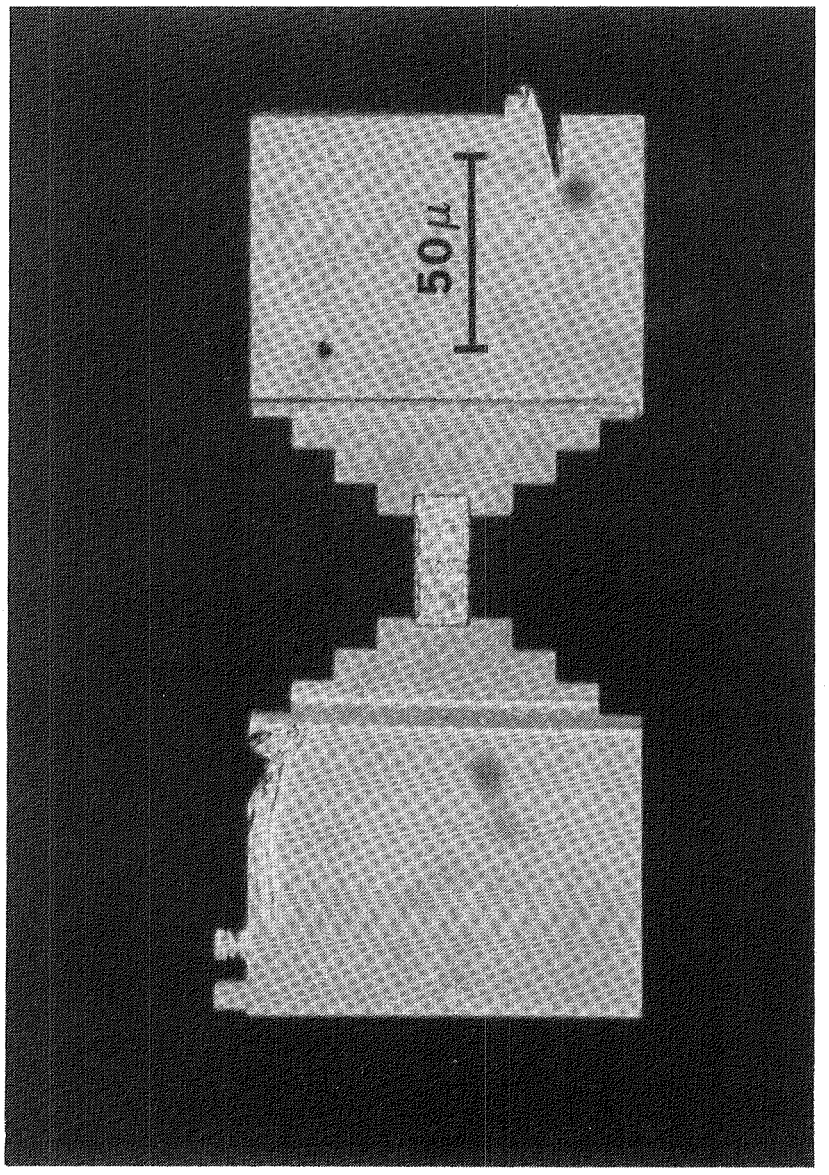

Fig. 3-1

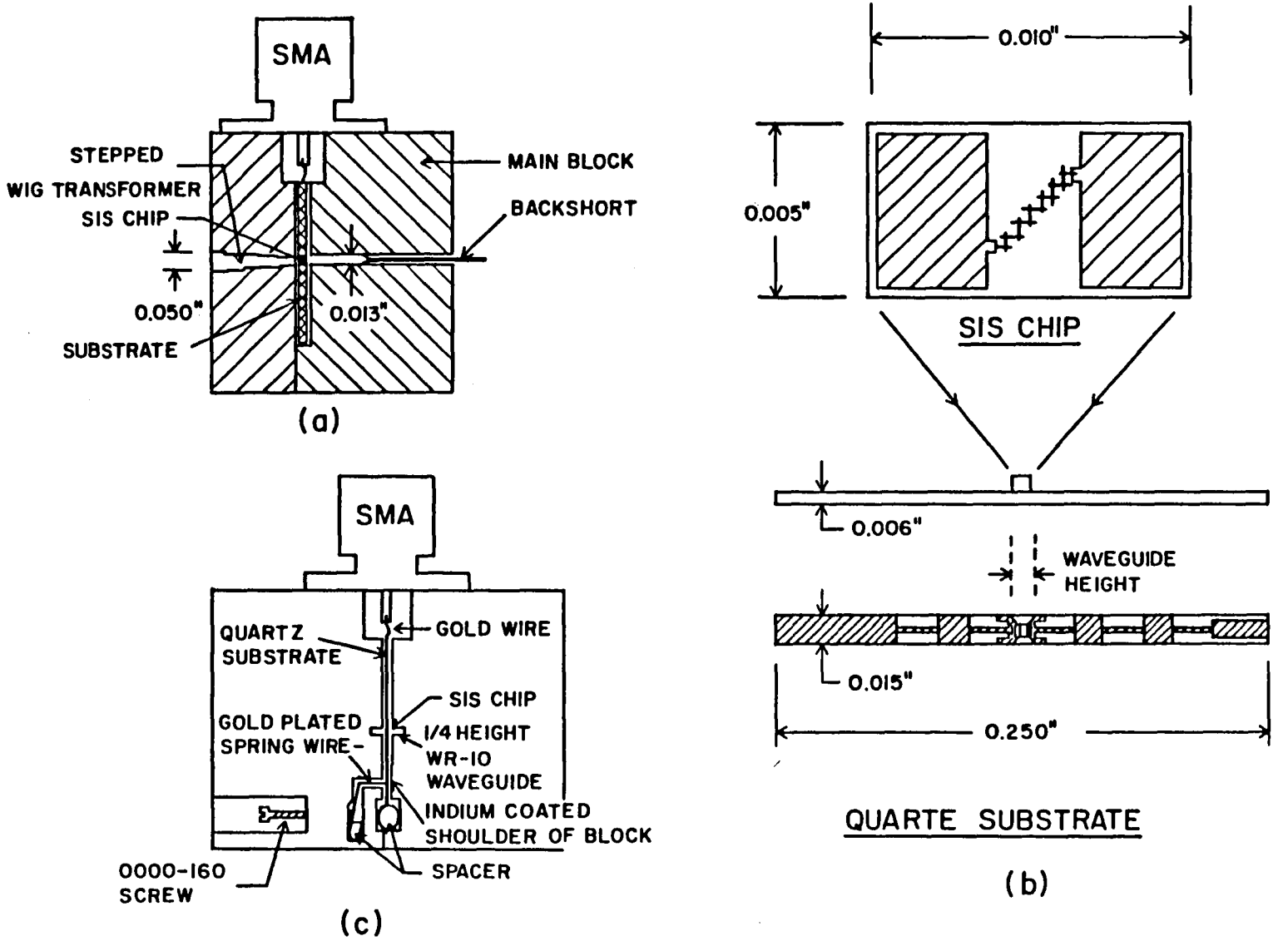
SMA
STEPPED
WIG TRANSFORMER
SIS CHIP
MAIN BLOCK
BACKSHORT
0.050"
0.013"
SUBSTRATE
(a)
SMA
QUARTZ
SUBSTRATE
GOLD WIRE
SIS CHIP
GOLD PLATED
SPRING WIRE
1/4 HEIGHT
WR-10
WAVEGUIDE
INDIUM COATED
SHOULDER OF BLOCK
0000-160
SCREW
SPACER
(c)
0.010"
0.005"
SIS CHIP
0.006"
WAVEGUIDE
HEIGHT
0.015"
0.250"
QUARTE SUBSTRATE
(b)

Fig. 4-1

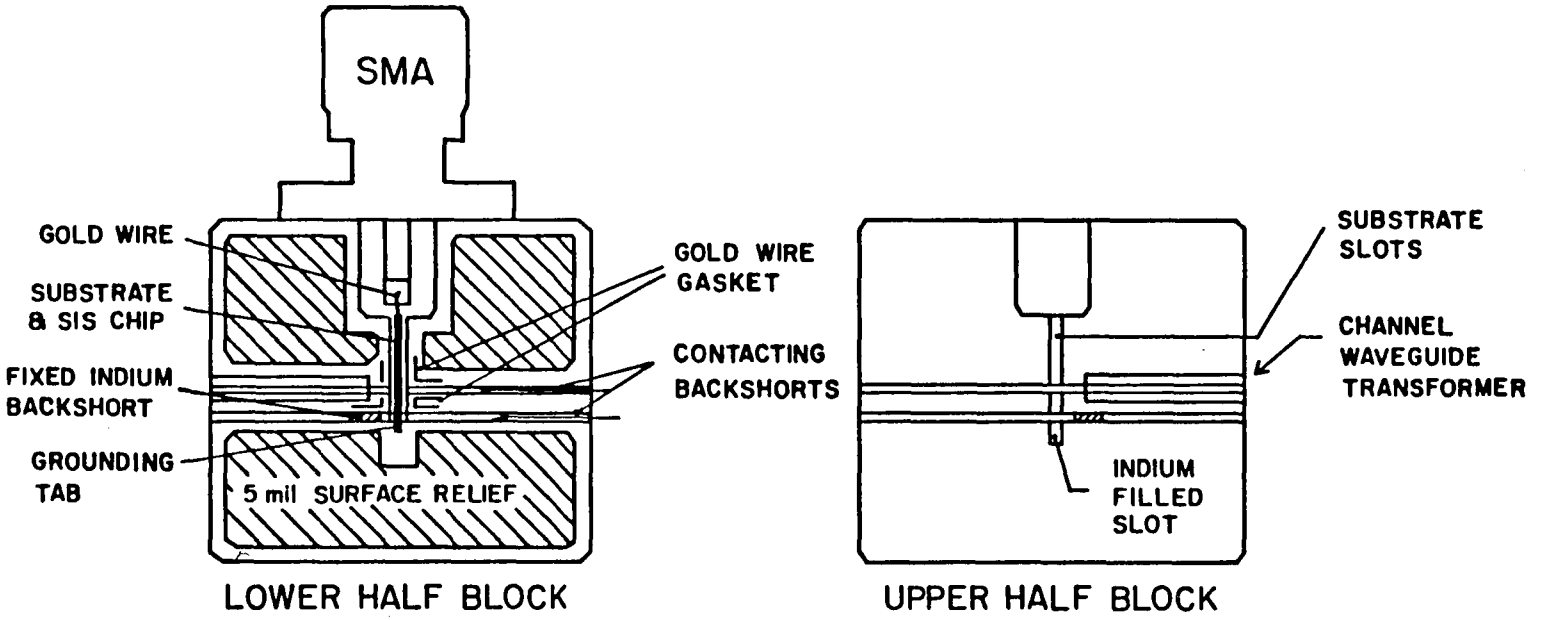
SMA
GOLD WIRE
SUBSTRATE & SIS CHIP
FIXED INDIUM BACKSHORT
GROUNDING TAB
5 mil SURFACE RELIEF
GOLD WIRE GASKET
CONTACTING BACKSHORTS
LOWER HALF BLOCK
SUBSTRATE SLOTS
CHANNEL WAVEGUIDE TRANSFORMER
INDIUM FILLED SLOT
UPPER HALF BLOCK

Fig. 4-2 a)

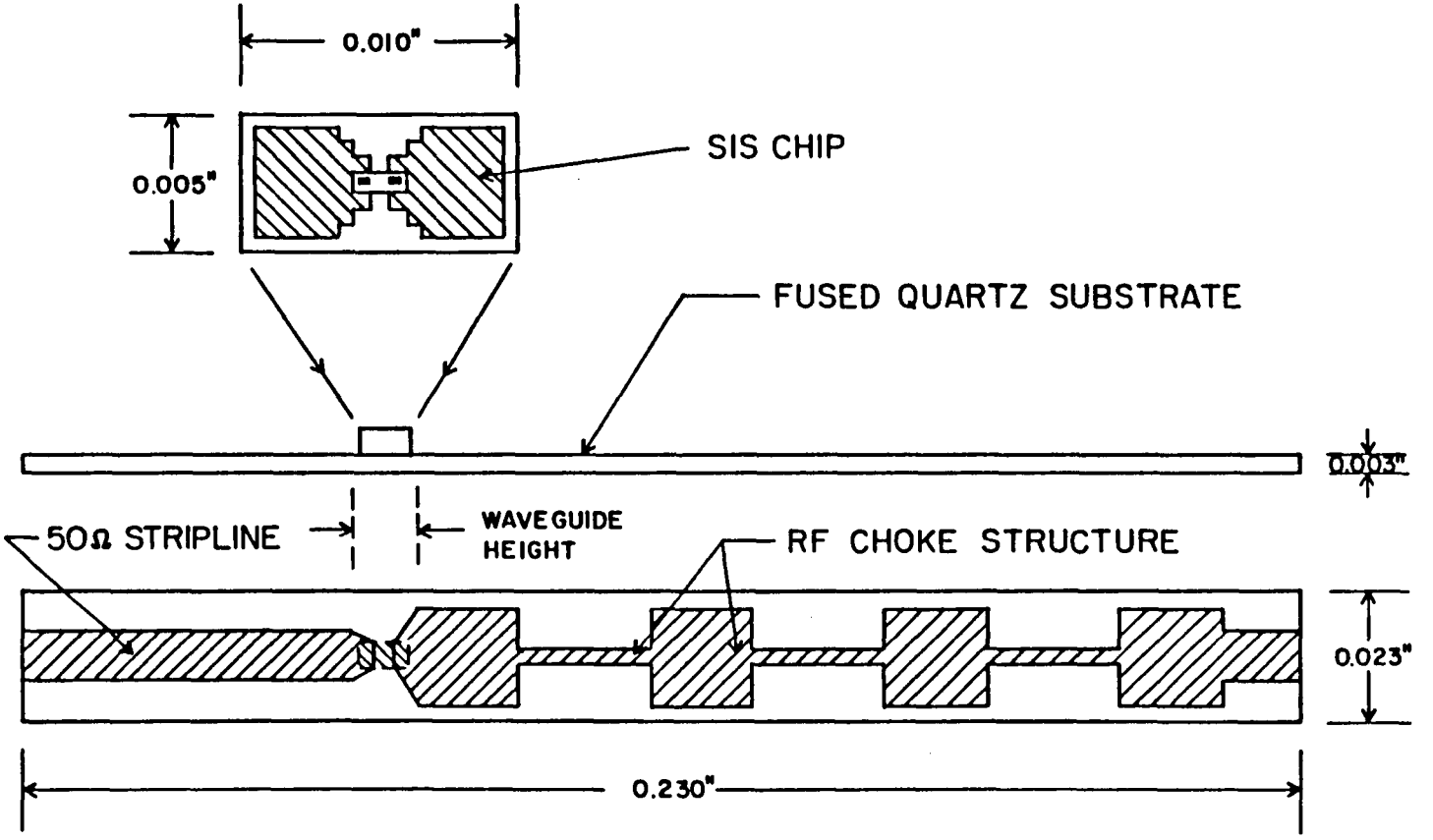
0.010"
0.005"
SIS CHIP
FUSED QUARTZ SUBSTRATE
0.003"
50Ω STRIPLINE
WAVEGUIDE HEIGHT
RF CHOKE STRUCTURE
0.023"
0.230"

Fig. 4-2 b)

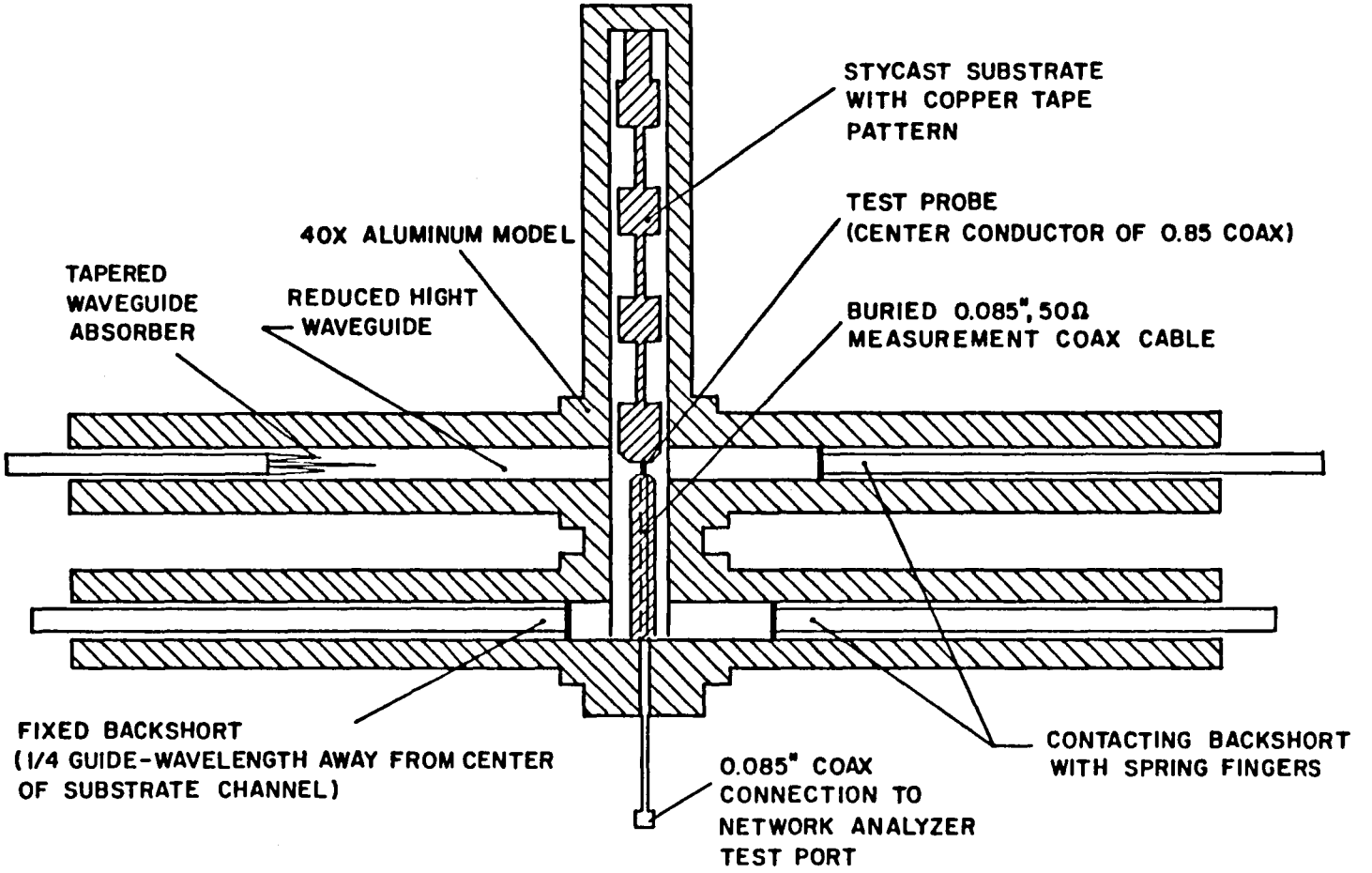
STYCAST SUBSTRATE
WITH COPPER TAPE
PATTERN
TEST PROBE
(CENTER CONDUCTOR OF 0.85 COAX)
40X ALUMINUM MODEL
TAPERED
WAVEGUIDE
ABSORBER
REDUCED HIGHT
WAVEGUIDE
BURIED 0.085", 50Ω
MEASUREMENT COAX CABLE
FIXED BACKSHORT
(1/4 GUIDE-WAVELENGTH AWAY FROM CENTER
OF SUBSTRATE CHANNEL)
0.085" COAX
CONNECTION TO
NETWORK ANALYZER
TEST PORT
CONTACTING BACKSHORT
WITH SPRING FINGERS

Fig. 4-3

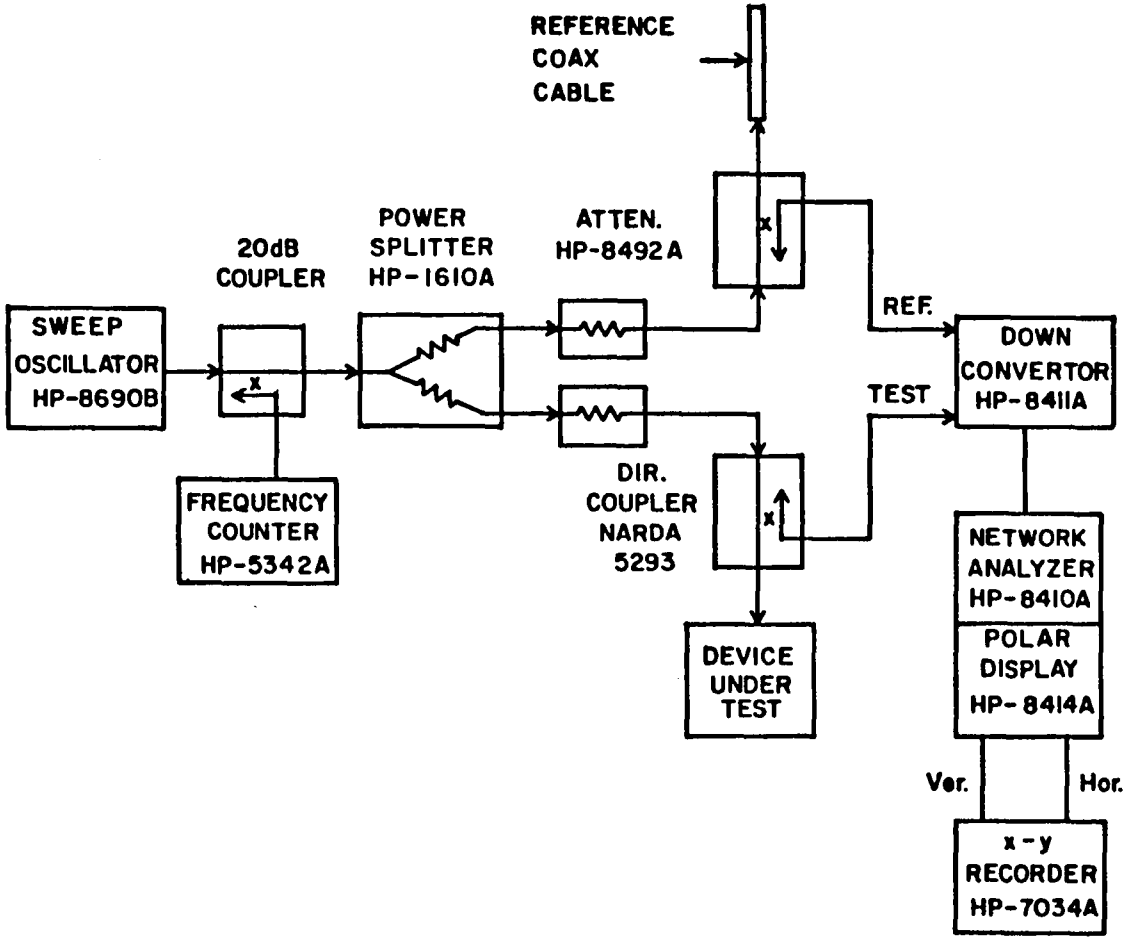
REFERENCE
COAX
CABLE
SWEEP
OSCILLATOR
HP-8690B
20dB
COUPLER
POWER
SPLITTER
HP-1610A
ATTEN.
HP-8492A
FREQUENCY
COUNTER
HP-5342A
DIR.
COUPLER
NARDA
5293
DEVICE
UNDER
TEST
REF.
TEST
DOWN
CONVERTOR
HP-8411A
NETWORK
ANALYZER
HP-8410A
POLAR
DISPLAY
HP-8414A
Ver.
Hor.
x-y
RECORDER
HP-7034A

Fig. 4-4

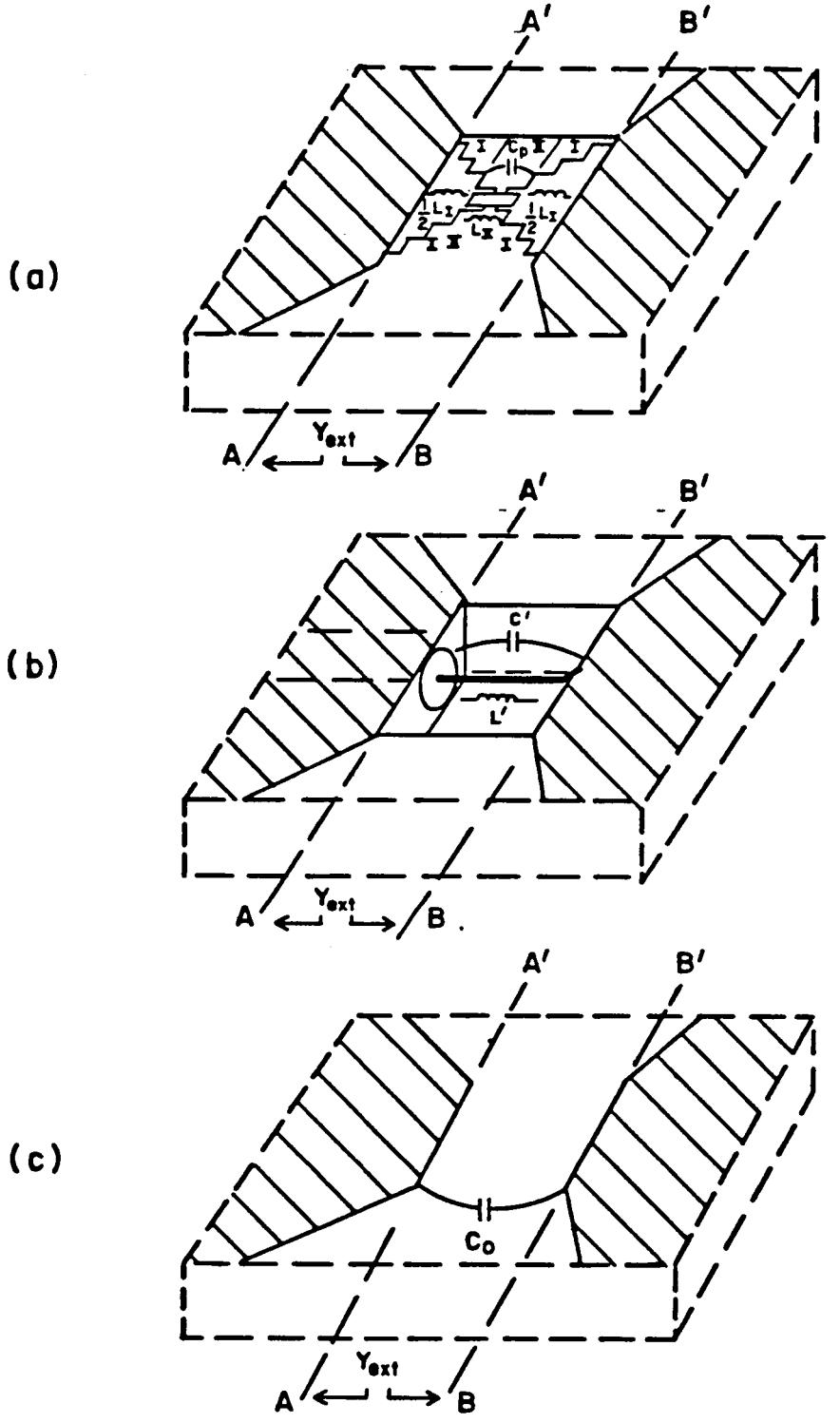

Fig. 4-5

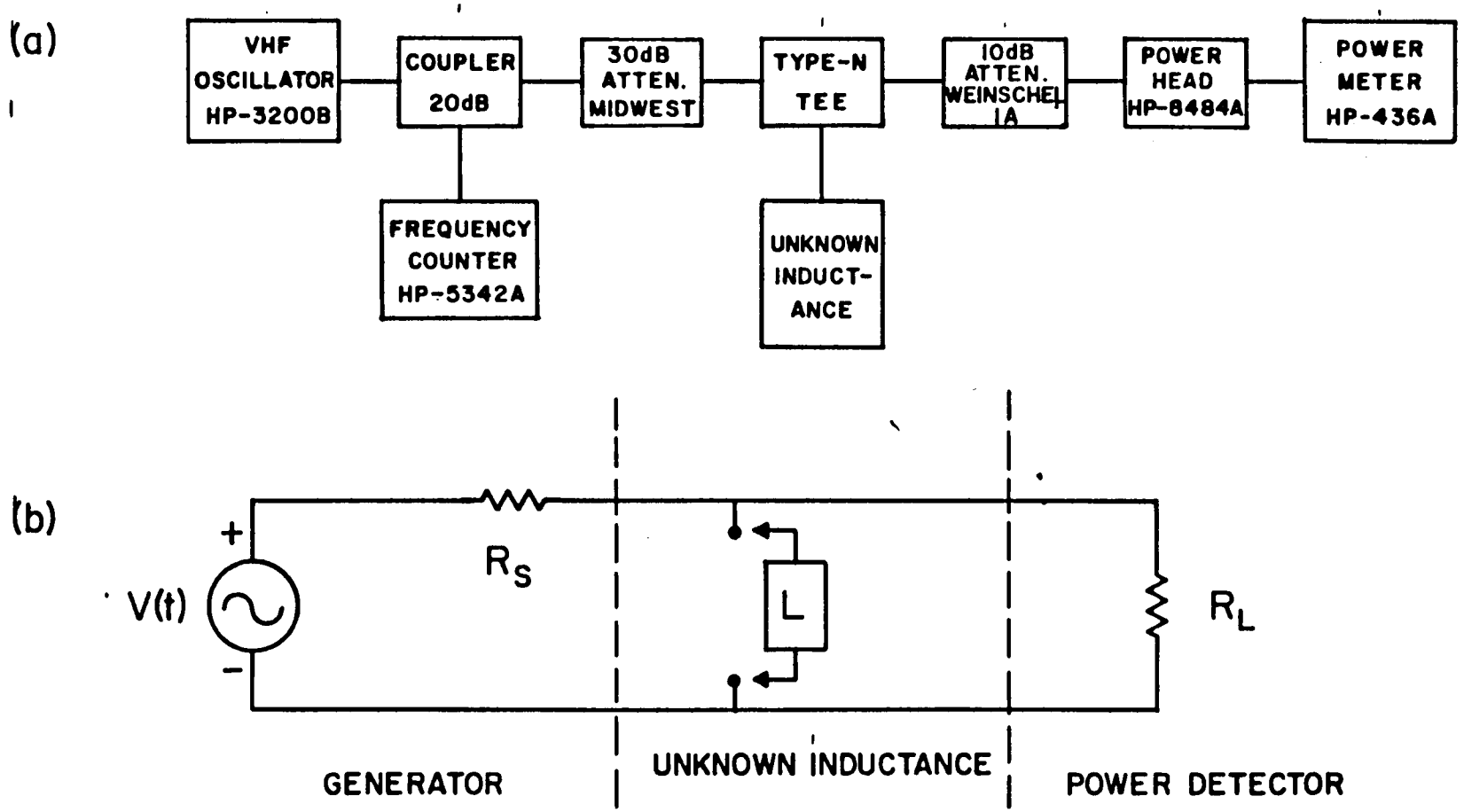
(a)
VHF OSCILLATOR HP-3200B
COUPLER 20dB
30dB ATTEN. MIDWEST
TYPE-N TEE
10dB ATTEN. WEINSCHEL 1A
POWER HEAD HP-8484A
POWER METER HP-436A
FREQUENCY COUNTER HP-5342A
UNKNOWN INDUCT-ANCE
(b)
+
V(t)
−
R_S
L
R_L
GENERATOR
UNKNOWN INDUCTANCE
POWER DETECTOR

Fig. 4-6

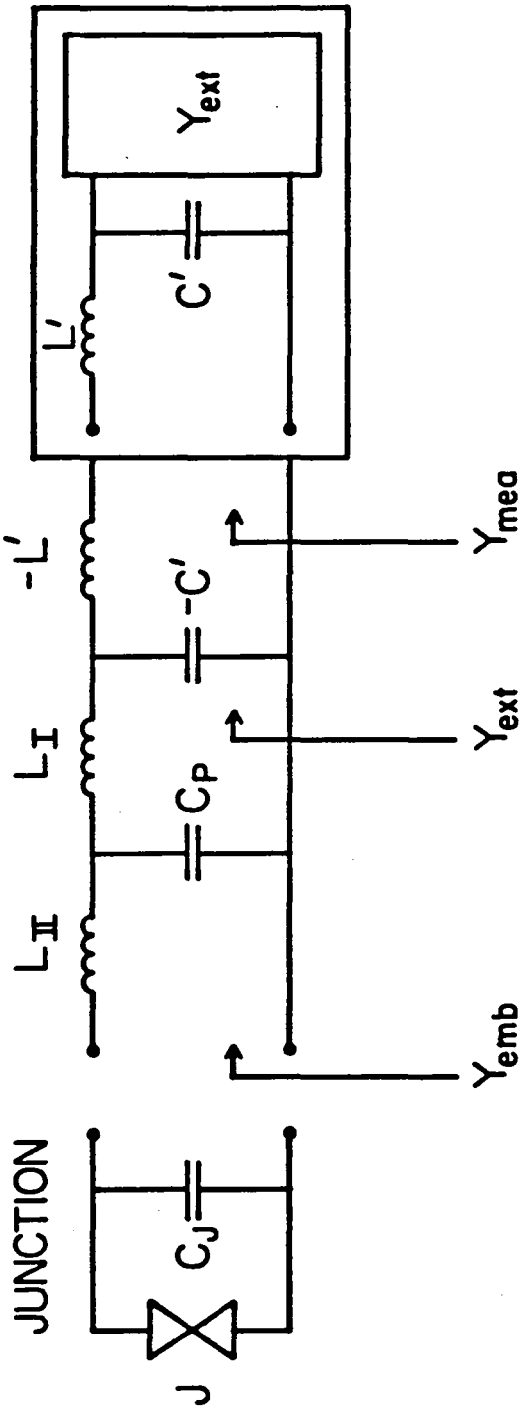

Fig. 4-7

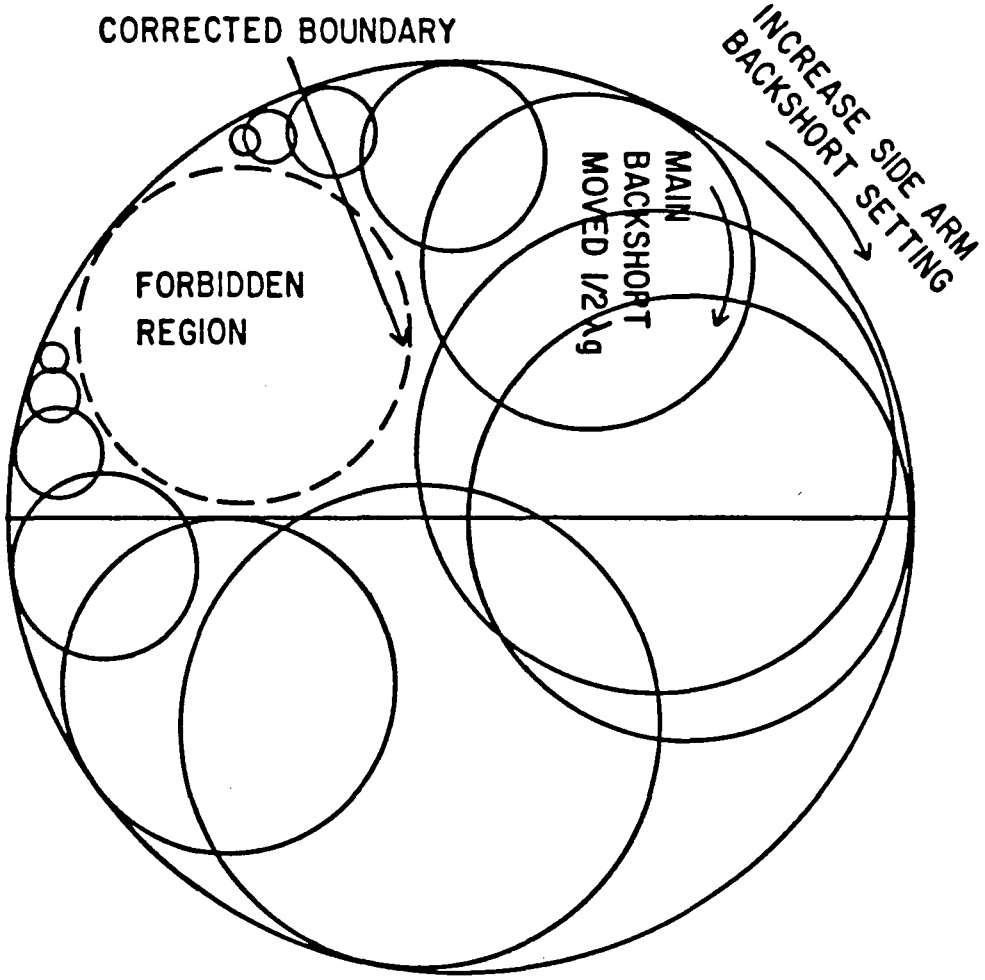
INCREASE SIDE ARM
BACKSHORT SETTING
MAIN
BACKSHORT
MOVED 1/2λg
CORRECTED BOUNDARY
FORBIDDEN
REGION

Fig. 4-8

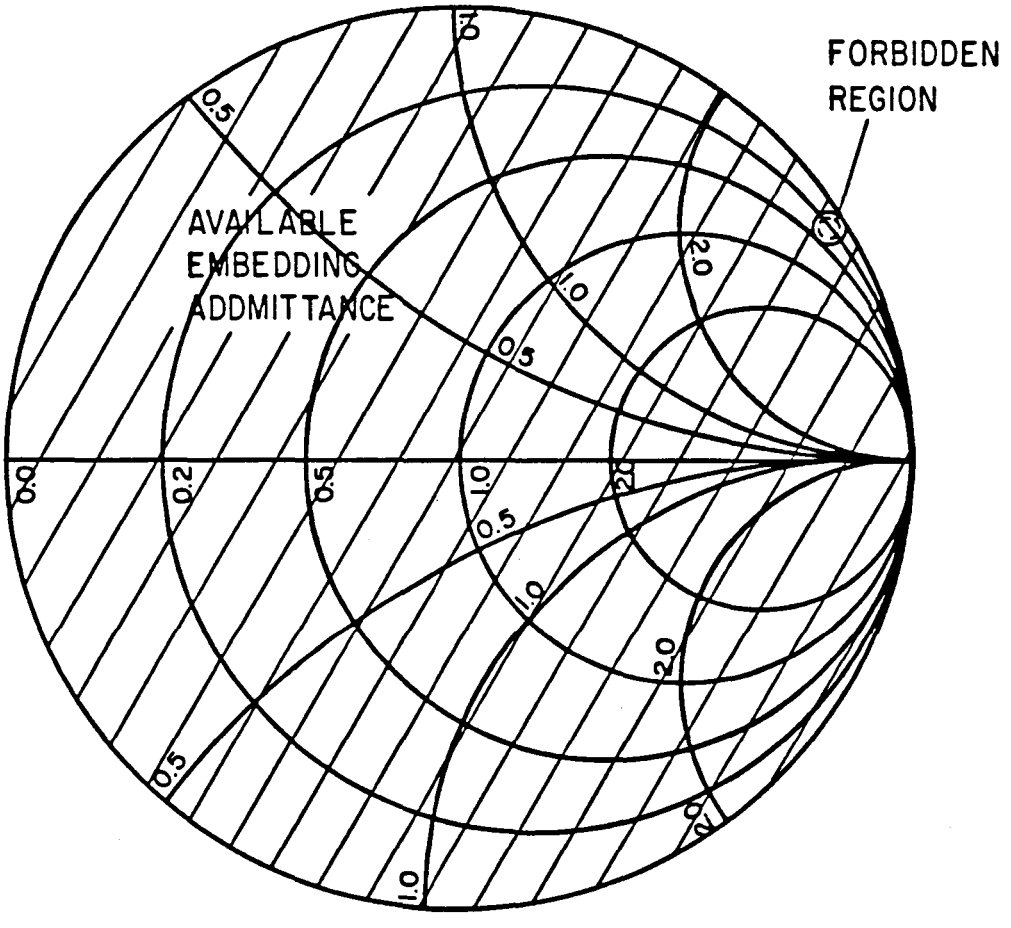
FORBIDDEN
REGION
AVAILABLE
EMBEDDING
ADDMITTANCE
0.0
0.2
0.5
1.0
2.0
0.5
1.0
2.0
0.5
1.0
2.0
0.5
1.0
2.0
0.5
1.0
2.0

Fig. 4-9

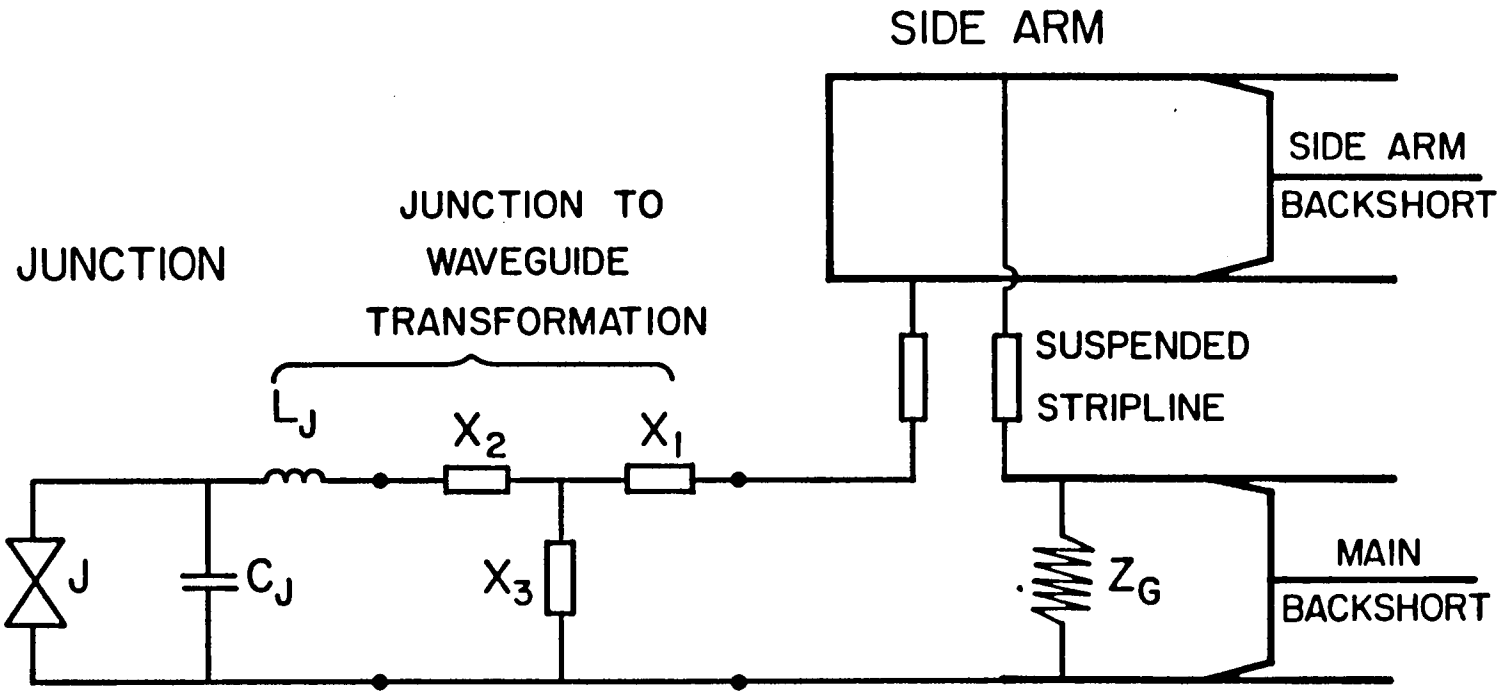
SIDE ARM
SIDE ARM
BACKSHORT
JUNCTION
JUNCTION TO
WAVEGUIDE
TRANSFORMATION
SUSPENDED
STRIPLINE
L_J
X_2
X_1
J
C_J
X_3
Z_G
MAIN
BACKSHORT

Fig. 4-10

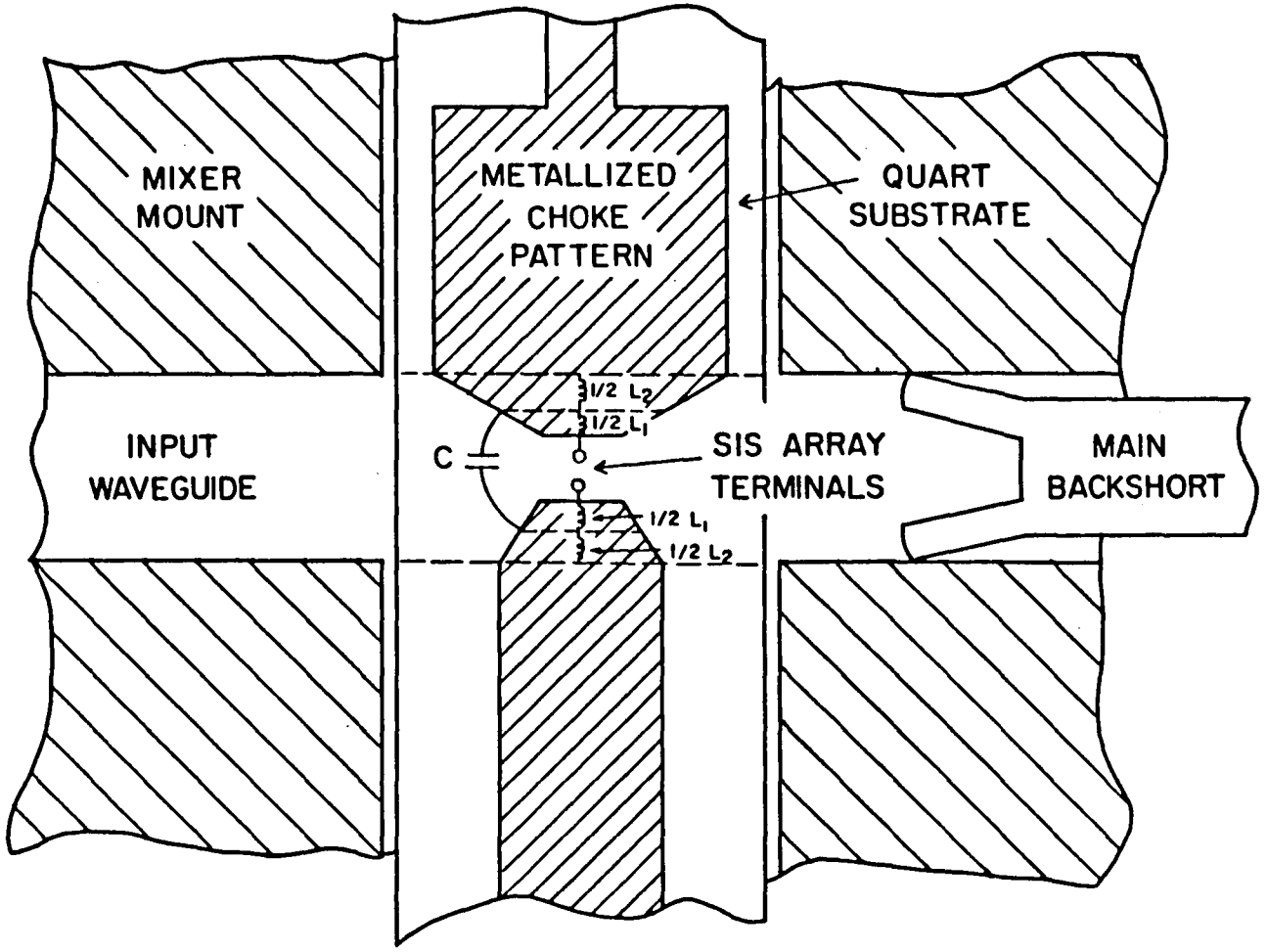
MIXER
MOUNT
METALLIZED
CHOKE
PATTERN
QUART
SUBSTRATE
1/2 L2
1/2 L1
INPUT
WAVEGUIDE
C
SIS ARRAY
TERMINALS
MAIN
BACKSHORT
1/2 L1
1/2 L2

Fig. 4-11

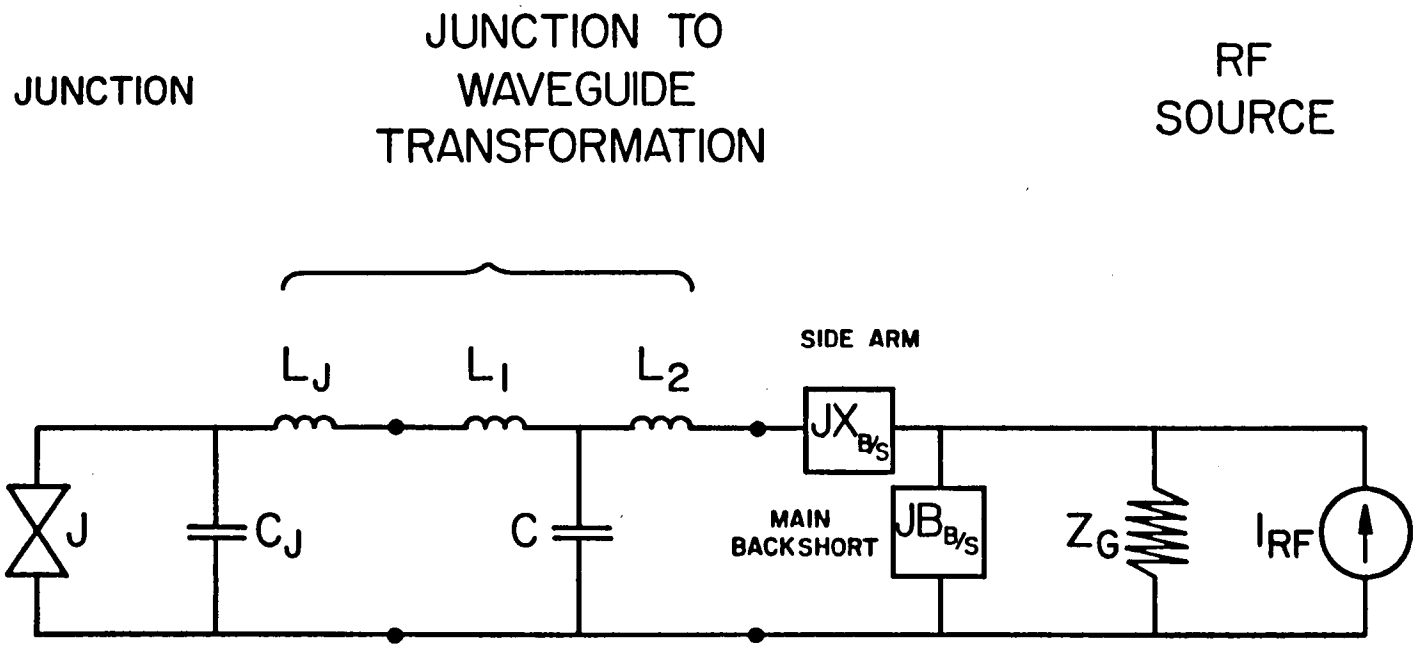
JUNCTION
JUNCTION TO WAVEGUIDE TRANSFORMATION
RF SOURCE
SIDE ARM
L_J
L_1
L_2
$JX_{B/S}$
J
C_J
C
MAIN BACKSHORT
$JB_{B/S}$
Z_G
I_{RF}

Fig. 4-12

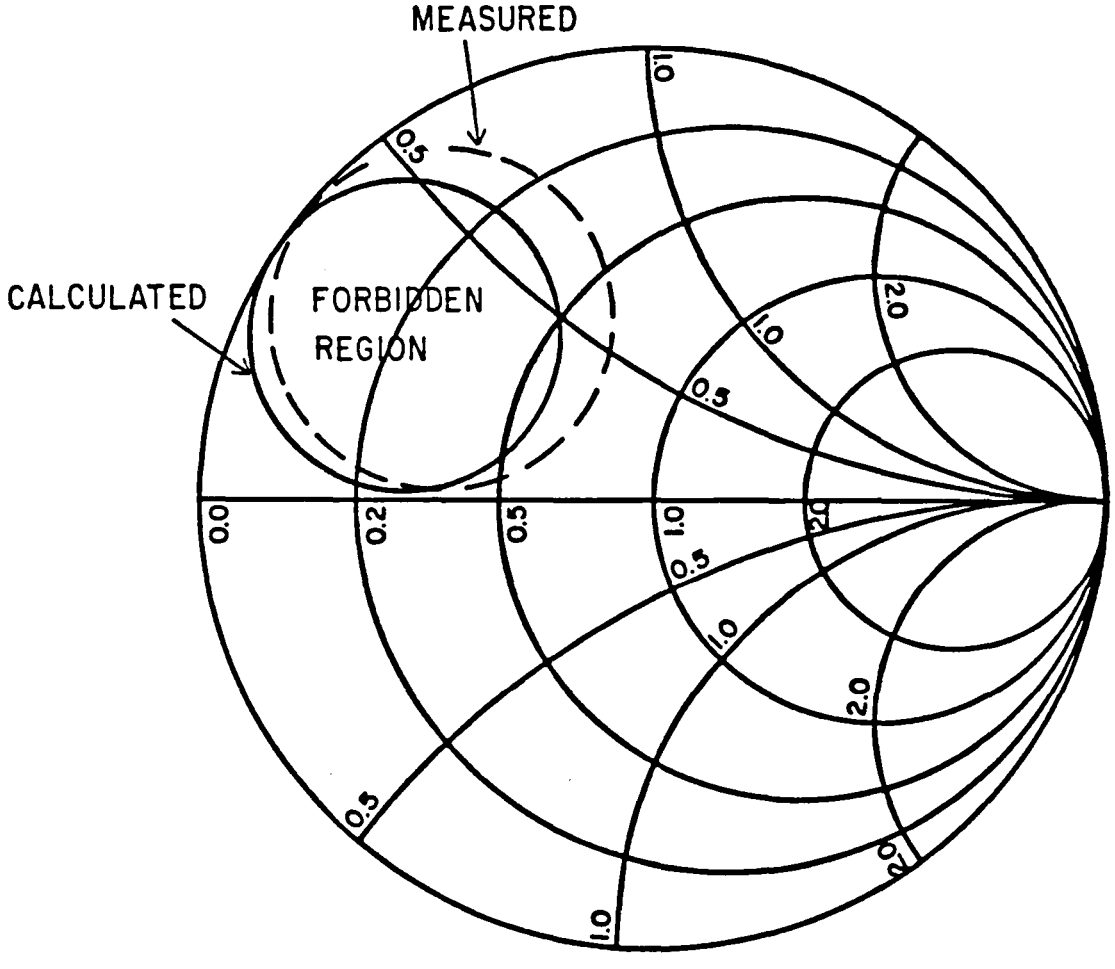
MEASURED
CALCULATED
FORBIDDEN
REGION
0.0
0.2
0.5
1.0
2.0
0.5
1.0
2.0
0.5
1.0
2.0
0.5
1.0
2.0
0.5
1.0
2.0

Fig. 4-13

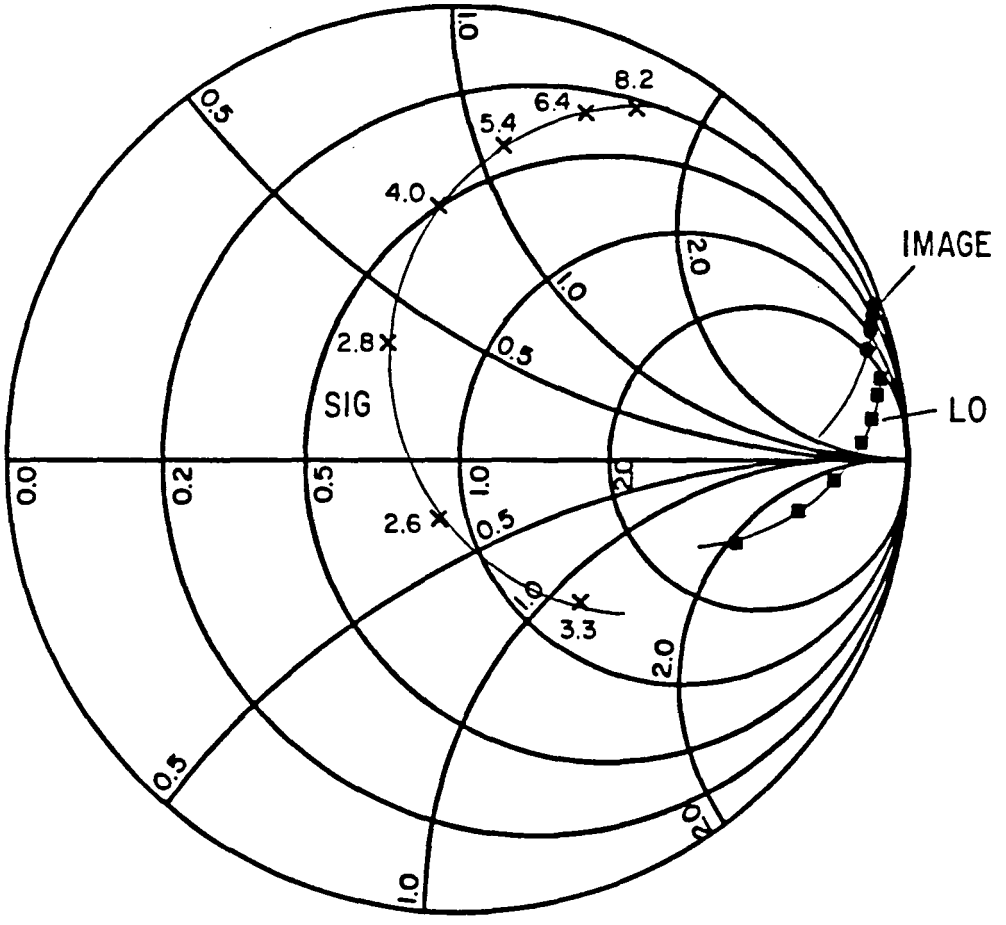
0.0
0.2
0.5
1.0
2.0
0.5
1.0
2.0
0.5
1.0
2.0
0.5
1.0
2.0
2.6
2.8
3.3
4.0
5.4
6.4
8.2
SIG
IMAGE
LO

Fig. 4-14

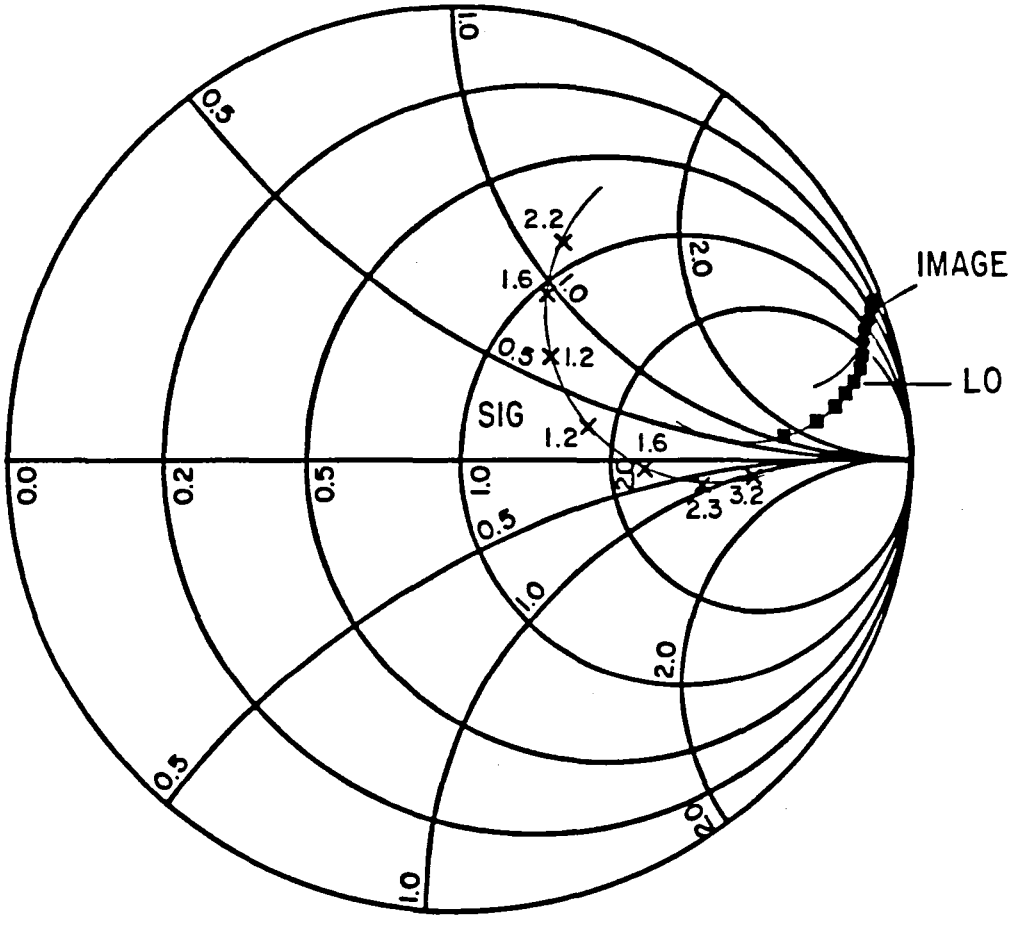
IMAGE
LO
SIG
0.0
0.2
0.5
1.0
2.0
0.5
1.0
2.0
0.5
1.0
2.0
0.5
1.0
2.0
2.2
1.6
1.0
0.5
1.2
1.2
1.6
2.0
2.3
3.2

Fig. 4-15

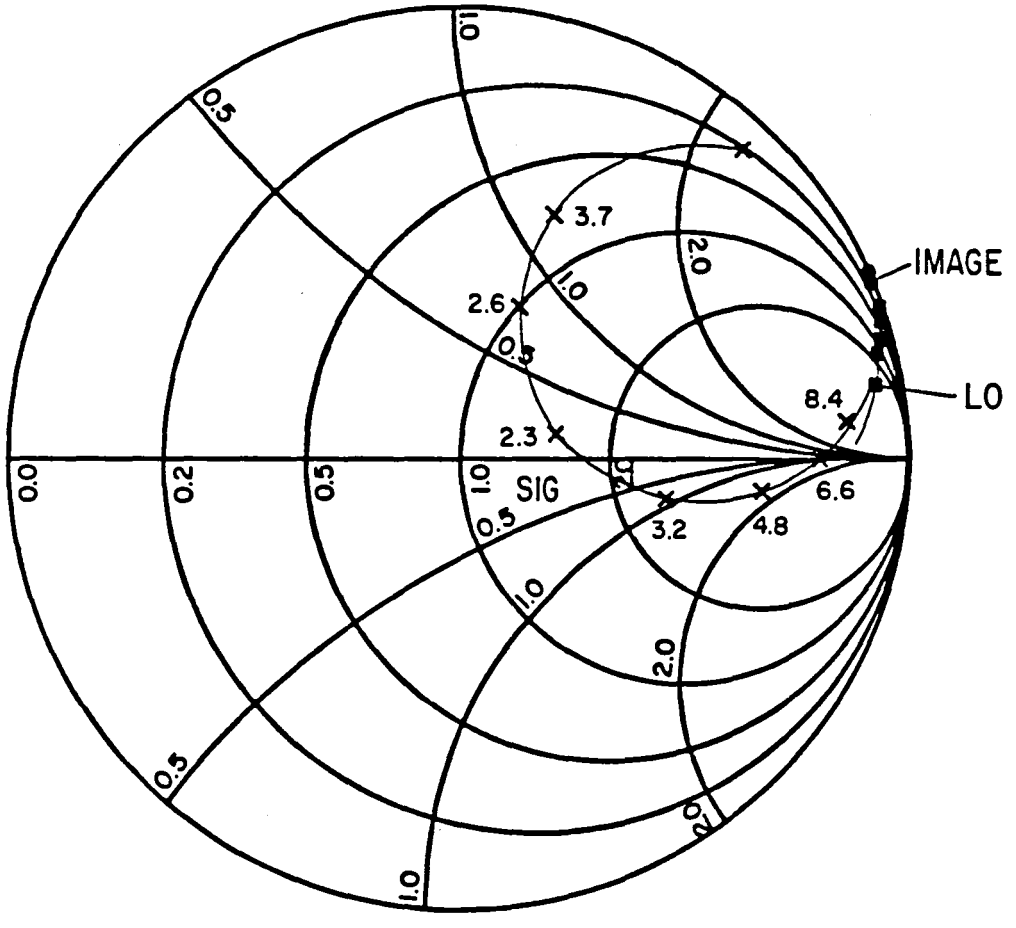
0.0
0.2
0.5
1.0
2.0
0.5
1.0
2.0
0.5
1.0
2.0
0.5
1.0
2.0
SIG
IMAGE
LO
2.3
2.6
3.7
3.2
4.8
6.6
8.4

Fig. 4-16

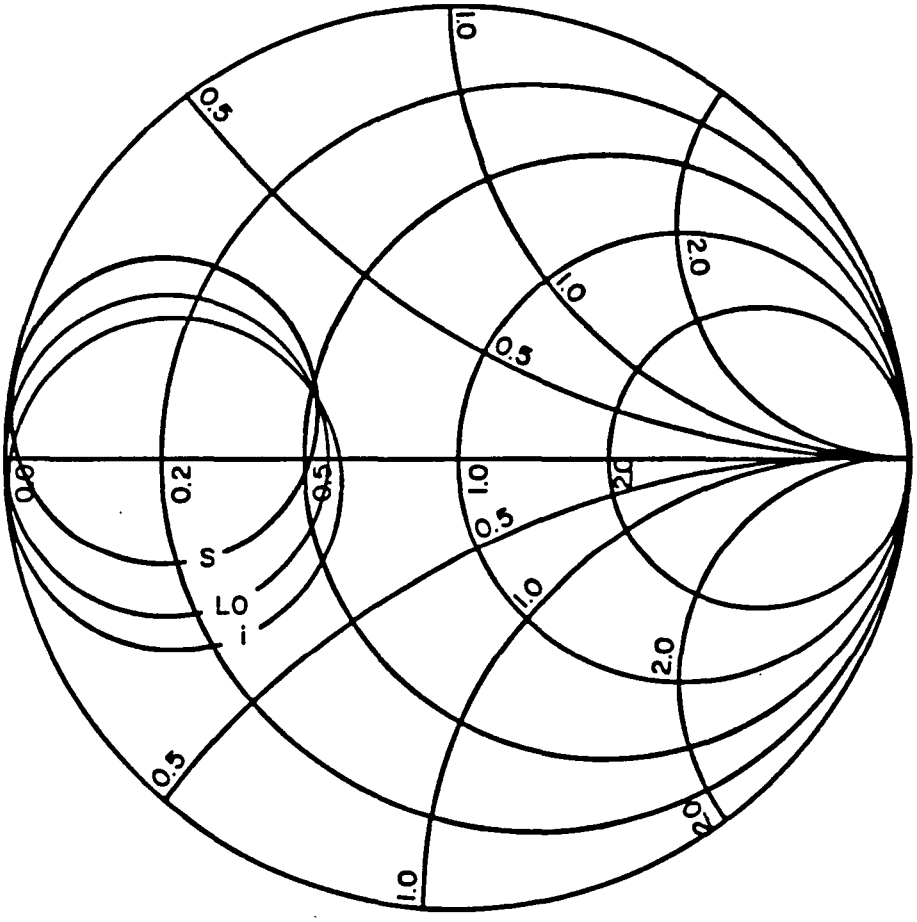

Fig.4-17

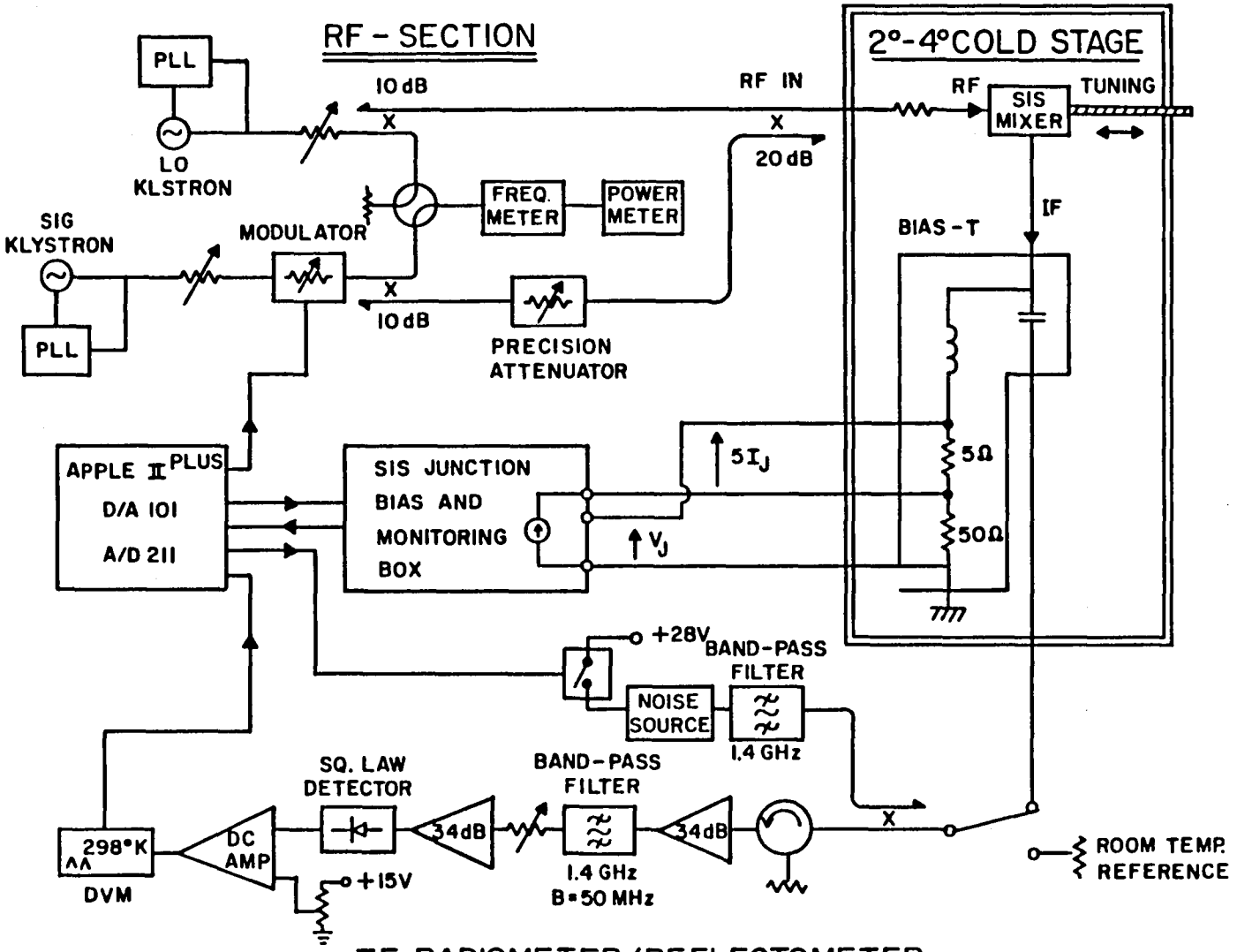

IF RADIOMETER/REFLECTOMETER

Fig. 5-1

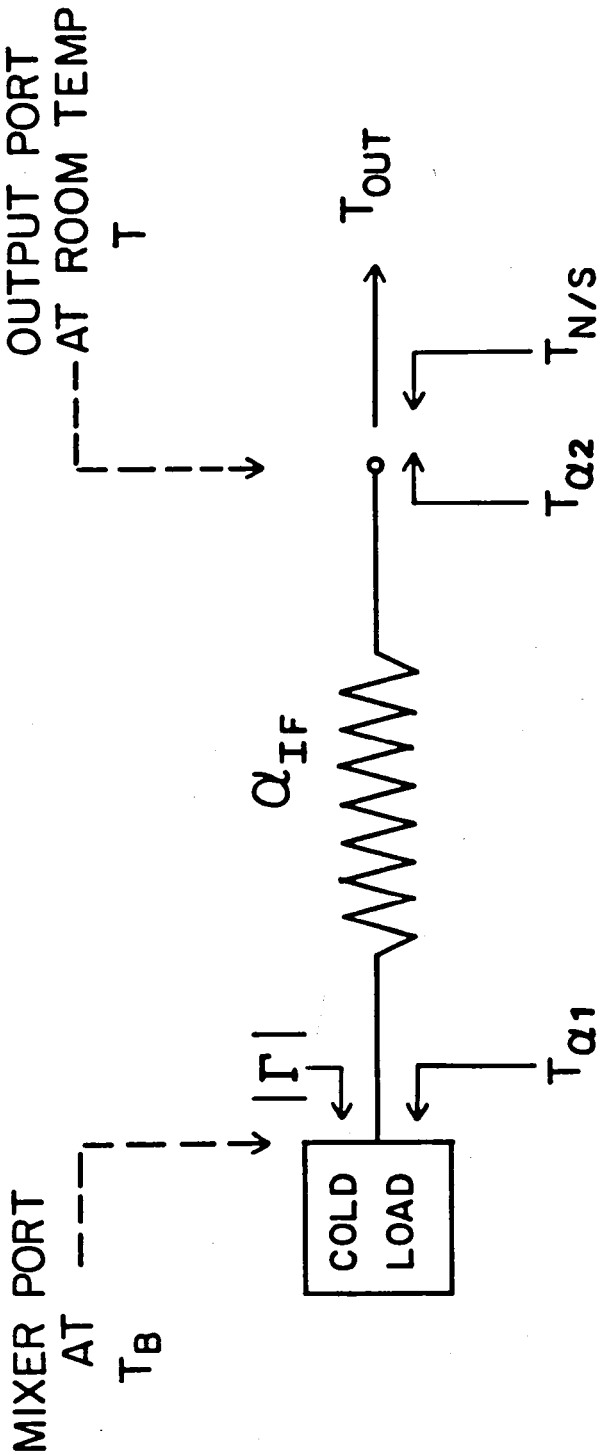
OUTPUT PORT
AT ROOM TEMP
T
MIXER PORT
AT
T_B
COLD
LOAD
$|\Gamma|$
α_{IF}
T_{OUT}
$T_{\alpha 1}$
$T_{\alpha 2}$
$T_{N/S}$

Fig. 5-2

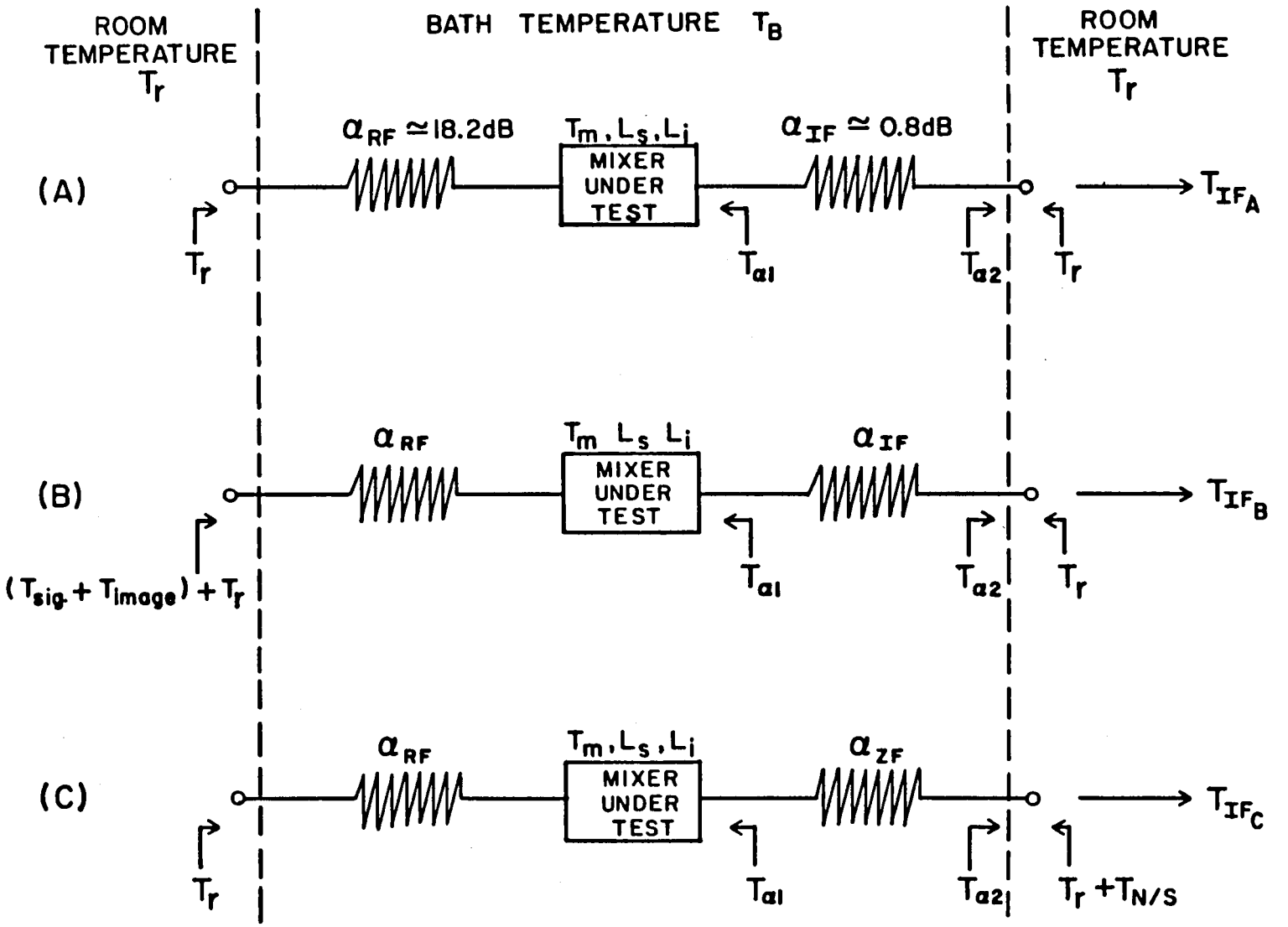
ROOM TEMPERATURE T_r
BATH TEMPERATURE T_B
ROOM TEMPERATURE T_r
(A)
$\alpha_{RF} \simeq 18.2dB$
T_m, L_s, L_i
MIXER UNDER TEST
$\alpha_{IF} \simeq 0.8dB$
T_{IF_A}
T_r
T_{a1}
T_{a2}
T_r
(B)
α_{RF}
T_m L_s L_i
MIXER UNDER TEST
α_{IF}
T_{IF_B}
$(T_{sig} + T_{Image}) + T_r$
T_{a1}
T_{a2}
T_r
(C)
α_{RF}
T_m, L_s, L_i
MIXER UNDER TEST
α_{ZF}
T_{IF_C}
T_r
T_{a1}
T_{a2}
$T_r + T_{N/S}$

Fig. 6-1

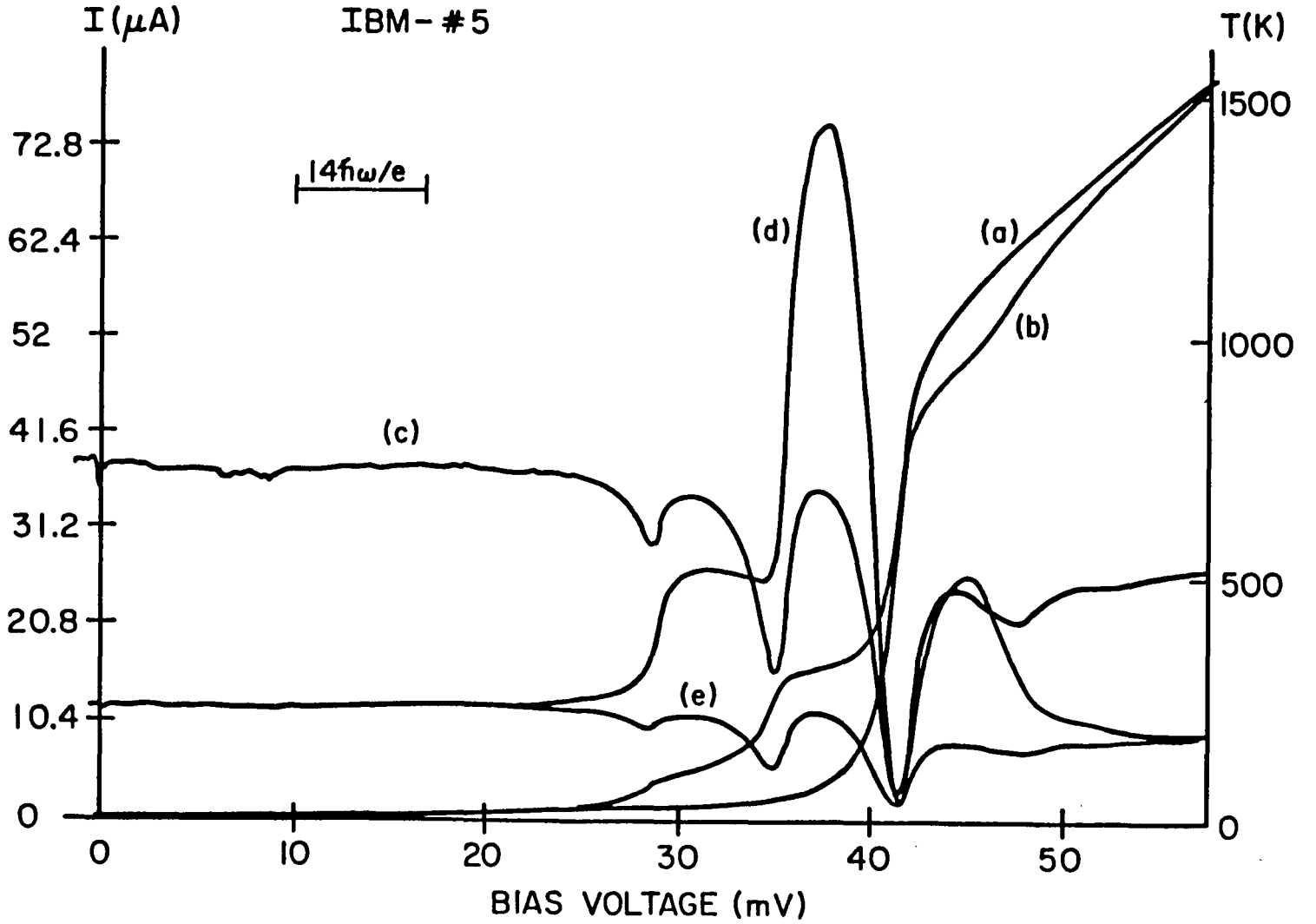
I(μA)
IBM-#5
T(K)
72.8
62.4
52
41.6
31.2
20.8
10.4
0
14ħω/e
(a)
(b)
(c)
(d)
(e)
1500
1000
500
0
0
10
20
30
40
50
BIAS VOLTAGE (mV)

Fig. 6-2

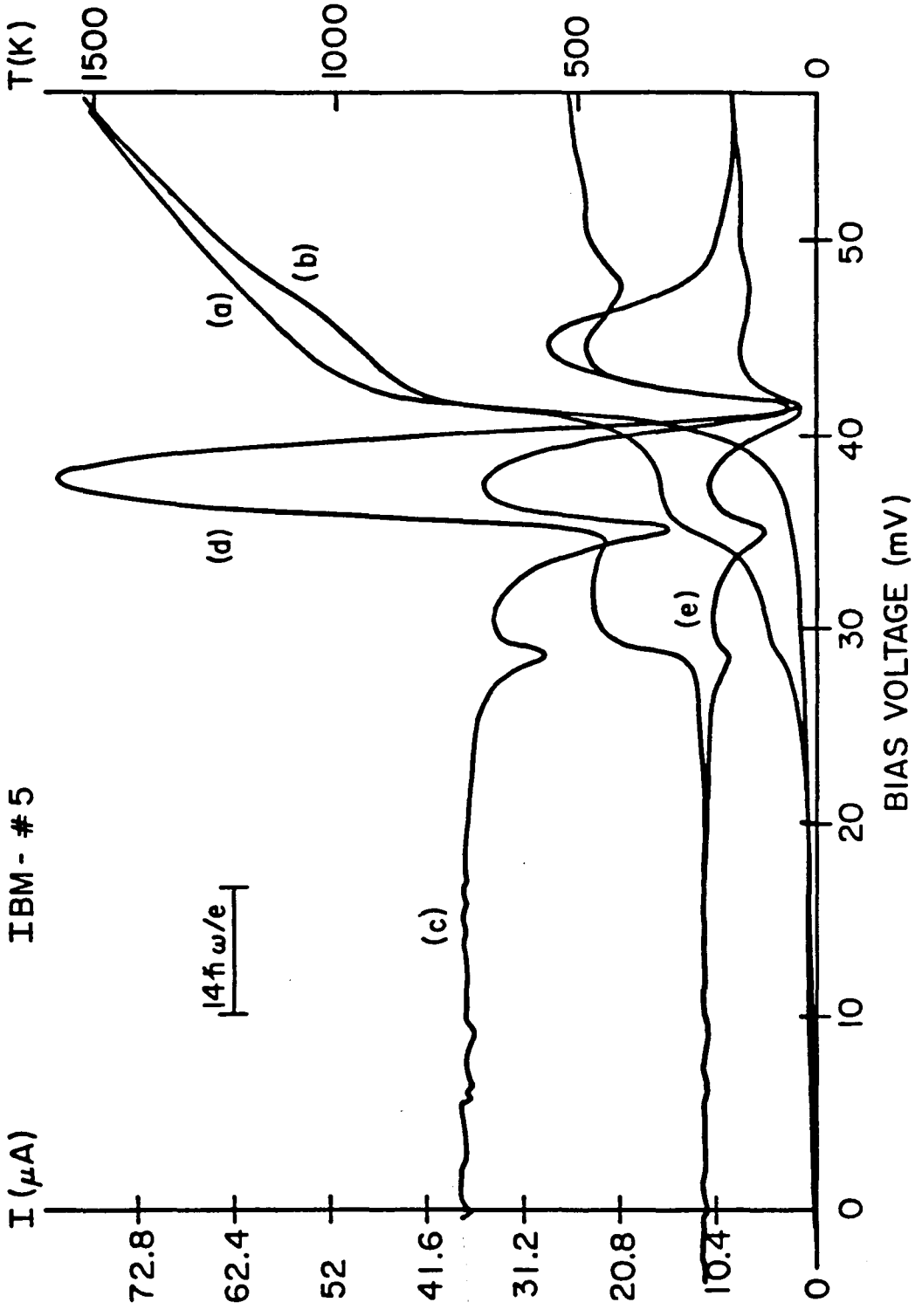
IBM - #5
T(K)
1500
1000
500
0
I (μA)
72.8
62.4
52
41.6
31.2
20.8
10.4
0
(a)
(b)
(c)
(d)
(e)
4ħω/e
0
10
20
30
40
50
BIAS VOLTAGE (mV)

Fig. 6-3

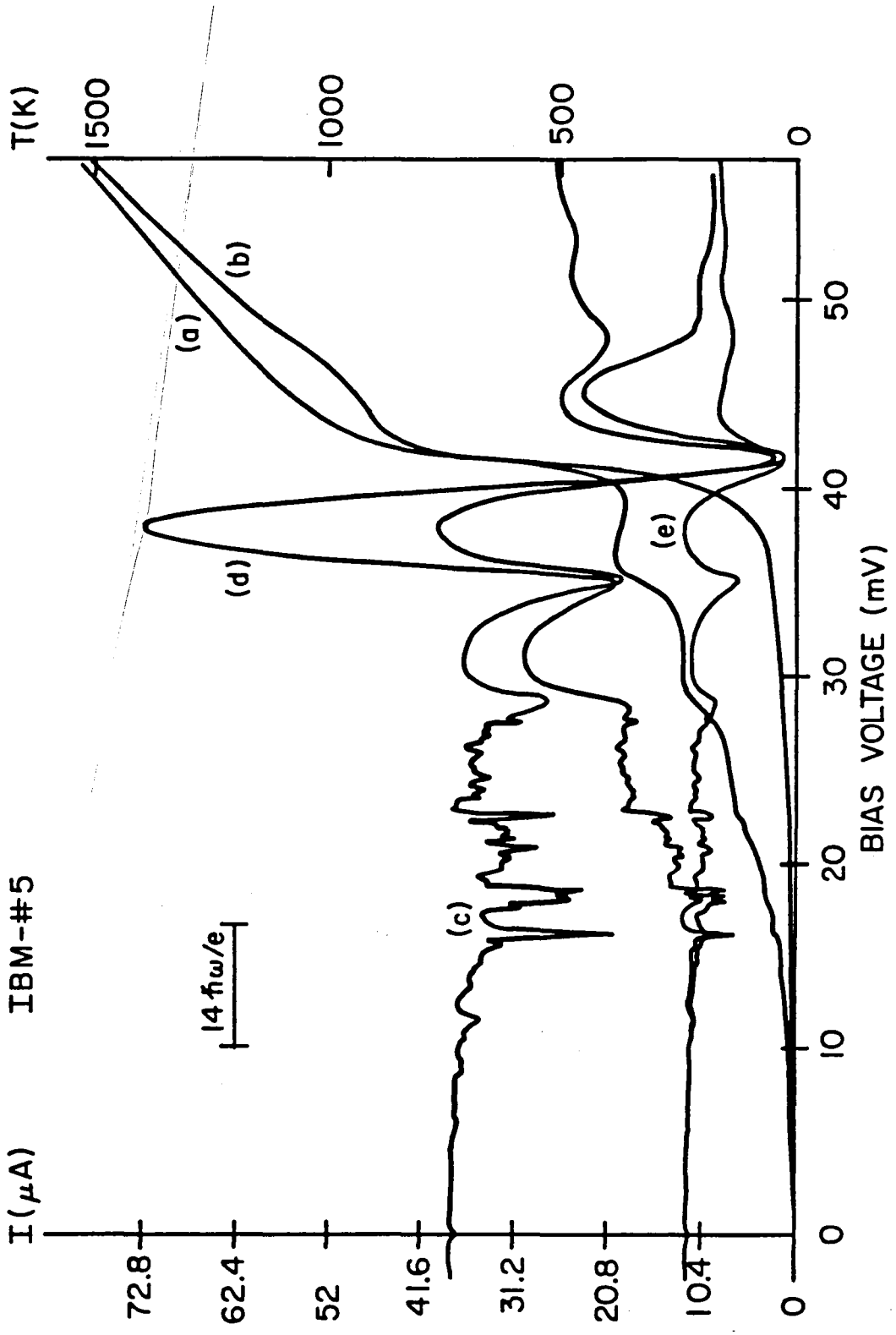
T(K)
1500
1000
500
0
I(μA)
72.8
62.4
52
41.6
31.2
20.8
10.4
0
IBM-#5
14ħω/e
(a)
(b)
(c)
(d)
(e)
0
10
20
30
40
50
BIAS VOLTAGE (mV)

Fig. 6-4

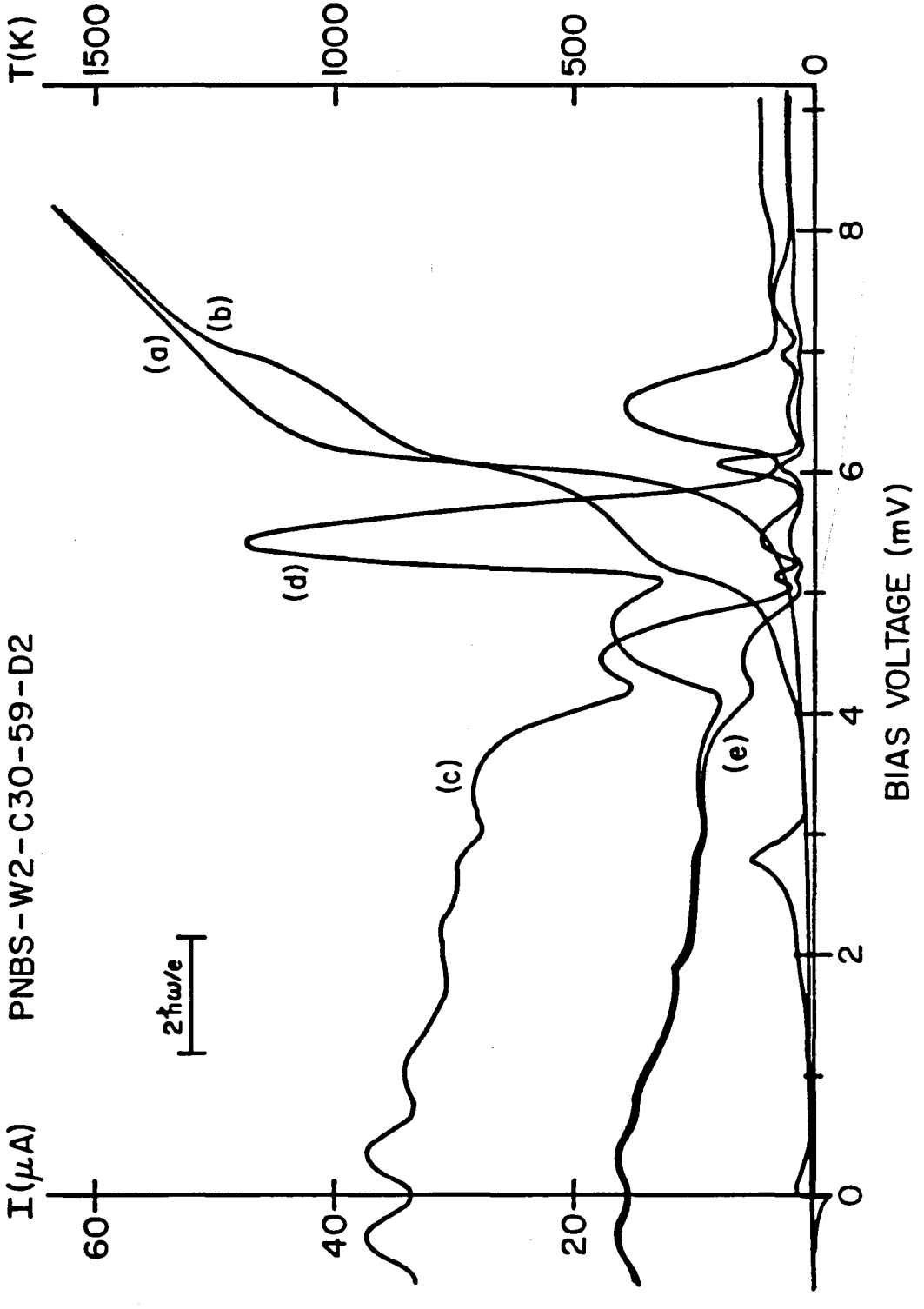
PNBS-W2-C30-59-D2
I(μA)
T(K)
60
40
20
0
1500
1000
500
0
2ħω/e
(a)
(b)
(c)
(d)
(e)
0
2
4
6
8
BIAS VOLTAGE (mV)

Fig. 6-5

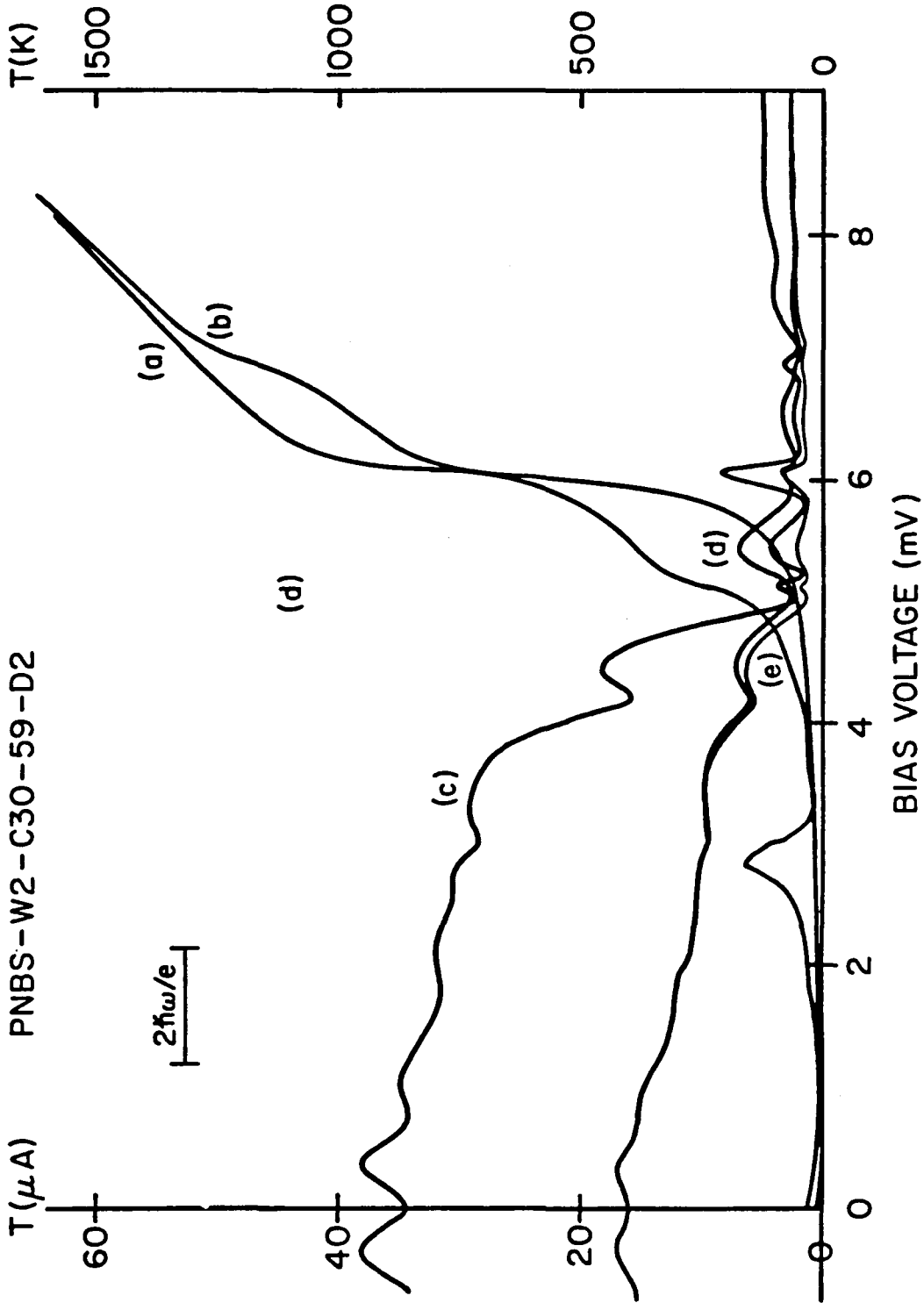
T(K)
1500
1000
500
0
T(μA)
60
40
20
0
PNBS-W2-C30-59-D2
2ħω/e
(a)
(b)
(c)
(d)
(d)
(e)
0
2
4
6
8
BIAS VOLTAGE (mV)

Fig. 6-6

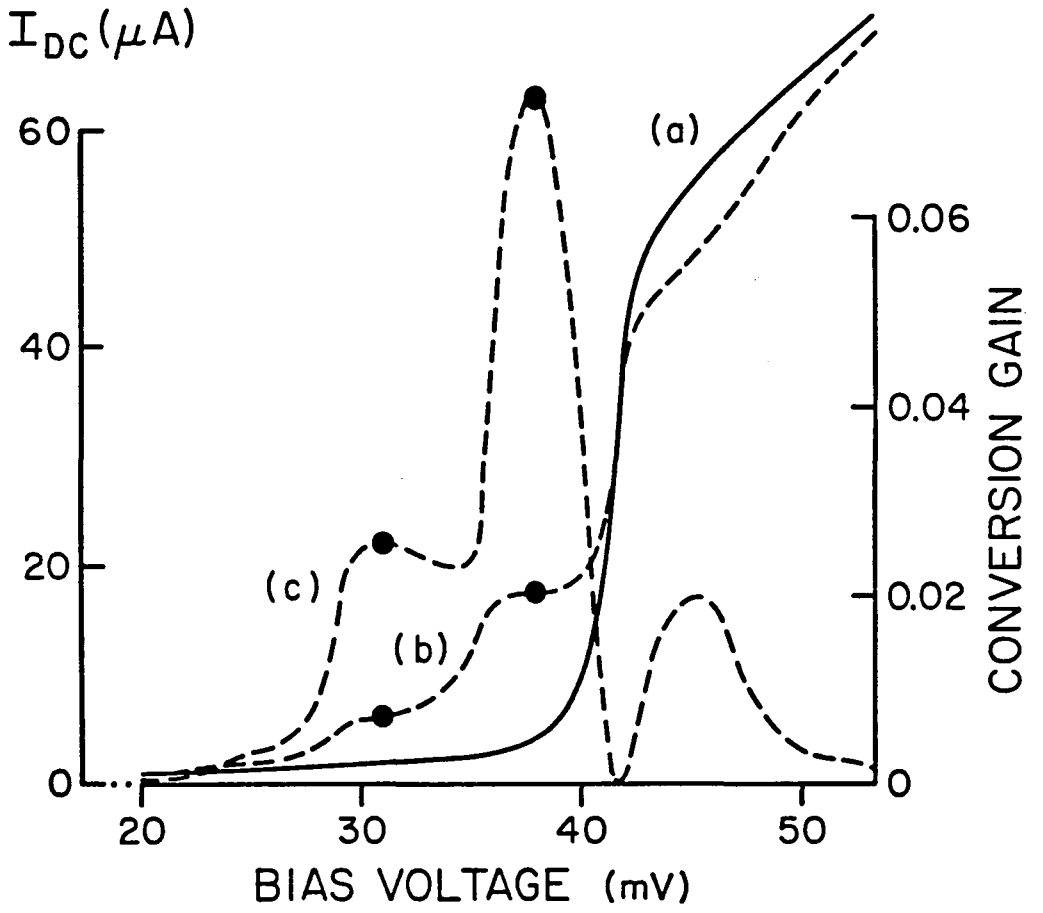
$I_{DC}(\mu A)$
60
40
20
0
(a)
(b)
(c)
0.06
0.04
0.02
0
CONVERSION GAIN
20
30
40
50
BIAS VOLTAGE (mV)

Fig. 6-7

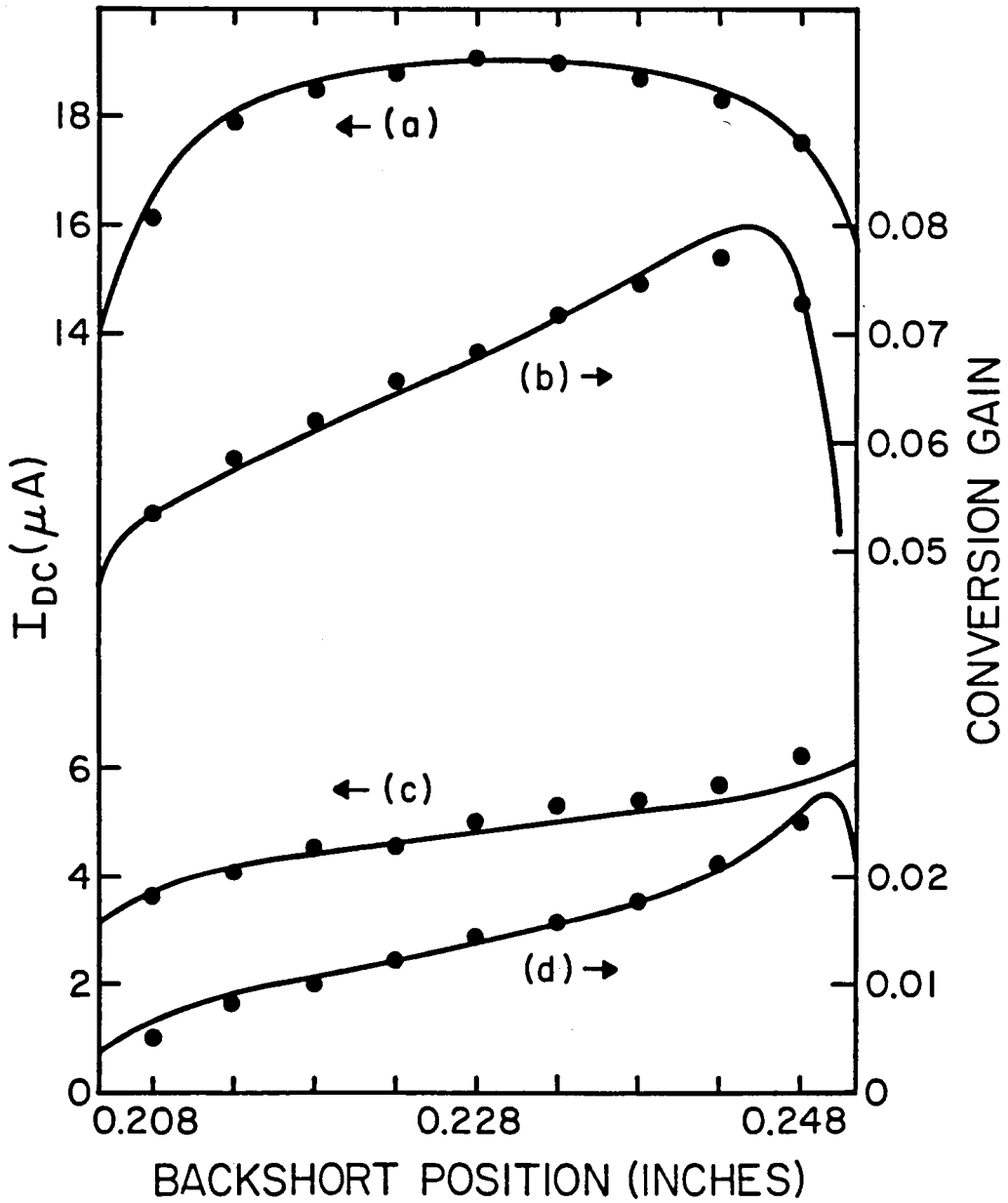
18
16
14
6
4
2
0
0.08
0.07
0.06
0.05
0.02
0.01
0
0.208
0.228
0.248
(a)
(b)
(c)
(d)
$I_{DC}(\mu A)$
CONVERSION GAIN
BACKSHORT POSITION (INCHES)

Fig. 6-8

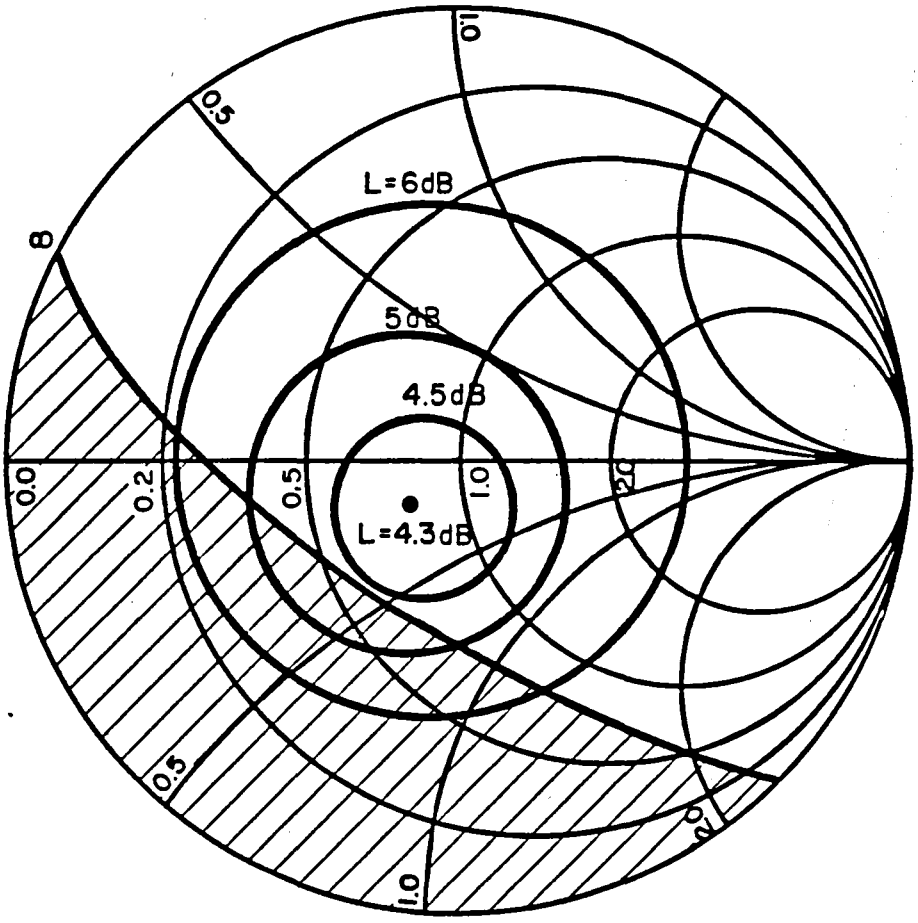

Fig. 6-9

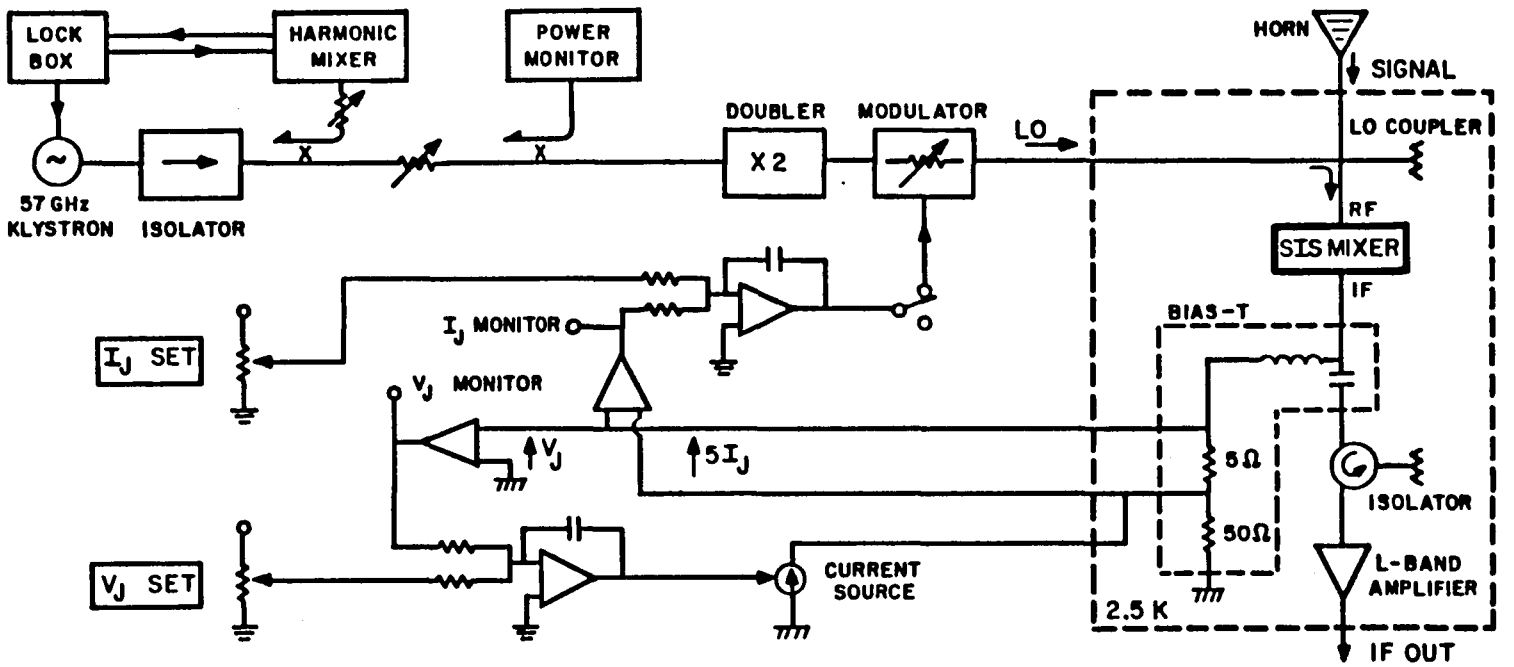
LOCK BOX
HARMONIC MIXER
POWER MONITOR
57 GHz KLYSTRON
ISOLATOR
DOUBLER
X2
MODULATOR
LO
HORN
SIGNAL
LO COUPLER
RF
SIS MIXER
IF
BIAS-T
I_J SET
I_J MONITOR
V_J MONITOR
V_J
$5I_J$
5Ω
50Ω
ISOLATOR
L-BAND AMPLIFIER
V_J SET
CURRENT SOURCE
2.5 K
IF OUT

Fig. 7-1

115 GHZ SIS RECEIVER

$T_{SSB} = 83K$

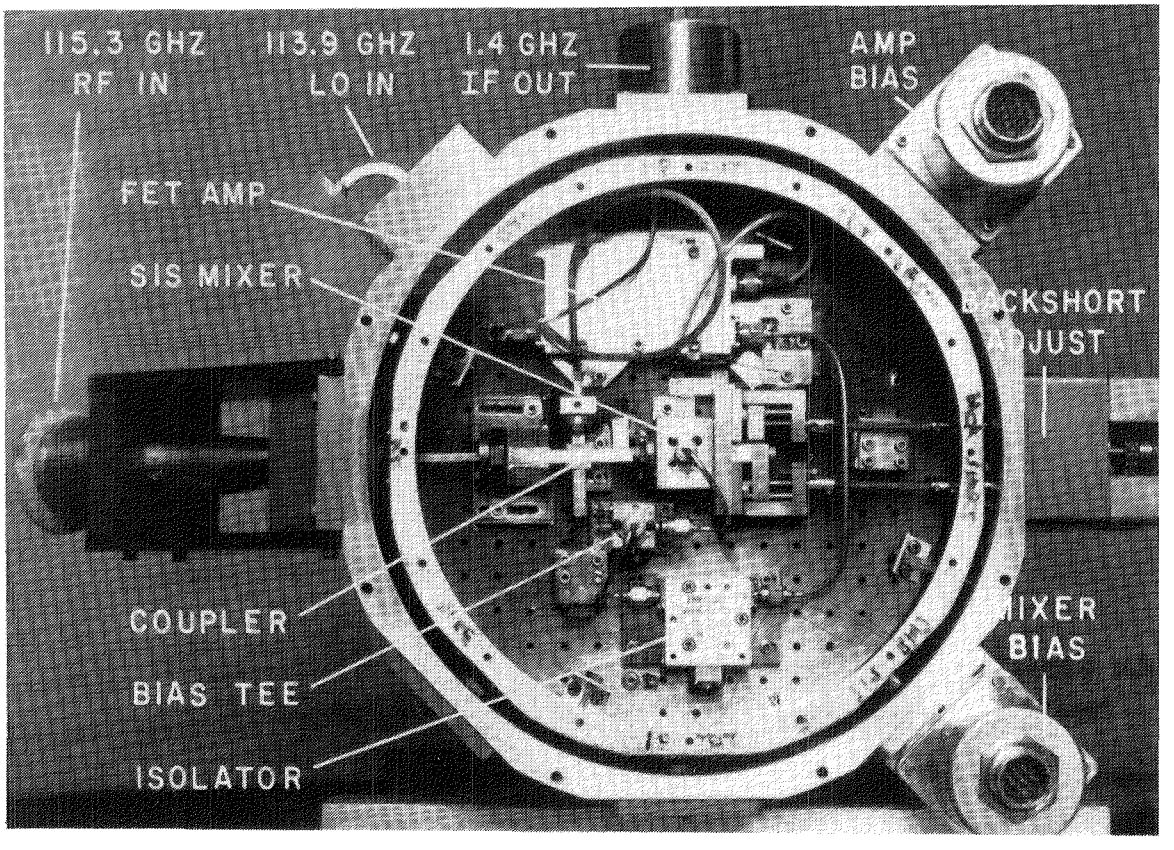

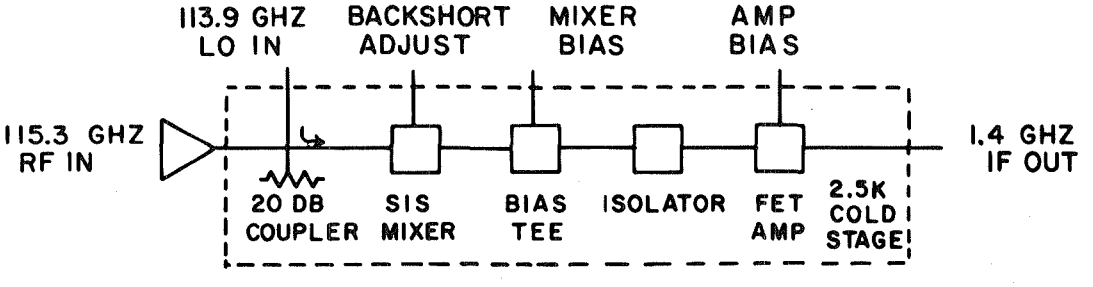

Fig. 7-2

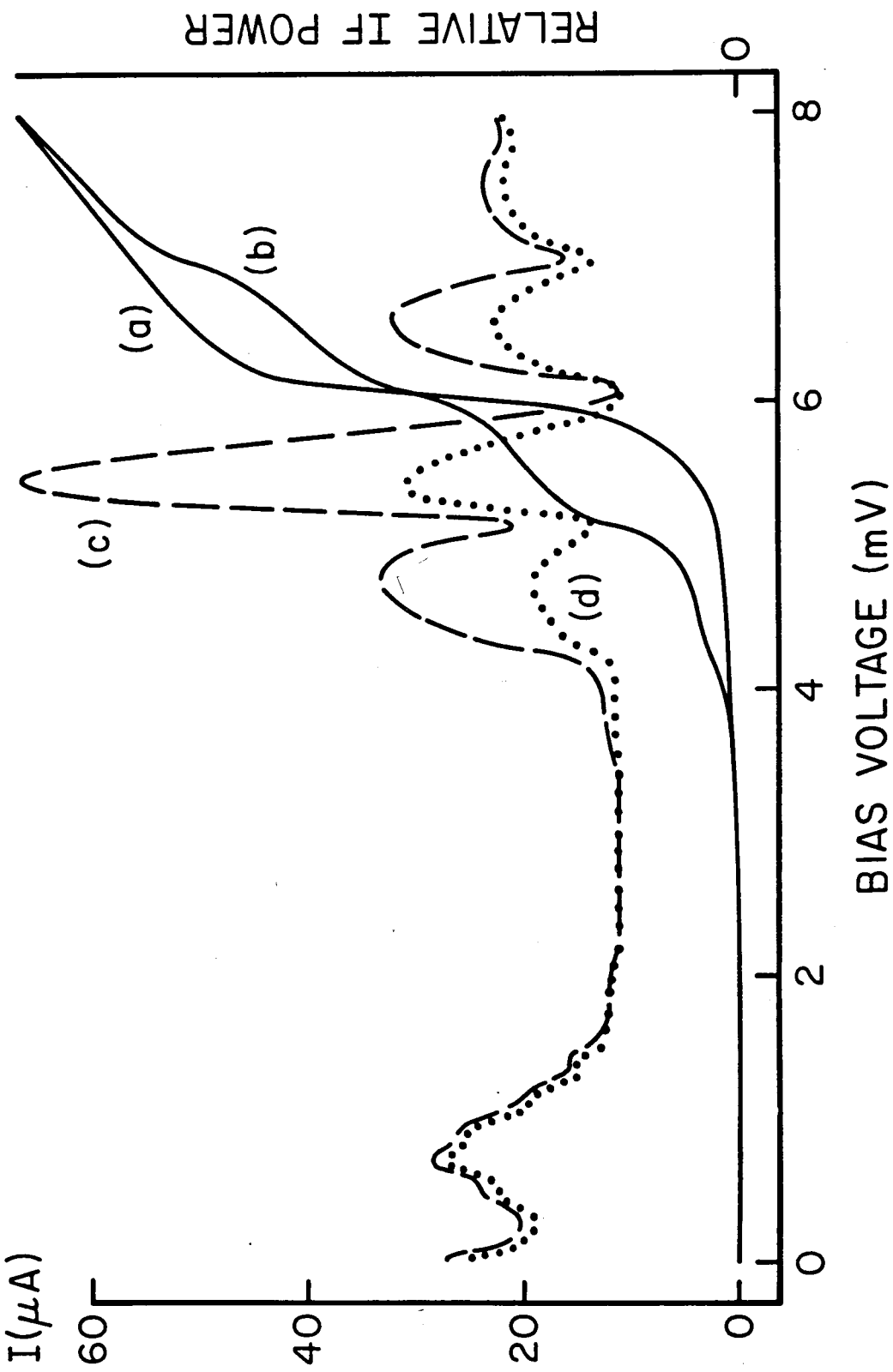

Fig. 7-3

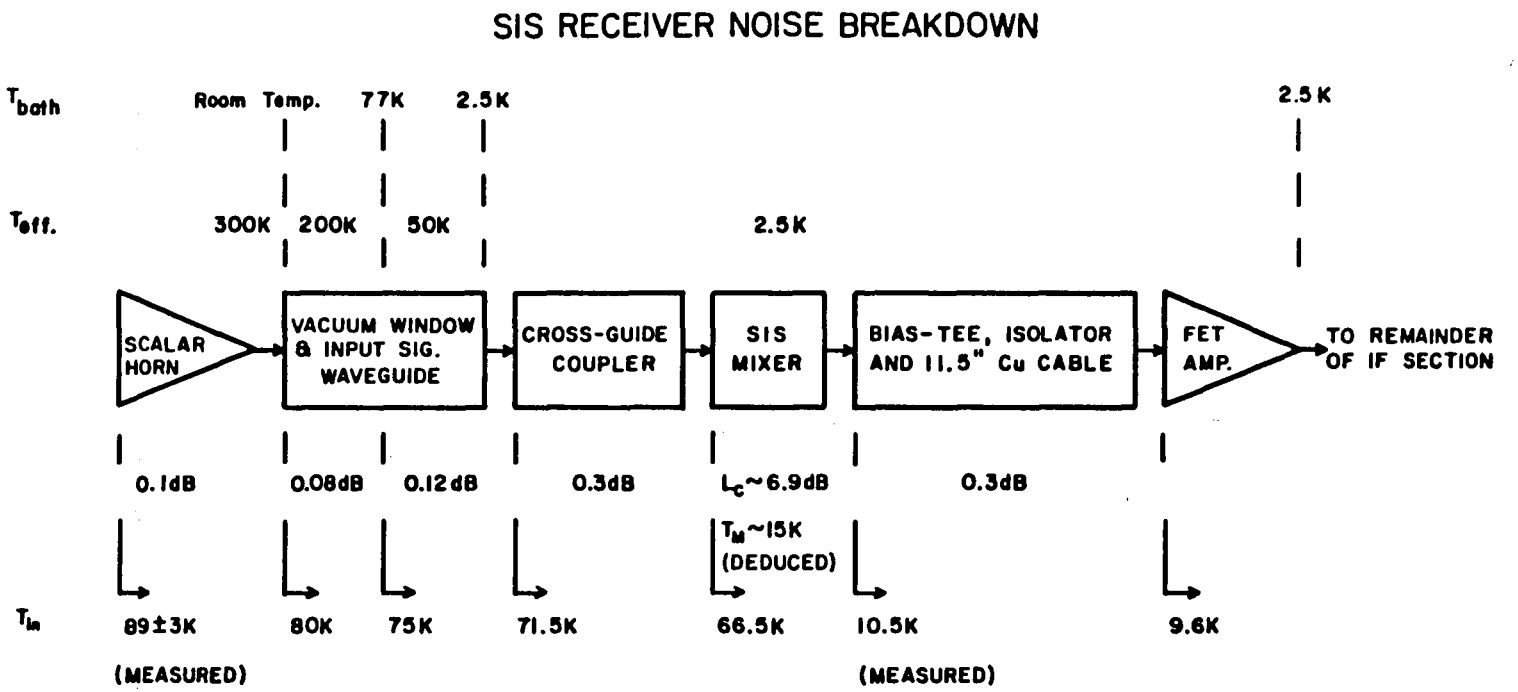
SIS RECEIVER NOISE BREAKDOWN
T_{bath}
Room Temp.
77K
2.5K
2.5K
$T_{eff.}$
300K
200K
50K
2.5K
SCALAR HORN
VACUUM WINDOW & INPUT SIG. WAVEGUIDE
CROSS-GUIDE COUPLER
SIS MIXER
BIAS-TEE, ISOLATOR AND 11.5" Cu CABLE
FET AMP.
TO REMAINDER OF IF SECTION
0.1dB
0.08dB
0.12dB
0.3dB
L_c~6.9dB
0.3dB
T_M~15K (DEDUCED)
T_{in}
89±3K
80K
75K
71.5K
66.5K
10.5K
9.6K
(MEASURED)
(MEASURED)

Fig. 7-4

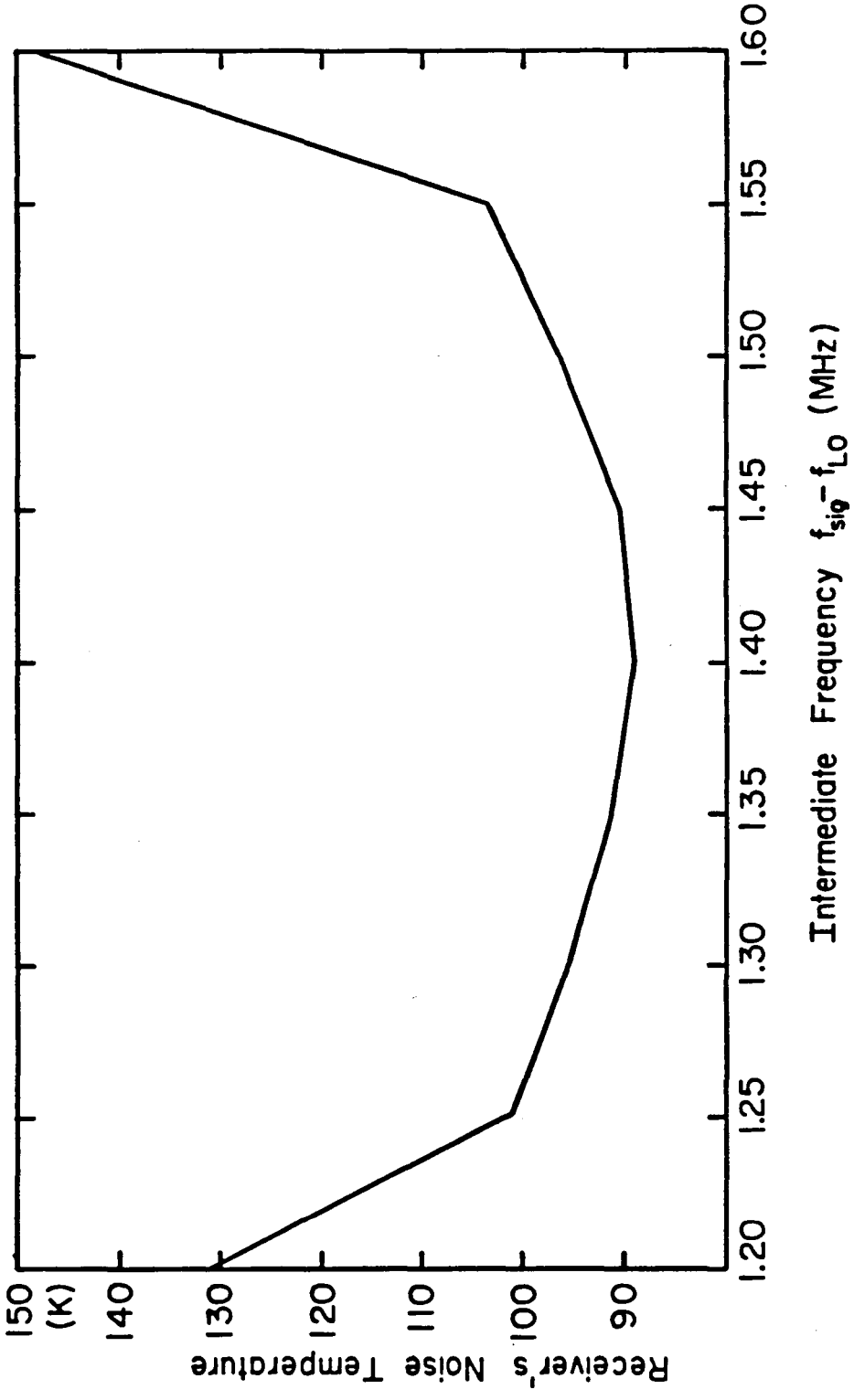
150
(K)
140
130
120
110
100
90
Receiver's Noise Temperature
1.20
1.25
1.30
1.35
1.40
1.45
1.50
1.55
1.60
Intermediate Frequency $f_{sig} - f_{LO}$ (MHz)

Fig. 7-5

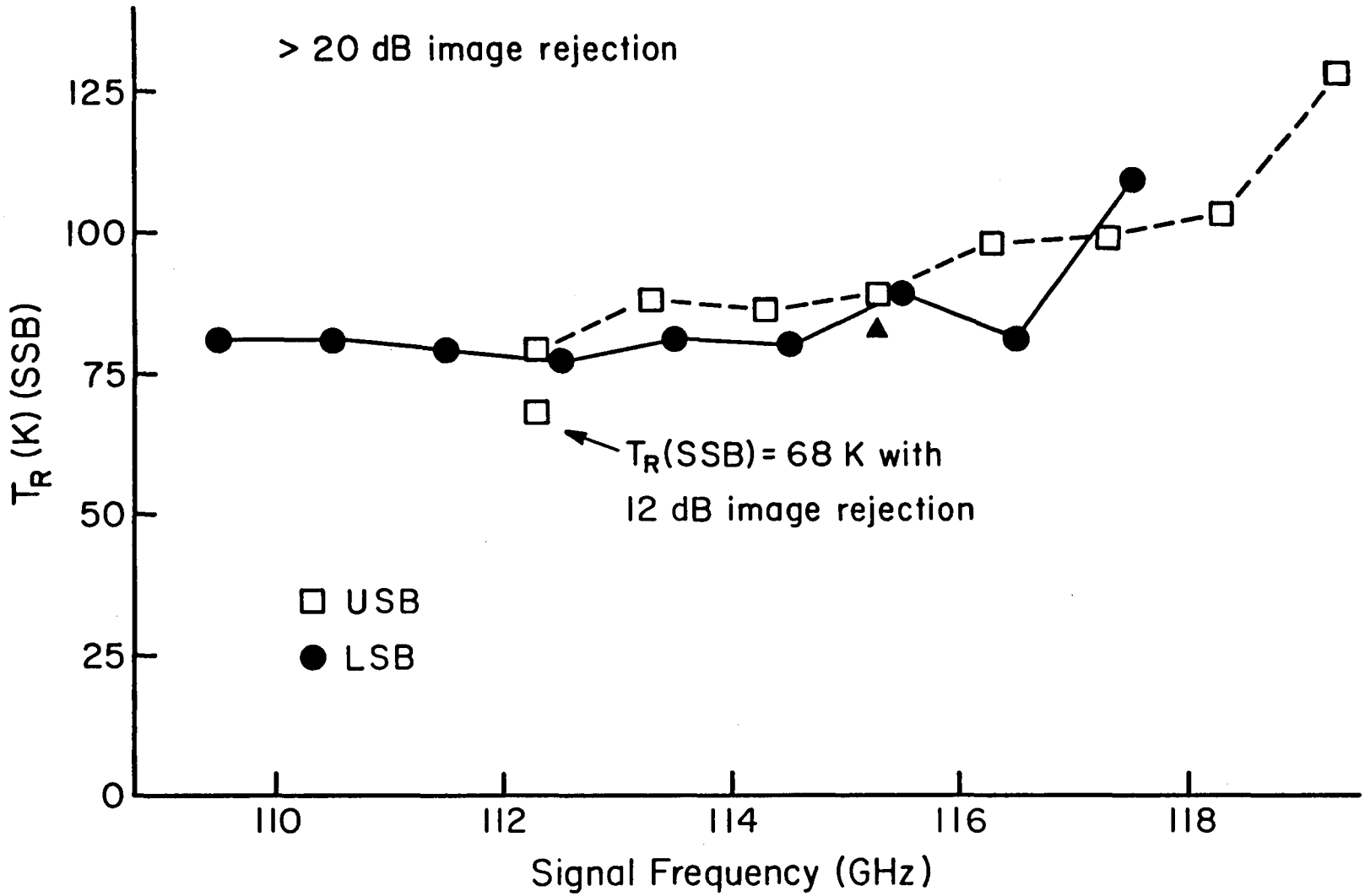
> 20 dB image rejection
125
100
75
50
25
0
T_R (K) (SSB)
T_R(SSB) = 68 K with
12 dB image rejection
USB
LSB
110
112
114
116
118
Signal Frequency (GHz)

Fig. 7-6

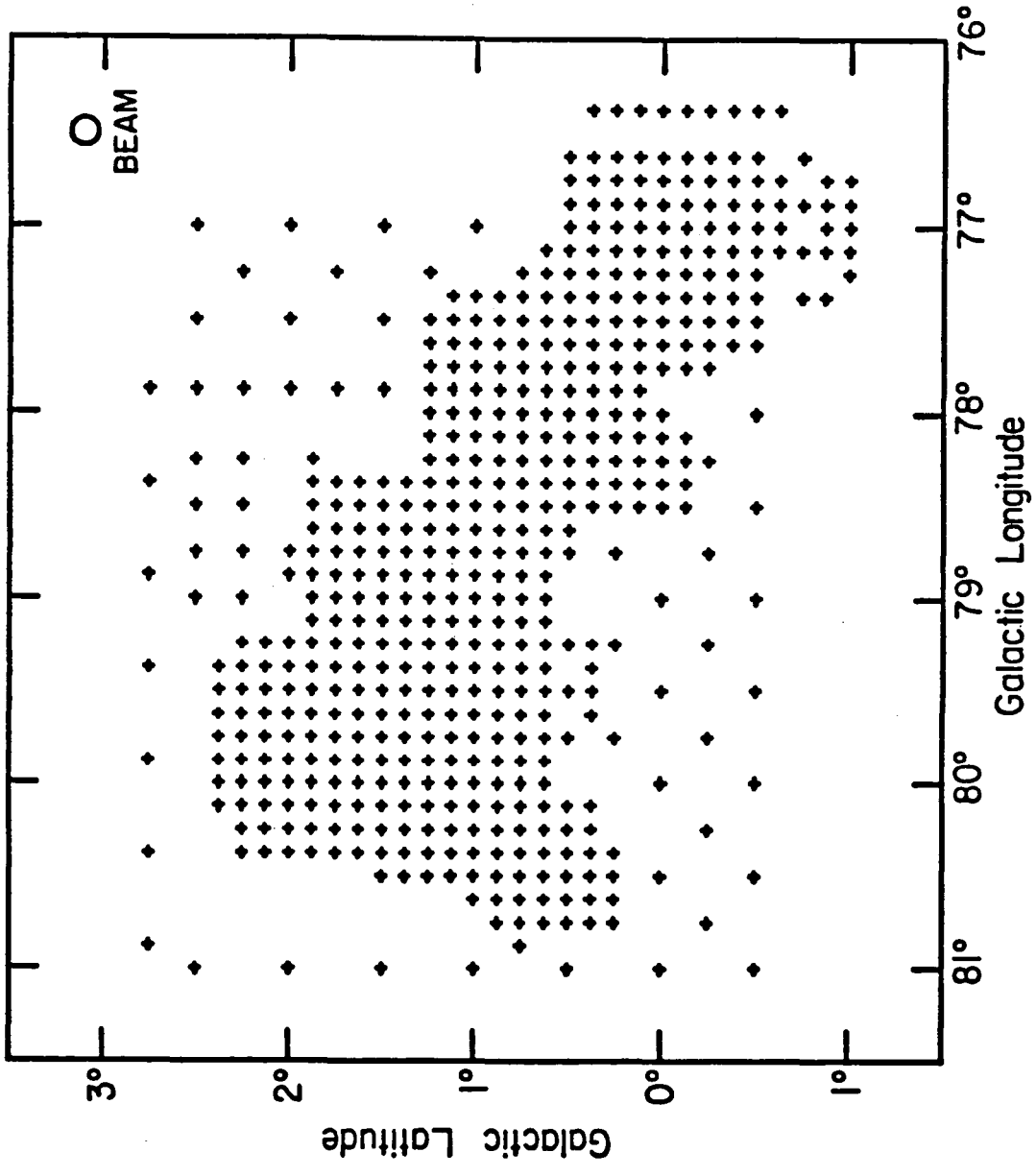
O
BEAM
3°
2°
1°
0°
1°
Galactic Latitude
81°
80°
79°
78°
77°
76°
Galactic Longitude

Fig. 8-1

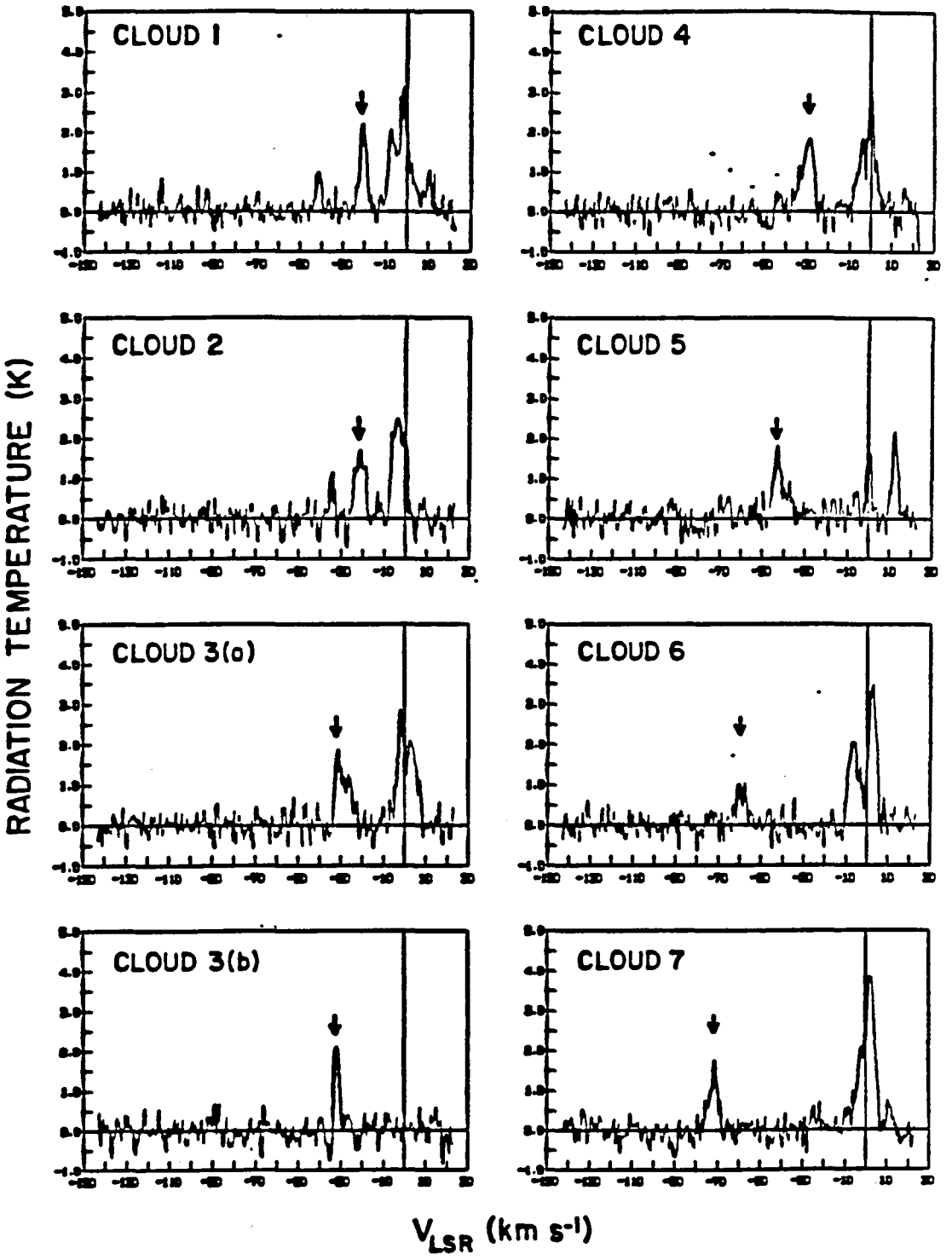
CLOUD 1
CLOUD 4
CLOUD 2
CLOUD 5
CLOUD 3(a)
CLOUD 6
CLOUD 3(b)
CLOUD 7
RADIATION TEMPERATURE (K)
V_{LSR} (km s^{-1})

Fig. 8-2

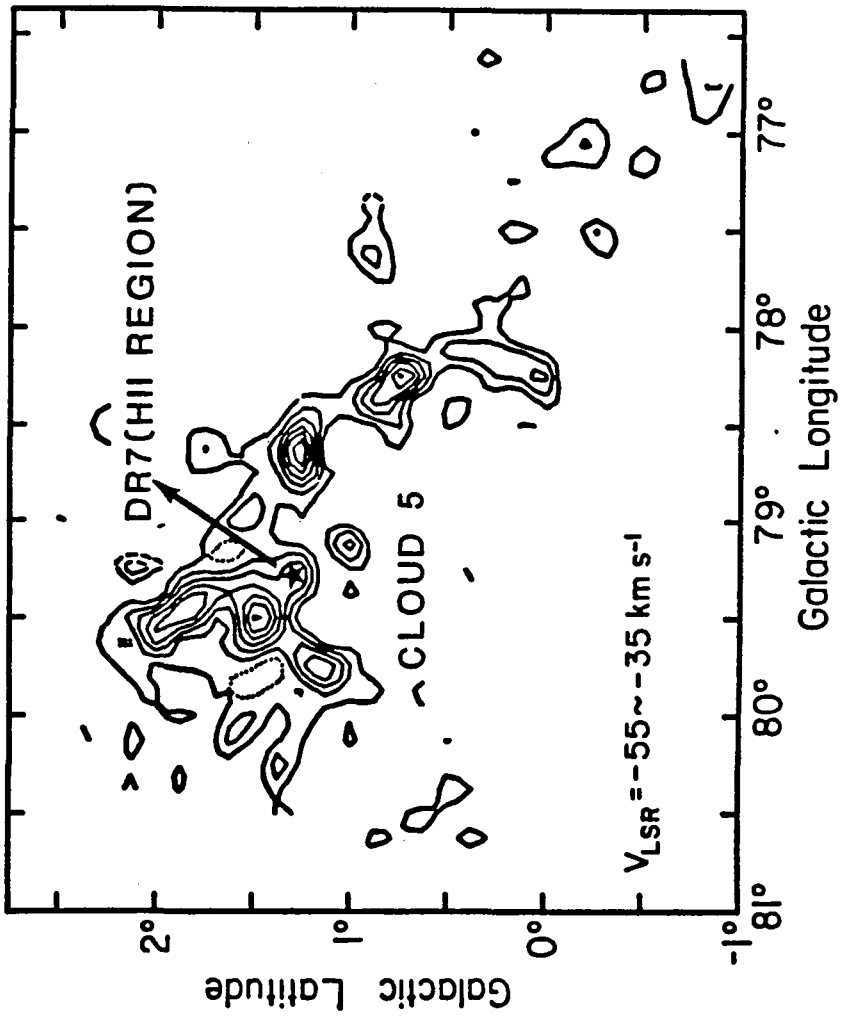
DR7(HII REGION)
CLOUD 5
V_{LSR}=-55~-35 km s^{-1}
Galactic Longitude
Galactic Latitude
81°
80°
79°
78°
77°
2°
1°
0°
-1°

Fig. 8-3

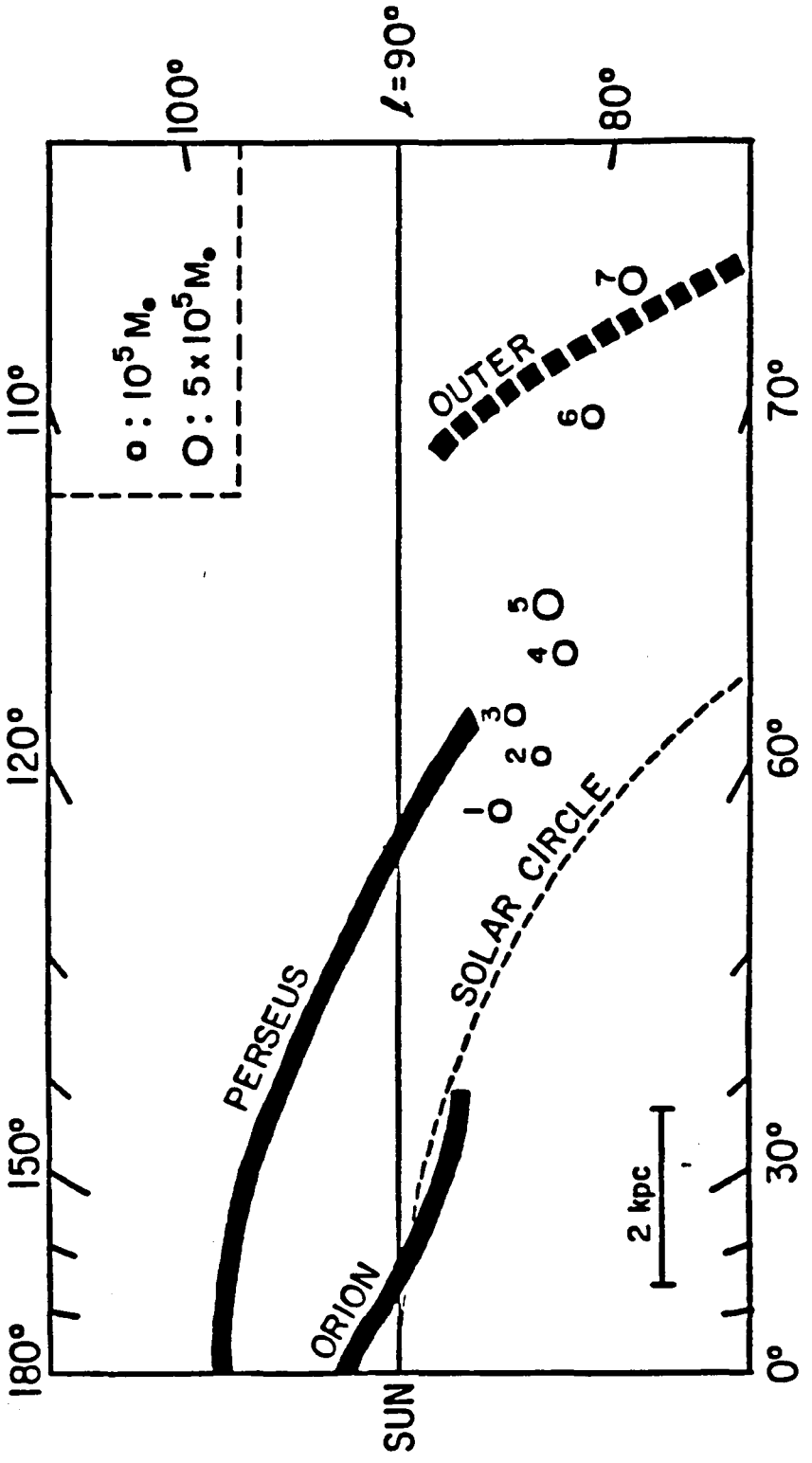
180°
150°
120°
110°
100°
ℓ=90°
80°
70°
60°
30°
0°
SUN
o : 10^5 M☉
O : 5x10^5 M☉
OUTER
PERSEUS
ORION
SOLAR CIRCLE
2 kpc
1
2
3
4
5
6
7

Fig. 8-4

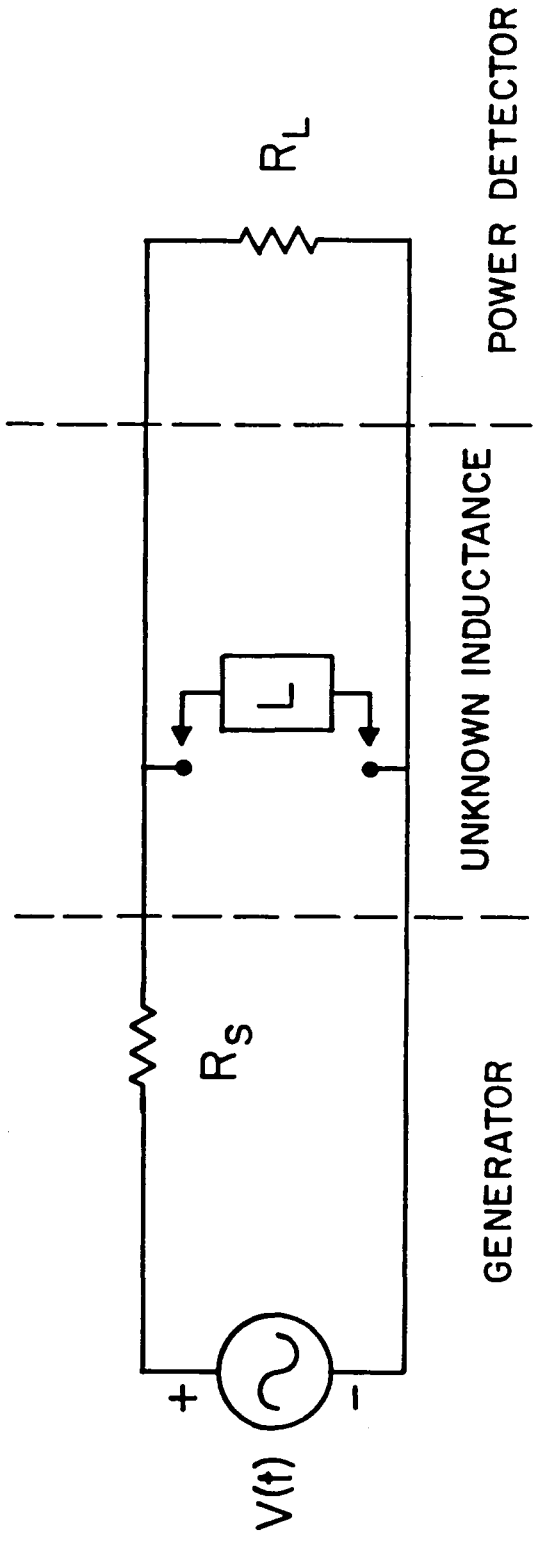

Fig. AI-1

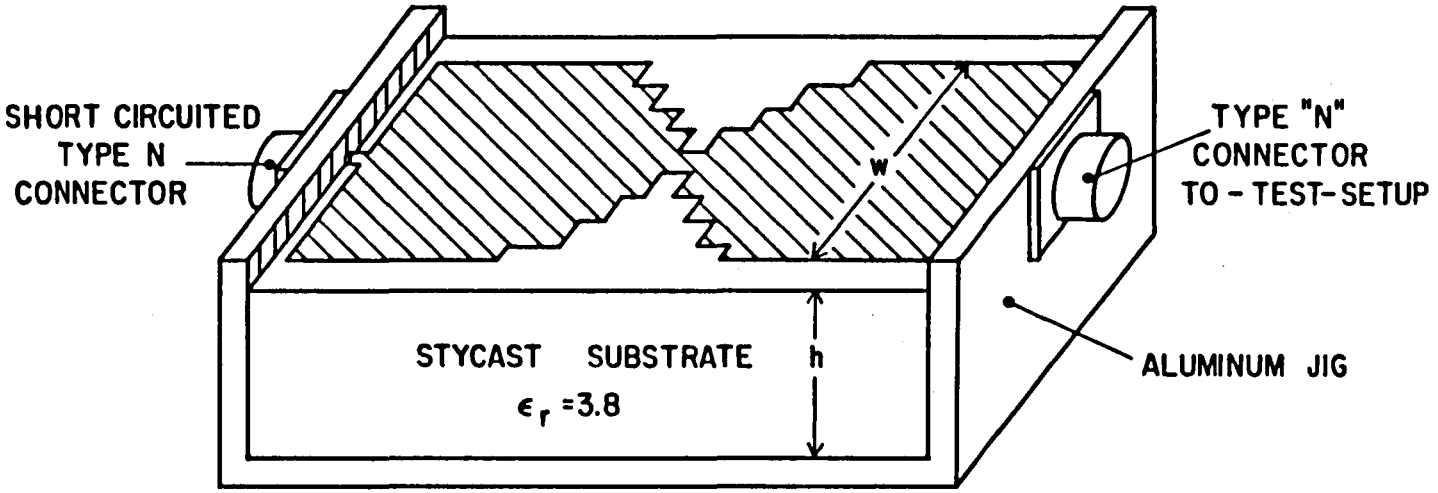
SHORT CIRCUITED
TYPE N
CONNECTOR
TYPE "N"
CONNECTOR
TO - TEST-SETUP
w
h
STYCAST SUBSTRATE
ϵ_r =3.8
ALUMINUM JIG

Fig. AI-2

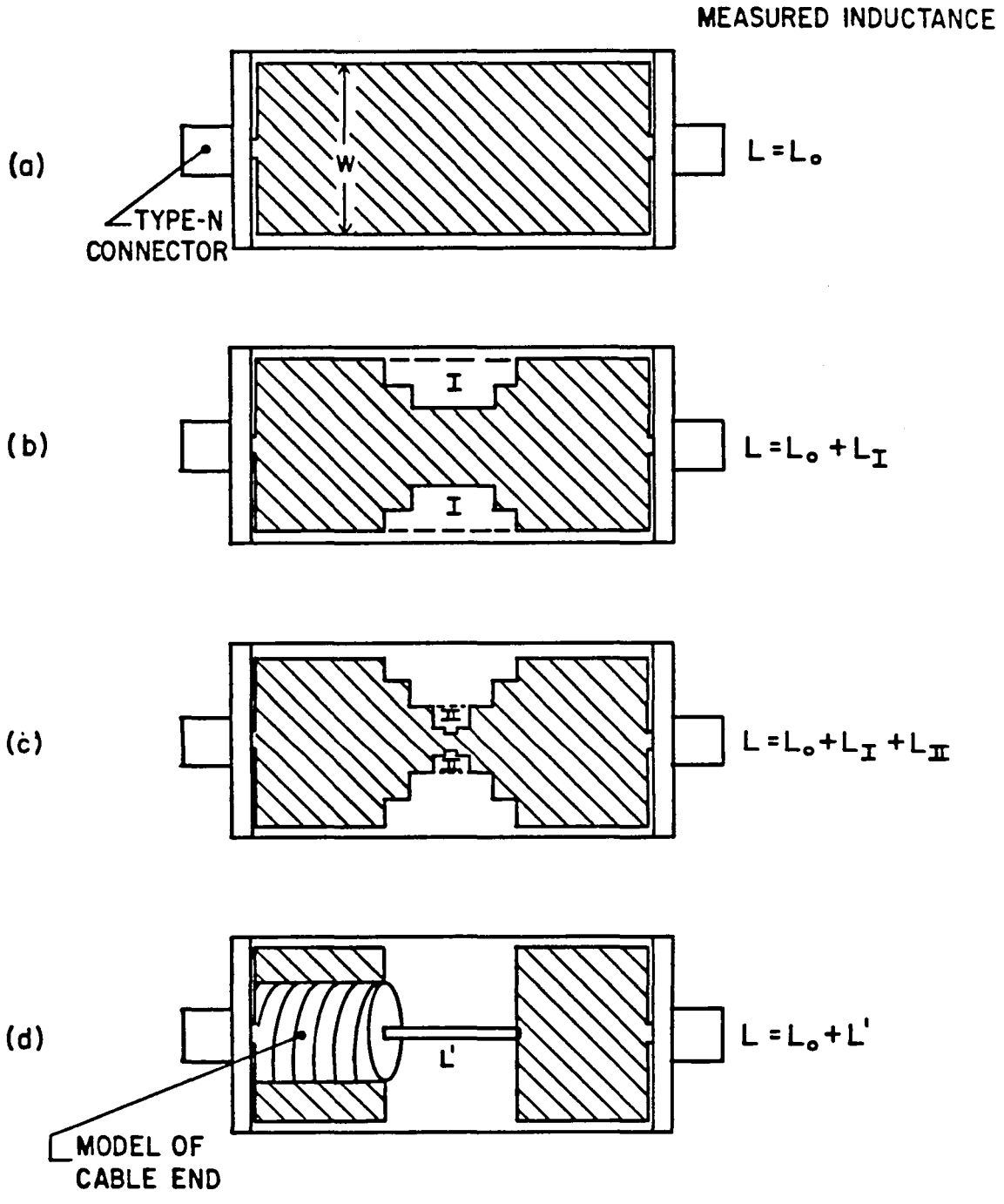
MEASURED INDUCTANCE
(a)
W
TYPE-N
CONNECTOR
L = L₀
(b)
I
I
L = L₀ + L_I
(c)
II
II
L = L₀ + L_I + L_II
(d)
L'
L = L₀ + L'
MODEL OF
CABLE END

Fig. AI-3

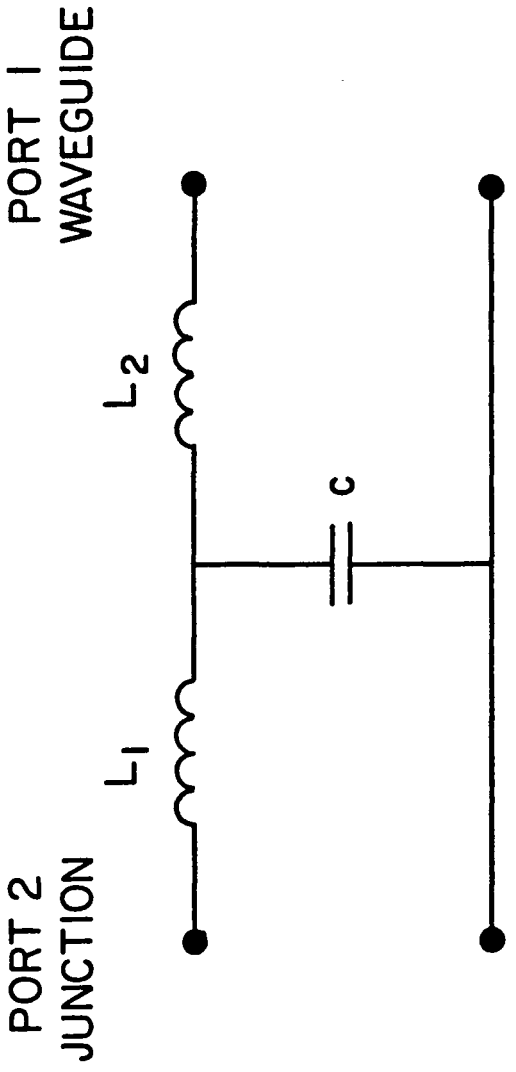

Fig. AII-1

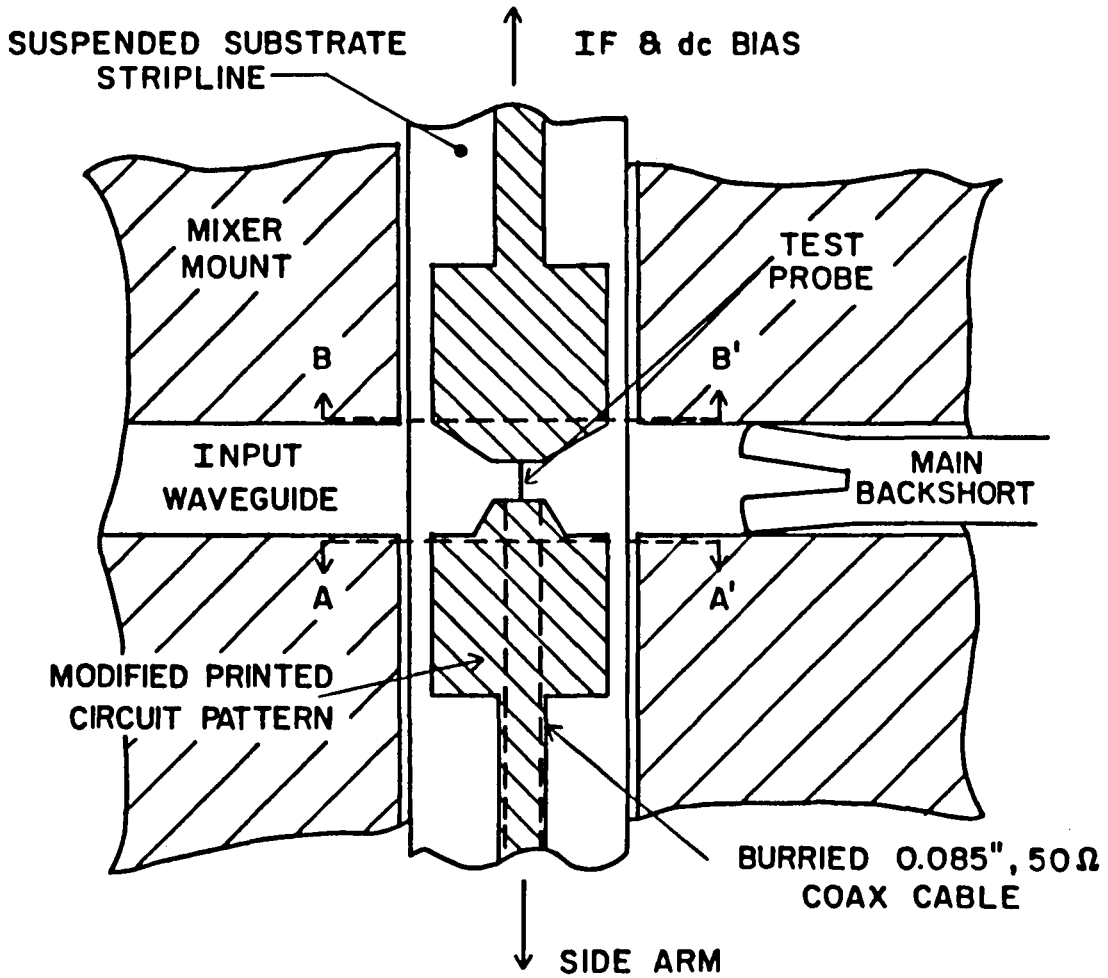
SUSPENDED SUBSTRATE
STRIPLINE
IF & dc BIAS
MIXER
MOUNT
TEST
PROBE
B
B'
INPUT
WAVEGUIDE
MAIN
BACKSHORT
A
A'
MODIFIED PRINTED
CIRCUIT PATTERN
BURRIED 0.085", 50Ω
COAX CABLE
SIDE ARM

Fig. AII-2

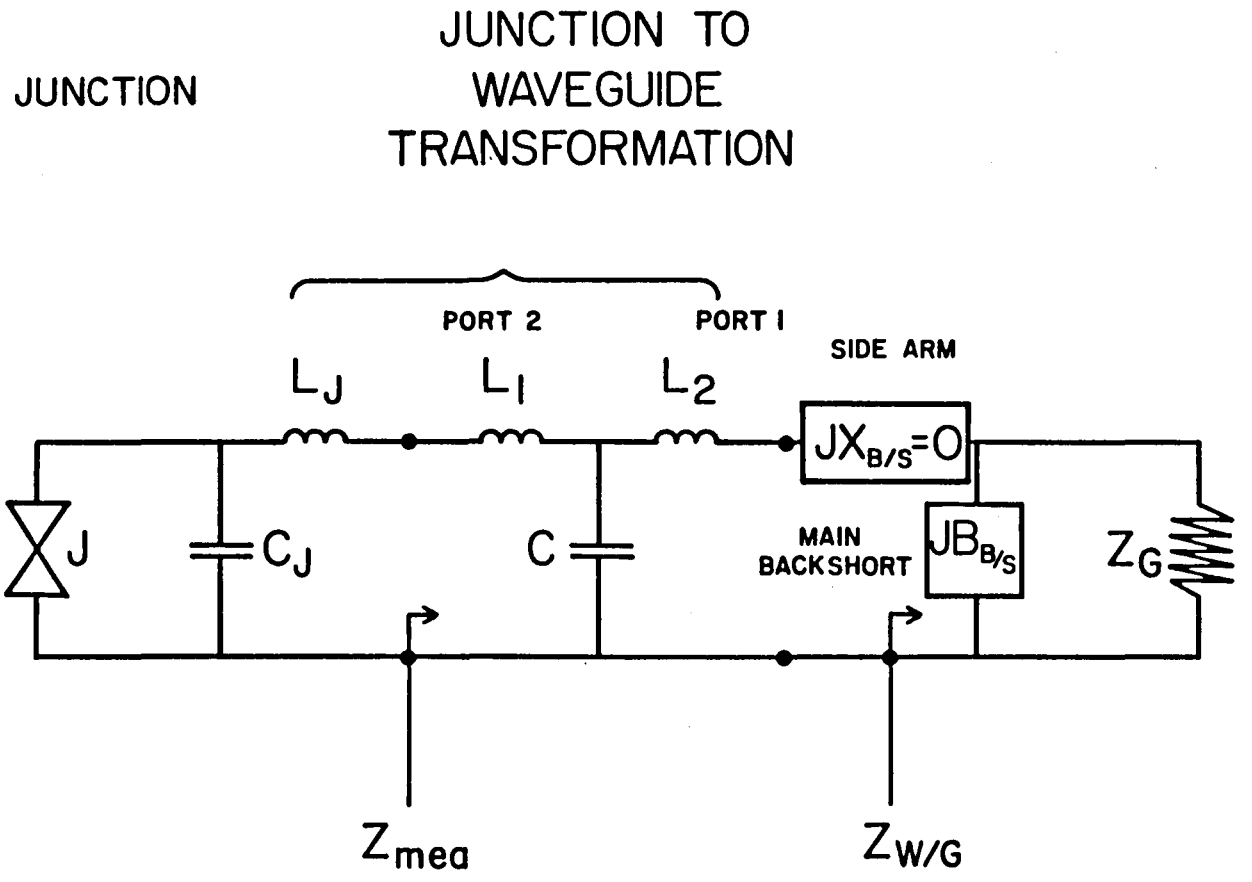
JUNCTION
JUNCTION TO
WAVEGUIDE
TRANSFORMATION
PORT 2
PORT I
SIDE ARM
L_J
L_1
L_2
$JX_{B/S}=0$
J
C_J
C
MAIN
BACKSHORT
$JB_{B/S}$
Z_G
Z_{mea}
$Z_{W/G}$

Fig. AII-3

REFERENCES

1. Ambegaokar, V., and Baratoff, A., Phys. Rev. Lett. 10, 486 (1963)

2. Basavaiah, S., Eldridge, J.M., and Matisoo, J., J. Appl. Phys. 45, 457 (1974)

3. Blundell, R., Hein, H., Gundlach, K.H., and Blum, E.J., Int. J. Infrared and Millimeter Waves. 3, 793 (1982)

4. Blundell, R., Gundlach, K.H., and Blum, E.J., Electron. Lett. 19, 498 (1983)

5. Broom, R.F., Jaggi, R., Mohr, Th.O., Oosenbrug, A., IBM J. Res. Develop. 24, 206 (1980)

6. Chin, G., Ph.D. dissertation, Columbia University, (1978)

7. Cohen, M.H., Falicov, L.M., and Phillips, J.C., Phys. Rev. Lett. 8, 316 (1962)

8. Cohen, R.S., Ph.D. dissertation, Columbia University, (1978), Published as NASA Tech. Memo. 78071

9. Cohen, R.S., Cong, H., Dame, T.M., Thaddeus, P., Ap. J. Lett. 230, 153 (1980)

10. Collin, R., Fundations for Microwave Engineering (McGraw-Hill, New York, 1972)

11. Cong, H.-I., Ph.D. dissertation, Columbia University, (1977)

12. Cong, H.-I., Kerr, A.R., and Mattauch, R.J., IEEE Trans. Microwave Theory and Tech. MTT-27, 245 (1979)

13. Dame, T.M., Ph.D. disertation, Columbia University, (1983), Published as NASA Tech. Paper. 2288

14. Dolan, G.J., Phillips, T.G., and Woody, D.P., Appl. Phys. Lett. 34, 347 (1979)

15. Dolan, G.J., Linke, R.A., Sollner, T.C.L.G., Woody, D.P., and Phillips, T.G., IEEE Tras. Microwave Theory Tech. MTT-29, 87 (1981)

16. Elmegreen, B.G., Lada, C.J., Ap. J. 214, 725 (1977)

17. Feldman, M.J., J. Appl. Phys. 53, 584 (1982)

18. Feldman, M.J., Pan, S.-K., Kerr, A.R., and Davidson, A., IEEE Tran. Magn. MAG-19, 494 (1983)

19. Feldman, M.J., Ruder, S., in Reviews of Infrared and Millimeter Waves, Volume 1, edited by Button, K.J., (Plenum, New York, 1983), pp. 47-75.

20. Giaever, I., Phys. Rev. Lett. 5, 147 (1960)

21. Giaever, I., Phys. Rev. Lett. 5, 464 (1960)

22. Harris, R.E., Phys. Rev. B 10, 84 (1974)

23. Held, D.N., Doctoral thesis, Columbia University, (1976). Published as NASA Goddard Space Flight Center Report No. X-130-77-6.

24. Held, D.N., and Kerr, A.R., IEEE Trans. Microwave Theory Tech. MTT-26, 49 (1978)

25. Held, D.N., and Kerr, A.R., IEEE Trans. Microwave Theory Tech. MTT-26, 55 (1978)

26. Huang, Y.-L., Ph.D. dissertation in preparation, Columbia University

27. Huang, Y.-L., Dame, T.M., Pan, S.-K., and Thaddeus, P., to appear in Bulletin of the A.A.S. Proceedings of the 164th Meeting (Baltimore, MD., June 11-13, 1984)

28. IBM J. Res. Develop. 24, 105-264 (1980)

29. Josephson, B.D., Phys. Lett. 1, 251 (1962)

30. Kautz, R.L., Journal of Research of the National Bureau of Standards. 84, 247 (1979)

31. Kelly, A.J., IEEE Trans. Microwave Theory Tech. MTT-25, 867 (1977)

32. Kerr, A.R., IEEE Trans. Microwave Theory Tech. MTT-27, 135 (1979)

33. Kerr, A.R., Pan, S.-K., Feldman, M.J., and Davidson, A., Physica. 108B, 1369 (1981)

34. Kerr, A.R., "Trans2: A basic-language program for analysis of passive lumped and distributed circuits on an Apple-II computer," NASA/GISS Internal Report, July, 1982

35. Lebrun, F., et al. Ap. J. 274, 231 (1983)

36. Leisawitz, D., Ph.D. dissertation in preparation, University of Texas of Austin

37. Magerlein, J.H., IEEE Trans. Magn. MAG-17, 286 (1981)

38. Matick, R.E., Transmission Lines for Digital and Communication Networks (McGraw-Hill, New York, 1969)

39. Mauzy, B., NRAO Electronics Division Internal Report, No. 146 (1974)

40. Olsson, L., Rudner, S., Kollberg, E., and Lindstrom, C.O., in "Proceedings of the 12th European Microwave Conference," (Microwave Exhibitions and Publishers, Kent) 270 (1982)

41. Olsson, L., Rudner, S., Kollberg, E., and Lindstrom, C.O., Int. J. Infrared and Millimeter Waves. 4, 847 (1983)

42. Palmer, E.S., "A frequency-agile phase lock system for stabilizing millimeter wave klystrons," NASA/GISS Internal Report, May 1982

43. Pan, S.-K., Feldman, M.J., Kerr, A.R., and Timbie, P., Appl. Phys. Lett. 43, 786 (1983)

44. Pan, S.-K., Feldman, M.J., Kerr, A.R., Palmer, E.S., Grange, J.A., and Timbie, P., in "Digest of the Eighth International Conference on Infrared and Millimeter Waves," (IEEE cat. No. 83CH1917-4), edited by Temkin, R.J., (IEEE, New York, 1983), P.M6.2

45. Phillips, T.G., Jefferts, K.B., Rev. Sci. Instrum. 44, 1009 (1973)

46. Phillips, T.G., and Woody, D.P., Ann. Rev. Astron. Astrophys. 20, 285 (1982)

47. Predmore, C.R., Raisanen, A.V., Erickson, N.R., Goldsmith, P.F., and Marero, J.L.R., IEEE Trans.

Microwave Theory Tech. MTT-32, 498 (1984)

48. Reifenstein III, E.C., Wilson, T.L., Burke, B.F., Mezger, P.G., and Altenhoff, W.J., Astron. & Astrophys. 4, 357 (1970)

49. Richards, P.L., Shen, T.-M., Harris, R.E., and Lloyd, F.L., Appl. Phys. Lett. 34, 345 (1979)

50. Rogovin, D., and Scalapino, D.J., Ann. Phys. 86, 1 (1974)

51. Rudner, S., and Claeson, T., Appl. Phys. Lett. 34, 711 (1979)

52. Rudner, S., Feldman, M.J., Kollberg, E., and Claeson, T., IEEE Trans. Magn. MAG-17, 690 (1981)

53. Rudner, S., Feldman, M.J., Kollberg, E., and Claeson, T., J. Appl. Phys. 52, 6366 (1981)

54. Saleh, A.A.M., Theory of Resistive Mixers (MIT Press, Cambridge, 1971)

55. Schneider, M.V., Bell Syst. Tech. J. 48, 1421 (1969)

56. Schneider, M.V., Chapter 4 of Infrared and Millimeter Waves, Vol. 6, edited by Button, K.J., (Academic Press, New York, 1982)

57. Shen, T.-M., IEEE J. Quantum Electron. QE-17, 1151 (1981)

58. Siegel, P.H., Ph.D. dissertation, Columbia University, (1983), Published as NASA Tech. Paper. 2287.

59. Siegel, P.H., Peterson, D.W., and Kerr, A.R., IEEE

Trans. Microwave Theory and Tech. MTT-31, 473 (1983)

60. Silver, A.H., Pedersen, R.J., McColl, M., Dickman, R.L., and Wilson, W.J., IEEE Trans. Magn. MAG-17, 698 (1981)

61. Smith, A.D., McGrath, W.R., Richards, P.L., van Kempen, H., Prober, D.E., and Santhanam, P., Physica. 108B, 1367 (1981)

62. Smith, A.D., and Richards, P.L., J. Appl. Phys. 53, 3806 (1982)

63. Sollner, T.C.L.G., Physica 108B, 1365 (1981)

64. Stark, A.A., Proceedings of National Radio Science Meeting (Boulder, Colorado, January 5-7, 1983)

65. Sutton, E.C., IEEE Tran. Microwave Theory Tech. MTT-31, 589 (1983)

66. Taur, Y., and Kerr, A.R., Appl. Phys. Lett. 32, 775 (1978)

67. Taur, Y., IEEE Tran. Electron Devices. ED-27, 1921 (1980)

68. Thaddeus, P., Phil. Trans. R. Soc. Lond. A 303, 469 (1981)

69. Tiuri, M.E., in Radio Astronomy, Chapter 7, by Kraus, J.D., (McGraw-Hill, New York, 1966)

70. Torrey, H.C., and Whitmer, C.A., Crystal Rectifiers MIT. Radiation Lab. Series. Vol. 15. (McGraw-Hill, New York, 1948)

71. Tucker, J.R., and Millea, M.F., Appl. Phys. Lett.

33, 611 (1978)

72. Tucker, J.R., and Millea, M.F., IEEE Trans. Magn. MAG-15, 288 (1979)

73. Tucker, J.R., IEEE J. Quantum Electron. QE-15, 1234 (1979)

74. Tucker, J.R., Appl. Phys. Lett. 36, 477 (1980)

75. Tucker, J.R., in Reviews of Infrared and Millimeter Waves, Volume 1, edited by Button, K.J., (Plenum, New York, 1983), pp. 1-46.

76. Tucker, J.R., and Feldman, M.J., "Quantum detection at millimeter wavelengths," to be published in Reviews of Modern Physics

77. Uhlir, A.Jr., Bell Syst. Tech. J. 37, 951 (1958)

78. Weinreb, S., and Kerr, A.R., IEEE J. Solid-State Circuits. SC-8, 58 (1973)

79. Weinreb, S., Fenstermacher, D.L., and Harris, R.W., IEEE Trans. Microwave Theory Tech. MTT-30, 849 (1982)

80. Werthamer, N.R., Phys. Rev. 147, 255 (1966)

81. Yariv, A., Quantum Electronics, Second Edition, (John Wiley & Sons, Inc., New York, 1975)

82. Zappe, H.H., and Landman, B.S., J. Appl. Phys. 49, 4149 (1978)

83. Zuckerman, B., Ann. Rev. Astron. Astrophys. 18, 263 (1980)

BIBLIOGRAPHIC DATA SHEET

1. Report No. NASA TM-87792	2. Government Accession No.	3. Recipient's Catalog No.
4. Title and Subtitle A Superconducting Tunnel Junction Receiver for Millimeter-Wave Astronomy		5. Report Date July 1986 6. Performing Organization Code 612
7. Author(s) Shing-Kuo Pan and Anthony R. Kerr		8. Performing Organization Report No.
9. Performing Organization Name and Address NASA/Goddard Institute for Space Studies New York, New York 10025		10. Work Unit No. 11. Contract or Grant No.
12. Sponsoring Agency Name and Address National Aeronautics and Space Administration Washington, DC 20546		13. Type of Report and Period Covered Technical Memorandum 14. Sponsoring Agency Code

15. Supplementary Notes

Shing-Kuo Pan: NASA Goddard Institute for Space Studies, New York, New York and Columbia University, New York, New York.
Anthony R. Kerr: NASA Goddard Institute for Space Studies, New York, New York.

16. Abstract

This report describes the development and construction of an ultra-low noise heterodyne receiver for millimeter-wave astronomy, and its use for 115.3 GHz CO line observations. The receiver uses a Superconductor-Insulator-Superconductor (SIS) quasi-particle tunnel junction mixer to convert the millimeter wavelength signal to a microwave intermediate frequency.

The first part of the report describes experiments aimed at quantitative verification of J. R. Tucker's quantum mixer theory, to see whether it could be used as the basis for the design of a practical receiver. The experimental results were in excellent agreement with the theory, assuming the three-frequency approximation. Infinite available gain and negative output resistance were observed for the first time, non-classical effects which are not seen in conventional diode mixers.

Using Tucker's theory, an SIS receiver was then designed and constructed. At 115 GHz, the single sideband receiver noise temperature is 83K, the lowest ever reported in this frequency range.

Finally, a CO survey toward Cygnus-X region, using this SIS receiver on the Columbia-GISS 4-ft. telescope, is described.

17. Key Words (Selected by Author(s)) Superconductivity Superconductor-Insulator-Superconductor Quasi-Particle Tunnel Junction Mixer Millimeter Wave	18. Distribution Statement Unclassified - Unlimited Subject Category 76

19. Security Classif. (of this report)	20. Security Classif. (of this page)	21. No. of Pages	22. Price*
Unclassified	Unclassified	244	A11

*For sale by the National Technical Information Service, Springfield, Virginia 22161

NASA-Langley, 1986

End of Document